

# **ANALYSIS OF ELECTRON ENERGY-LOSS SPECTRA AND IMAGES**

Analyse van electronen energie-verlies  
spectra en beelden

## **Proefschrift**

ter verkrijging van de graad van doctor  
aan de Erasmus Universiteit Rotterdam  
op gezag van de Rector Magnificus  
Prof. Dr. C.J. Rijnvos

en volgens het besluit van het College van Decanen.

De openbare verdediging zal plaatsvinden op  
Woensdag 30 juni 1993 om 11.45 uur

door

**Cornelia Wilhelmina Johanna Sorber**  
geboren te Dordrecht

---

Promotie-commissie

Promotor: Prof. Dr. J.F. Jongkind

Co-promotor: Dr. W.C. de Bruijn

Overige leden: Prof. Dr. E.S. Gelsema  
Prof. Dr. F.T. Bosman  
Prof. Dr. N. Bonnet

Dit proefschrift werd bewerkt binnen de vakgroep Pathologische Anatomie en de vakgroep Celbiologie van de Faculteit der Geneeskunde en Gezondheids-  
wetenschappen, Erasmus Universiteit Rotterdam.



Gedrukt door: Drukkerij Haveka B.V., Alblasterdam

---

*Always look on the bright side of life.*

**Monty Python's Life of Brian, 1979**

Voor mijn ouders,  
Oma,  
Wilma en Peter



<b>Chapter 1</b>	General introduction	1
<b>Chapter 2</b>	Materials and methods	17
<b>SPECTRAL ANALYSIS</b>		
<b>Chapter 3</b>	1. Optimization of the background-fit	27
<b>Chapter 4</b>	2. The application of Bio-standards	49
<b>IMAGE ANALYSIS</b>		
<b>Chapter 5</b>	1. Morphometrical analysis with electron spectroscopic imaging of non-element related images	67
<b>Chapter 6</b>	2. Morphometrical- and qualitative analysis of electron energy-loss images	87
<b>Chapter 7</b>	3. Concentration measurements in electron energy-loss images	101
<b>Chapter 8</b>	4. The use of multivariate statistical analysis for the analysis of electron energy-loss images	117
<b>Chapter 9</b>	General discussion	139
	List of abbreviations	145
	References	149
	List of publications	161
	Summary / Samenvatting	165
	Acknowledgements	169
	Curriculum vitae	170



---

# CHAPTER 1

## GENERAL INTRODUCTION

## CHAPTER 1

### GENERAL INTRODUCTION

#### INTRODUCTION

Analytical techniques are widely used to detect the presence of chemical elements in biological and biomedical tissue. At a cellular level, this information can also provide an impression of the state of functioning of a cell.

Electron microscopy is one of the analytical techniques that can be used for the analysis of biological specimens at an ultrastructural level. Two types of data can be acquired: morphological and chemical data. Recent developments in instrumentation allow a combination of -in situ- high resolution morphometrical analysis with chemical elemental analysis [Egerton (1986)].

Among the electron microscopical techniques that allow to combine morphometrical and chemical analyses is electron energy-loss spectroscopy (EELS). With this kind of analysis the chemical data are acquired either as a spectrum to be related to the analyzed area in the image or as a chemical elemental distribution image to be related to the morphological information.

In electron microscopical analysis of cellular material, the following issues need to be addressed:

- 1. Identification of the chemical element(s), which may be characteristic for the cellular material.
- 2. Localization of the chemical element(s) in the specimen. The localization may be confined to certain cell-organelles.
- 3. Quantification of the concentration of the chemical element(s) in the biological material.

Positive identification may fail for the following reasons:

- 1. The element is present in the living cell but was lost as a consequence of the treatment of the specimen.
- 2. The instrumental technique used may not be adequate for detection.

Amongst the many analytical techniques, which are in principle available, only a few include a combination of a sensitive -in situ- analysis of chemical elements

with the high spatial resolution as present in electron microscopy. EELS analysis can be used for both identification and quantification of chemical elements in the biological items of interest, at high spatial resolution.

In practice, quantitative EELS information may be obtained in two ways:

- (a) *Quantitative Spectral Analysis (QSA)*; In this type of analysis, an electron energy-loss (EEL) spectrum of the analyzed area of the specimen is recorded and the ionization events are detected as edges which are related to the different elements. Subsequently, the edges are extracted and used for further element quantification, in relation to the total mass of the analyzed area.
- (b) *Quantitative Image Analysis (QIA)*; For this type of analysis, several electron spectroscopic images (ESI) are recorded around one specific ionization edge. As with QSA, but now pixel-wise, the ionization event is extracted and allows 2-dimensional spatial element-distribution images to be acquired. The extraction procedures used for this analysis are similar to those used with QSA, being applied on each sequence of corresponding pixels in the images. This type of analysis offers an additional possibility of morphometry. Images which contain only the element under investigation are related to total mass images to acquire element concentration-distribution images. When more elements are present these element-distribution images can be combined to show their correlation with each other.

These two techniques will be discussed in more detail in paragraphs 1.3 and 1-4.

Numerous examples can be found in which the analysis of a specific chemical element plays an important role in the investigation of a disease or in the metabolism of a cell:

- 1. Localization and identification of calcium [Arsenault & Ottensmeyer (1983); Körtje *et al.* (1990a, 1990b); Probst (1986)].
- 2. Localization of conglomerations of iron in hepatic lysosomes of patients with idiopathic haemosiderosis [Cleton *et al.* (1986, 1989), Ringeling *et al.* (1989, 1990)].
- 3. Storage of metabolites in cells from patients with certain lysosomal or cytoplasmic enzyme-deficiencies can occur because such metabolites fail in further degradation. The nature of such material, sometimes disclosed by a chemical element, which can accumulate in certain celltypes or organelles, can give information about the kind of enzyme-deficiency.
- 4. Also the activity of enzymes can be determined by the precipitation of their

## Chapter 1

reaction-products (e.g. phosphate by cerium (capture ion) in the case of acid phosphatase, and sulphate by barium in the case of the enzyme aryl-sulphatase) [Van Dort *et al.* (1989), Sorber *et al.* (1990b)].

- 5. Intracellular NaK-determination for the diagnosis of cystic fibrosis [Roomans *et al.* (1980)].

The application of -in situ- EELS analysis will be used to show the validity of this analytical method. In the next paragraphs the analytical potentials of energy filtering transmission electron microscopy (EFTEM) will be shown.

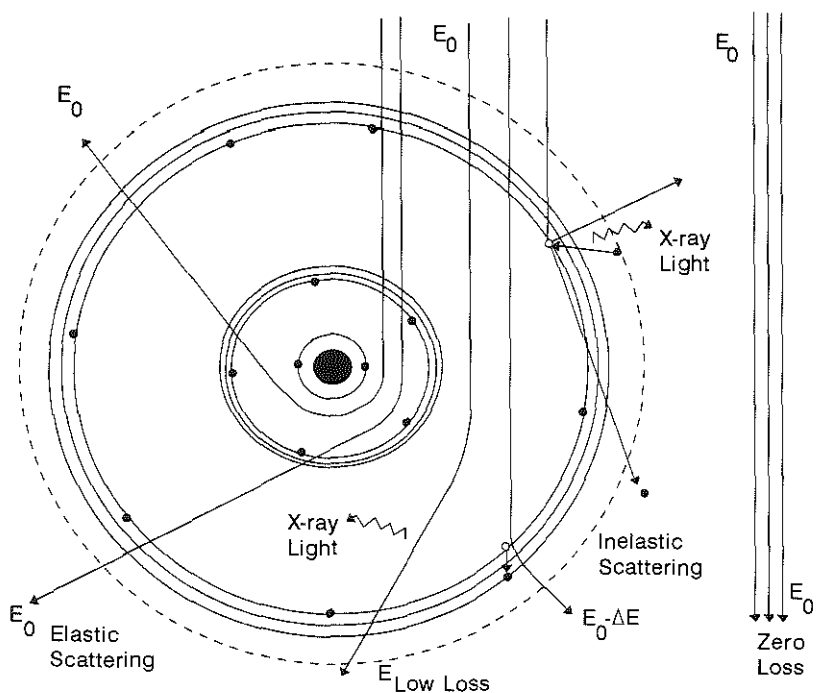


**Figure 1.1.** Schematic view of the possible interactions of the incident electrons with an atom of the specimen. A large part of the incident electrons escapes from any reaction at all (*zero-loss electrons*). Those which have reacted with the atomic nucleus undergo virtually no loss of energy and are deflected over large angles (*elastically scattered electrons*). Incident electrons which have reacted with shell-electrons of the atom, are subject to an energy-loss ( $\Delta E$ ) and are scattered over small angles (*inelastically scattered electrons*) while the shell-electrons are excited. Inelastically scattered electrons are used for EELS-analysis.

**ENERGY FILTERING TRANSMISSION ELECTRON MICROSCOPY***Interactions in the electron microscope*

In the electron microscope, fast-moving gun-derived electrons with energy  $E_0$  may interact, in a variety of ways, with the atoms of the (biological) material because of electrostatic (Coulomb) forces. A large proportion of the electrons ( $\pm 90\%$ , depending on the thickness of the section), escapes from any interaction and are registered beyond the specimen as zero-loss electrons. However, a small part of the beam-electrons are scattered as a result of the interactions with the atoms of the specimen (Fig. 1.1).

The elastically scattered electrons, which have interacted with the atomic nucleus, undergo virtually no loss of energy and can be deflected in a large angle. The elastically scattered electrons that are not filtered out by a diaphragm can be found in the zero-loss peak of the EEL-spectrum.

The inelastically scattered electrons, which have interfered with the shell electrons of the atoms in the specimen, are subject to an energy-loss ( $\Delta E$ ) and are deflected over a small angle, while the shell electrons are excited (the atom is ionized). Populations of such electrons are registered beyond the specimen as element specific energy-loss electrons.

*Inelastic scattering*

The inner-shell electrons can only be excited if they absorb an amount of energy greater than their original binding energy. Because the total energy is conserved at each collision, the fast beam-electrons lose an equal amount of energy.

The outer-shell electrons can also undergo single-electron excitation. The energy needed for this transition generally is only 5-50 eV. Particularly in organic compounds not all of the valence electrons return to their original state. The permanent disruption of chemical bonds is described as radiation (ionization) damage.

In addition to the outer-shell single-electron mode of excitation, inelastic scattering may involve electrons of many atoms of the solid. This collective effect is known as a plasma resonance (an oscillation of the valence-electron density). According to quantum theory, the excitation can also be described in terms of the creation of a pseudo particle, the plasmon [Egerton (1986)].

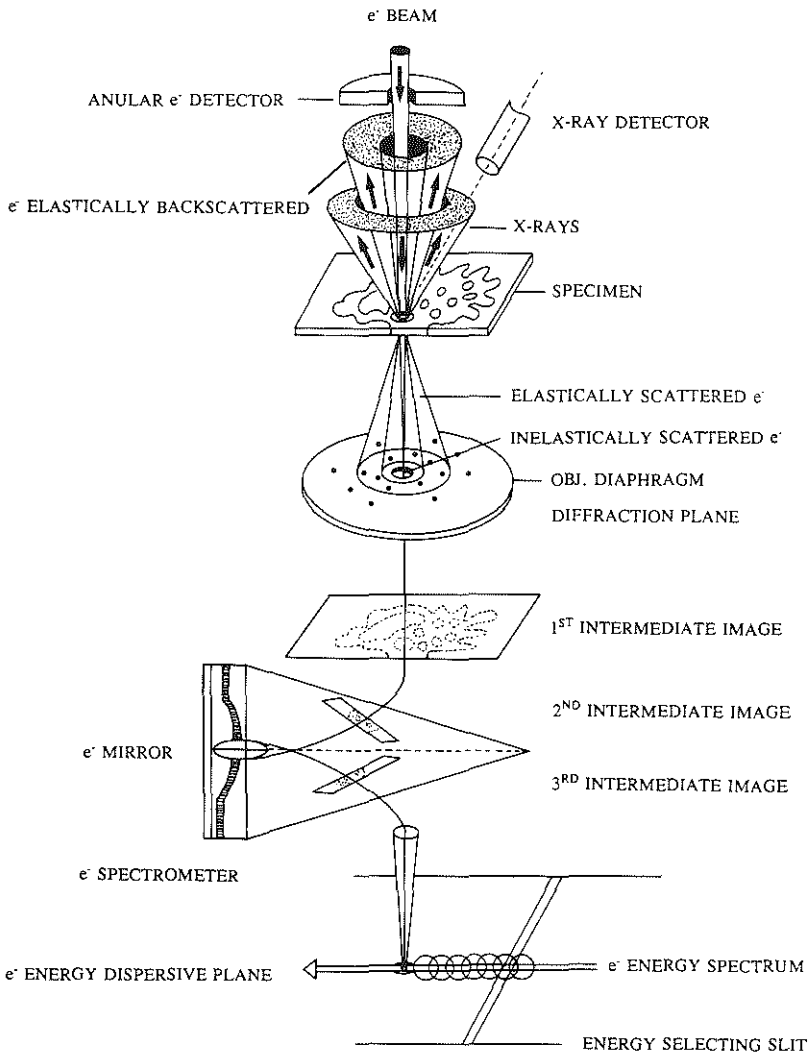


**Figure 1.2,** In this cross-section of a hypothetical microscope, EELS and EPMA are combined. Above the centrally placed specimen the incident electrons produce back-scattered electrons which can be used for image formation and X-rays for elemental analysis. In the area below the specimen the inelastically scattered electrons that have passed through the (objective) diaphragm are guided through the electron spectrometer to the energy-dispersive plane, where the total energy-loss spectrum is. An energy-selecting slit allows element specific-parts of the energy-loss spectrum to pass for spectrum or image recording.

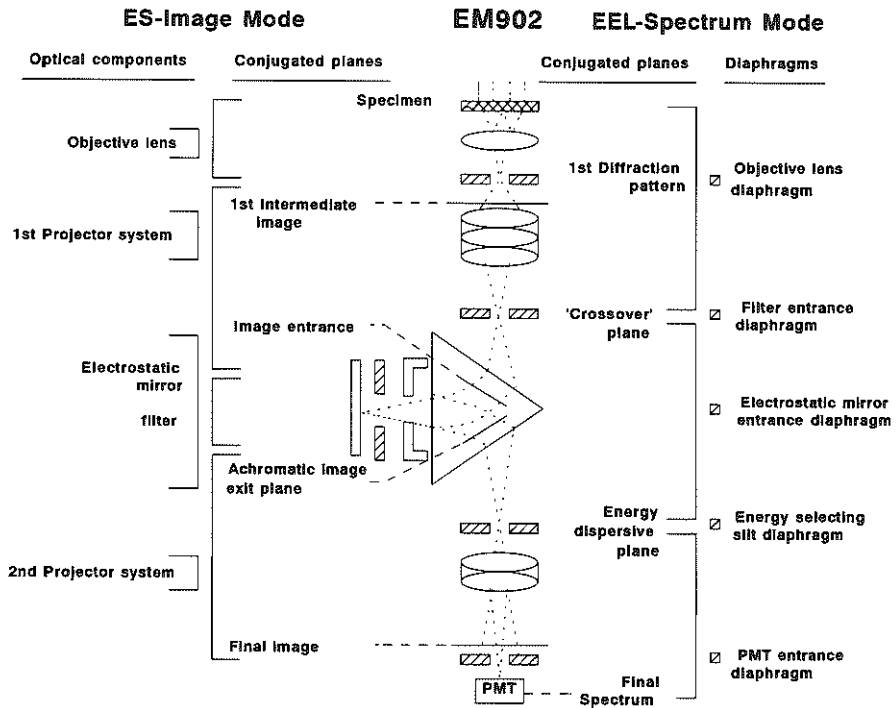


**Figure 1.3,** Cross-section of the Zeiss EM902 column, showing the various optical components, diaphragms and conjugated planes for spectra and images.

The return of the shell-electron from its excited state causes its excess energy to be emitted in the form of specific element-related X-rays or as kinetic energy of another atomic electron (Auger emission). The amount of X-rays of a specific energy or Auger-electrons can be used for qualitative and quantitative chemical analyses of the irradiated material (electron-probe microanalysis (EPMA) or Auger spectroscopy) (Fig. 1.2).

An alternative way of evaluation of the irradiated material, is electron energy-loss spectroscopy, which examines the element-specific amount of energy-loss. The inelastically scattered electrons, which have lost element-specific energy, bear the information about the spatial chemical composition of the irradiated specimen.

### *Recording of the energy-loss*

In a conventional transmission electron microscope (CTEM) the beam of electrons is directed into a high-resolution electron spectrometer which separates the electrons according to their kinetic energy and produces an electron energy-loss

## Chapter 1

---

spectrum showing the scattered intensity as a function of the decrease in kinetic energy of the fast electrons, in electron volts (eV).

There are various techniques for the differentiation of electrons according to their energy-losses by using internal magnetic fields in a spectrometer inside the microscope column such as the electron-magnetic prism/mirror/prism combination in the projector lens system of a transmission electron microscope which is present in the Zeiss EM902 (Fig. 1.3) [Castaing and Henry (1962), Henkelman and Ottensmeyer (1974), Castaing (1975), Egerton *et al.* (1975), Andrew *et al.* (1978), Egle *et al.* (1984)] or the omega-filter, which is well-suited for use with a high-voltage CTEM [Rose and Plies (1974), Krahl *et al.* (1978), Zanchi *et al.* (1975, 1977, 1978, 1982), Pejas and Rose (1978)].

Outside the microscope column one can use a sector magnet or a Wien-filter, which employs both magnetic and electrostatic fields.

In this thesis an electron-magnetic prism/mirror/prism instrument is used in which the electrons are first deflected in the magnetic field of the prism, then reflected by the electrostatic field of the mirror and again deflected in the magnetic prism. As the deflection of the electrons in a magnetic field is proportional to the square root of their energy, the spectrometer disperses the electrons in the energy dispersive plane according to their energy ( $E_0$ ,  $E_0 - \Delta E_i$ ).

The Zeiss EM902, which was used during this study, contains an imaging electron-energy spectrometer, which allows high resolution imaging with energy selected (mono-energetic=mono-chromatic) electrons. This technique is called "Electron Spectroscopic Imaging (ESI)" with which a spatial resolution of less than 0.5 nm can be achieved.

This energy selection is performed by the introduction of a slit in the energy-dispersive plane which is conjugate with the backfocal plane of the objective lens.

When there is no slit in the energy-dispersive plane of the spectrometer, both the unscattered-, the low-angle elastically scattered- and the inelastically scattered electrons are imaged in the final image plane (**global imaging** (Fig. 1.4a)). The information content of these images in this case is comparable with that of a conventional transmission electron microscope. As these electrons have varying energies ( $E_0$ ,  $E_0 - \Delta E_i$ ) and hence varying wavelengths, they are focused in the EM in different sites and impair the image quality. When a slit/diaphragm is introduced into the energy-dispersive plane, it can be positioned in such a way that the inelastically scattered electrons are stopped by the slit and only the unscattered electrons reach the final image plane. With biological sections this results in image-

contrast enhancement (**Zero-loss imaging**, Fig. 1.4b).

Biological materials and most embedding materials consist chiefly of light elements which do not scatter electrons elastically very effectively. As a result the contrast of biological specimens in conventional brightfield imaging is very low. Only by staining with heavy metals, a stronger elastical scattering can be achieved which enhances the cell structures with which the stain-molecules have reacted. Heavy metal staining, however, tends to produce small clusters of metal. Consequently, the resolution is impaired and is generally limited to about 2 nm.

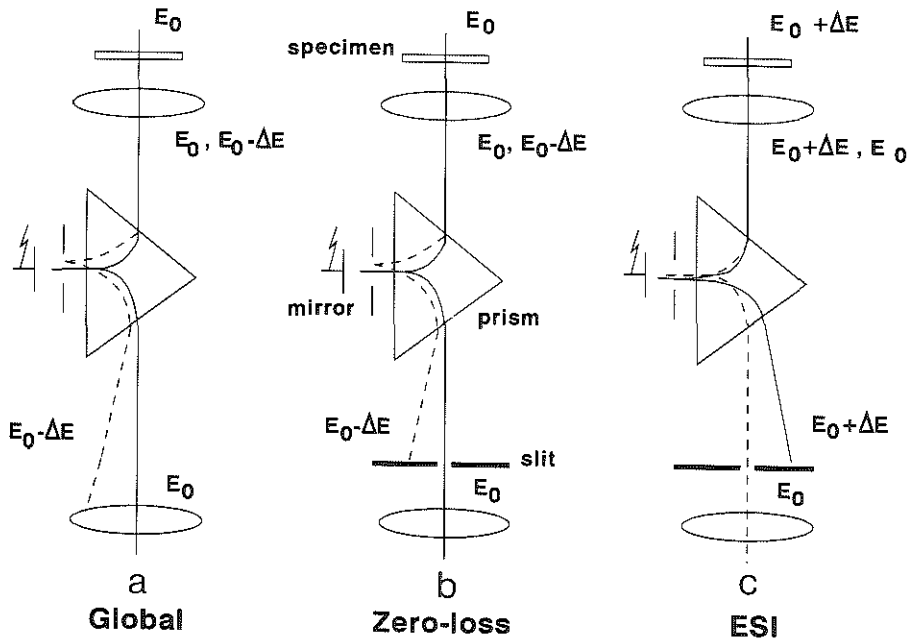


**Figure 1.4,** Three imaging modes in the electron microscope: (a) Global imaging in which all electrons take part; (b) Zero-loss imaging in which only zero-loss electrons are used by positioning a slit in the energy-dispersive plane to filter out all other electrons; (c) Electron spectroscopic imaging (ESI) in which only inelastically scattered electrons, which have lost a small amount of energy, are used by increasing the energy of the incident beam with exactly this energy-loss.

With ESI-imaging, heavy metal staining can be omitted. In that case the energy of the incident beam is increased with a specific energy  $\Delta E$ , which causes the electrons which have undergone inelastic scattering with that specific energy-loss to be projected on the optical axis and on the detector, resulting in high-contrast images (**ESI imaging**, Fig. 1.4c). In that case the initial energy of the beam is increased with the energy of interest, so that only the electrons which have lost that specific energy will be visible on the screen.

In addition to energy-selected imaging, the energy content of the slitdiaphragm can be converted to an energy spectrum by projecting the electrons on a photomultiplier. By continuously changing the energy of the incident beam, a spectrum of the irradiated area in the specimen is recorded, in which the number of electrons is registered against the energy-loss (Fig. 1.5). As an alternative, the spectrum can be projected into the tv-camera and recorded as an image, thus obtaining a parallel recorded spectrum.

### *The electron energy-loss spectrum*

Around 0 eV, a high intensity peak is visible of the electrons that do not interact with the specimen and of the low-angle elastically scattered electrons. This peak is called the **zero-loss peak** (see Fig. 1.5).

From about 5-50 eV plasmon peaks can be visible. In this **low-loss region** electrons have interacted with atomic electrons of the outer-shells. The energy-levels of these outer-shell or valence electrons are not clearly defined. Several energy-loss mechanisms can be distinguished [Van Puymbroeck J. (1992), Newburry (1986), Goodhew and Humphreys (1988), Loretto (1984)]: volume plasmons, single-electron excitation, excitons, radiation losses, surface plasmons.

At higher energy-losses (in the **high-loss region**), features, which represent inner-shell excitations, appear at element-specific energy-losses on a continuously decreasing slope of aspecific energy-losses. They take the form of edges rather than peaks, the inner-shell intensity rising rapidly and then falling more slowly with increasing energy-loss. The sharp rise occurs at the ionization threshold, which is approximately the binding energy of the corresponding atomic shell. When viewed in greater detail, both the plasmon peaks and the ionization edges possess a fine structure (white lines) which reflects the crystallographic or energy-band structure of the specimen.

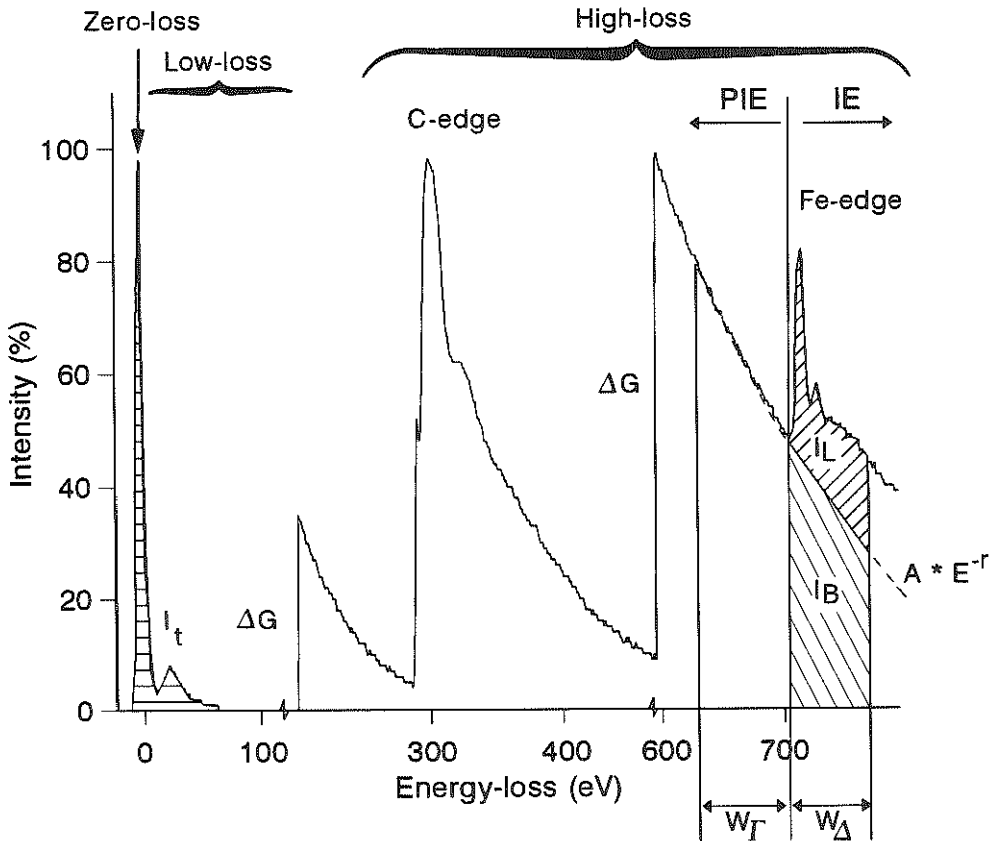


**Figure 1.5,** Example of a partially interrupted EEL-spectrum of a siderosome containing iron. A zero-loss peak and two edges (carbon (C) and iron (Fe)) are observed. The continuum under the Fe-edge is extrapolated according to a power-law model. PIE is the pre-ionization edge region, IE is the ionization-edge region.  $\Gamma$  is the part of the PIE used for the continuum estimation.  $\Delta$  is the part of the IE used for quantification of the element.  $\Delta G$  is an optional gain in the intensity of the signal.  $W$  is the width of a region.  $I_L$  is the integrated element-related signal.  $I_B$  is the integrated extrapolated continuum signal.  $I_t$  is the integrated total signal.

The tails of the ionization edges form a second continuous slope on top of the first one. To separate the edges from the preceding continuous slope, a mathematical procedure must be performed. Since in different parts of the spectrum, different edges may influence the continuous decreasing slope, this mathematical equation is not the same for the whole spectrum, which makes it necessary to calculate this equation for each part of the spectrum separately.

When an energy-loss spectrum is recorded from a sufficiently thin region of the specimen, each spectral feature corresponds to a different single excitation process. In thicker samples, there is a reasonable probability that a transmitted electron will be inelastically scattered more than once, giving a total energy-loss which is the sum of the individual energy-losses. In the case of plasmon scattering, the result is a series of peaks at multiples of the plasmon energy. The multiple scattering peaks have appreciable intensity if the specimen thickness approaches or exceeds the mean free path, which is the average distance between scattering events.

Inner-shell scattering occurs at comparatively low probability and therefore has a mean free path which is long compared to the section thickness. In ultrathin sectioned tissues the probability that a fast moving electron produces more than one inner-shell excitation is therefore considered to be negligible. However, an electron which has undergone inner-shell scattering may (with fair probability) also cause outer-shell excitation. This "mixed" inelastic scattering again involves an energy-loss which is the sum of the two separate energy-losses and results in a broad peak above the ionization threshold, displaced from the threshold by approximately the plasmon-peak energy ( $\pm 30$  eV). In Fig. 1.5 such a plasmon peak can be seen beyond the carbon-edge (C).

## ANALYSIS OF THE ELECTRON ENERGY-LOSS SPECTRUM

### *Separation of the background*

Historically, quantitative spectral EELS-analysis has predominantly concentrated on the curve-fitting procedures of the continuum in the pre-ionization-edge (PIE) region to acquire, after extrapolation beyond the ionization edge (IE), the core-loss ( $I_K$ ,  $I_L$ , etc) and background ( $I_B$ ) integrals as defined by Egerton [Egerton (1986)] (Fig. 1.5). K, L, M are the shells of the atom-electrons that are excited.  $\Gamma$  is the part of the PIE-region used for continuum estimation,  $\Delta$  is the part of the IE-region used for quantification of the edge.

In EEL-spectra, the background is assumed to follow an inverse power law:

$$I(E) = A * E^{-r} \quad (1.1)$$

where  $I(E)$  is the intensity at energy-loss  $E$ , and  $A$  and  $r$  are constants. Several background-fitting methods have been proposed:

1. Egerton's two-area method;
2. Bevington's Steepest Descent method;
3. Log-log transformation;
4. Simplex-optimization, which is a computational strategy to efficiently locate the optimum of a function of multiple parameters.

The four methods mentioned above will be discussed in chapter 3.

Critical examination of these methods will show which methods are best suitable for the analysis of EEL-spectra.

### Concentration measurements

A relative elemental concentration ( $R_x^*$ ) can be acquired by relating the spectral net-intensity signal  $I_{K,L,M,etc}$  to the total number of transmitted electrons  $I_t$ . Usually it suffices to take for  $I_t$  the integrated intensity in the zero-loss plus low-loss region of the spectrum (0-100 eV). This region contains about 99% of all transmitted electrons, as given by Egerton (1986):

$$R_x^* = \frac{I_{K,L,M,etc}(\beta, \Delta)}{I_t(\beta, \Delta) \cdot \sigma(\beta, \Delta)} \quad (1.2)$$

where  $K,L,M$  is the shell of the atom-electron which was excited by the beam-electron,  $\sigma$  is the partial ionization cross section, which is the probability that an incident electron causes edge-phenomena,  $\beta$  is the aperture in the objective lens back-focal plane and  $\Delta$  denotes the region of the spectrum used for quantification.

An alternative formulation of eq. 1.2 may be used in which  $I_B$  is the background integral, assuming that the background is the same for all items of interest in one section:

$$R_x = \frac{I_{K,L,M,etc}(\beta, \Delta)}{I_{K,L,M,etc}(\beta, \Delta) + I_B(\beta, \Delta)} \quad (1.3)$$

hereby avoiding the acquisition in the zero-loss + low-loss region which causes various instrumental problems.

### *Specimen thickness*

In quantitative analysis, many parameters, reflecting instrument-settings and/or properties of analytical procedures may influence the results obtained, such as the size of the hole in the objective lens diaphragm ( $\beta$ ), the number of integrations for image-acquisitions and the width of the  $\Gamma$ - and  $\Delta$ -region (chapter 3).

An important factor is the thickness of the specimen. Increase of the section thickness ( $t$ ) increases the probability of an interaction with the specimen. As mentioned before, when the thickness exceeds the minimum free pathlength ( $\lambda_x$ ), the probability of more than one interaction per electron increases, which may lead to a false interpretation of the results. Therefore, especially for quantitative analyses, thickness measurements must be performed. The thickness ( $t$ ) of the specimen can be calculated according to Leapman *et al.* (1984a) and Malis *et al.* (1988):

$$t = \lambda_x(\beta, \Delta) \cdot \ln \left( \frac{I_t}{I_0} \right) \quad (1.4)$$

where  $\lambda_x$  is the total inelastic mean free path for the collection angle  $\beta$  and width of the integration region ( $\Delta$ ),  $I_0$  is the number of the electrons which have not lost energy (zero-loss) and  $I_t$  is the total number of electrons (chapter 3).

## ANALYSIS OF ELECTRON ENERGY-LOSS IMAGES

### *Separation of the background*

In imaging mode, several images are recorded around the ionization edge. Through each sequence of corresponding pixels in the images before the edge, as with spectra, a background-equation is fitted, which is extrapolated and used to separate the background from the edge-information in the post-edge image. This yields a net-intensity image containing only the chemical element of interest. Several background estimation methods will be examined (chapter 7):

1. PIE-method.
2. Linear fitting.
3. Logarithmic fitting.

The results will be compared with the results obtained from spectra.

In some cases, however, these methods cannot be used (e.g. when the background does not follow an inverse power law). Therefore multivariate statistical analysis

(MSA) is examined as an alternative method for EELS-analysis, since this method does not depend on parameters to fit a background but instead analyses the information in a set of images. This information can be divided in element related information (edge-information) and non-element related information such as thickness-fluctuations and noise (chapter 8).

### *Integration of chemical and morphometric image analysis*

For integrated chemical and morphometric image analysis, attention has to be paid to the morphometric determination of area or area-fractions in element-distribution images, to monitor volume-changes in the chemical elemental distributions in the objects of interest in patient material (chapter 5, 6).

To distinguish  $R_x$ -values acquired from spectra from those acquired from images, these values are marked by superscripts S and I, respectively:  $^S R_x$  or  $^I R_x$ .

## BIO-STANDARDS

The application of standards for the determination of unknown concentrations in cell organelles and tissue is a well known practice in X-ray microanalysis [Roomans & Shelburne (1980), De Bruijn (1981a-b), De Bruijn & Cleton-Soeteman (1985), De Bruijn & Van Miert (1988)]. Pure-element thin-film standards and standards made from polyvinyl pyrrolidone (PVP) films have been proposed for EELS analysis [Shuman & Somlyo (1987), Leapman & Ornberg (1988)]. The use of the Chelex<sup>100</sup>-type ion-exchange bead as a standard for EELS will be investigated in this thesis. Such standards will be termed 'Bio-standards'. To determine the usefulness of the Chelex<sup>100</sup>-beads as a Bio-standard, several sections will be measured with the quantitative spectral analysis module (QSA), as described in chapter 2, to obtain the interbead and intrabead variation in elemental concentration.

These Bio-standards were also used to test various instrumental conditions and the performance of a computational procedure and to obtain absolute element concentrations in tissue.

## Chapter 1

---

---

# CHAPTER 2

## MATERIALS AND METHODS

### CHAPTER 2

#### MATERIALS AND METHODS

##### SPECTRUM ACQUISITION

###### *The spectrum acquisition chain*

The instrument used for this investigation is a Zeiss EM902 transmission microscope with an integrated electron energy filter according to Castaing/Henry/Ottensmeyer. Several acquisition chains are connected to the EM902 transmission electron microscope (Zeiss, Oberkochen, FRG) as shown in Fig. 2.1.

The spectrum acquisition chain leads to an Olivetti M280 personal computer, which also controls the spectrum control unit, the stage control unit and the microscope control unit. This chain consists of the following essential components:

- 1. Photo Multiplier (PMT) (in Zeiss EM902),
- 2. Amplifier (1x, 10x, 100x) (Central Research Workshop, Erasmus University, Rotterdam),
- 3. Digitizer (PC ADDA-12 card, FPC-010, QP-computer),
- 4. IBM compatible personal computer (Olivetti M280).

The EEL-spectra serially acquired from the EM902 are electron intensity recordings of consecutive channels in the range of 0-2000 eV with minimum nominal step increments of 0.5 eV. The energy resolution depends on the magnification and the objective-lens diaphragm, and is limited to a minimum of 1 eV. The setting of the spectrometer is software-controlled by a Quantitative Spectrum Analysis module (QSA) on the personal computer. The electron intensity in an energy-loss channel is measured by the photo-multiplier (PMT). This analog signal can be further amplified (10x or 100x) by an additional amplifier depending on the part of the spectrum which is being recorded. The first part of the spectrum (0-200 eV) needs no amplification, while the middle part (200-400 eV) needs a 10x amplification and the last part (400-2000 eV) a 100x amplification. After this optional second amplification, the analog signal is digitized by the PC ADDA-12 card (12-bit deep).

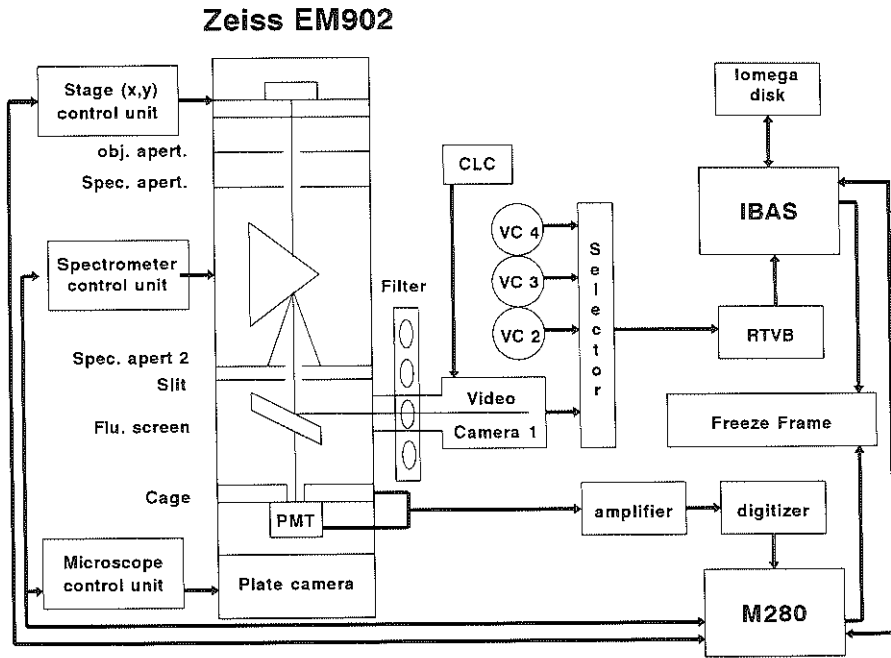


**Figure 2.1,** Schematic representation of the spectrum- and image-acquisition routes connecting the Zeiss EM902 to the Olivetti M280 computer, and to the IBAS 2000 image analyzer.

A pre-chosen energy band (e.g. 200 eV wide) is seemingly moved over the energy-selecting slit, actually by changing the high tension (e.g. from 80,750 to 80,950 eV) over a constant (but adjustable) time interval. Only elements present in the irradiated area with energy-losses within that band appear, generally with an intensity edge on a steadily decreasing continuum of inelastically scattered electrons

### *The quantitative spectral analysis module (QSA)*

This module is developed by the author. It is written in Turbo Pascal 4.0 and is organized as follows:

Before the actual spectrum acquisition takes place, the instrumental conditions are optimized with the use of an intensity calibration module by monitoring the signal from one channel of interest (channel with the highest intensity in the spectrum) on the screen while the microscope-settings are being changed.

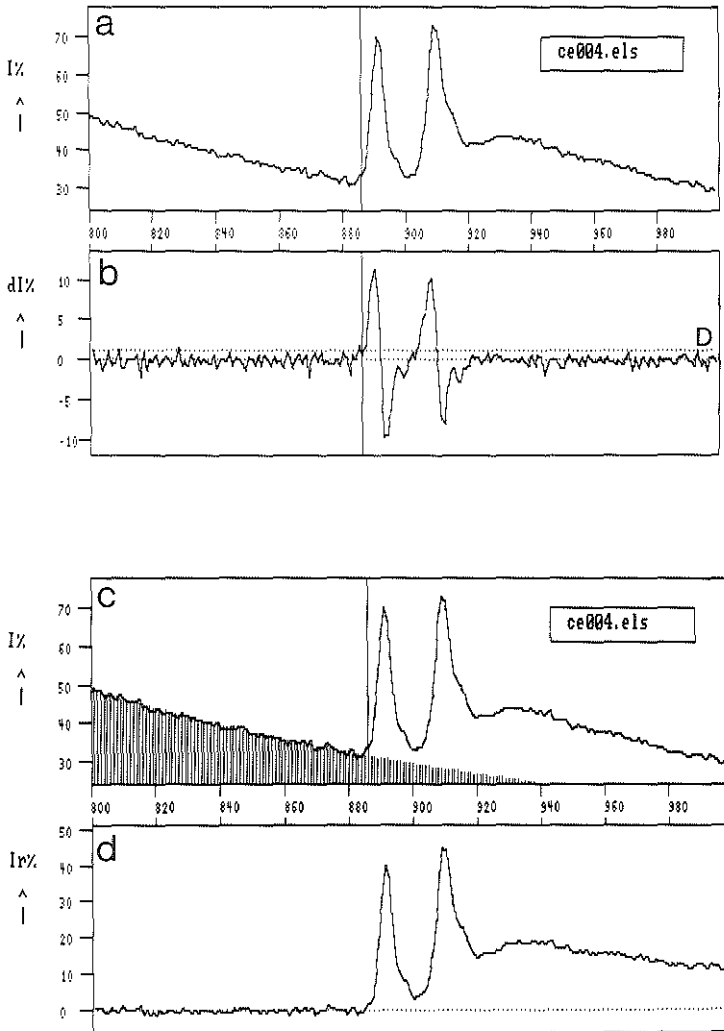


**Figure 2.2.** The four steps of spectrum processing by the QSA-program. (a) The recorded unprocessed Ce-standard spectrum. (b) The first derivative to find the ionization edge. The dotted line **D** represents the detection-limit for the edges, which is  $n \cdot \sigma$  ( $\sigma$  = standard deviation of baseline,  $n$  = a constant). (c) The fitted background indicated by the hatched area. (d) The result of the subtraction of the fitted background from the original spectrum.

The stage control unit is used to pre-select places of interest in the sections at a beam intensity which is kept as low as possible to reduce radiation damage. Their X-Y-coordinates are stored before spectral acquisition at all pre-selected places takes place in one run.

Spectrum recording is started after specifying in the main-QSA-menu the start and final eV-values and a set of parameters. While the spectrum data are recorded, the spectrum is on-line displayed on the screen. Each channel may be recorded several times to reduce noise. The mean value per channel is stored on disk. The EM902 information such as magnification, analyzed area, etc, is retrieved from the microscope control unit and is stored in front of the spectrum-data. The spectrum can then be evaluated immediately or off-line.

In Fig. 2.2, the processing of a Cerium-spectrum (Fig. 2.2a) is shown. The first derivative of the recorded spectrum (Fig. 2.2b) is used for the determination of the start of the ionization-edge. Next, the background-curve is fitted through a part of the PIE ( $\Gamma$ -range) and is extrapolated beyond the IE (Fig. 2.2c). The fitted curve is then subtracted from the original spectrum leading to the ratio-value  $R_C$  (Fig. 2.2d).

## IMAGE ACQUISITION

### *Image acquisition chain*

Analogue images are recorded on photographic emulsion (SO 163, Kodak, The Hague, NL) or are transferred to an image analyzer (IBAS 2000, Zeiss/Kontron, Oberkochen, FRG) by a TV camera for digitization and further analysis, processing or storage by normal routine (Zeiss/Kontron) software. To keep the camera-gain settings constant during acquisition of a series of images, a camera light controller (CLC) has been introduced in the image-pathway.

Unfortunately, the dynamic range of the TV-camera was not sufficient to allow the acquisition of both ESI- and zero-loss images with the same camera-settings, which is needed for  $R_C^*$ -measurements. Therefore, an optical filter was inserted in front of the camera which is used during the acquisition of the zero-loss image(s) with the same camera-settings as the ESI-images. The optical filter set, positioned in the C-mount that couples the TV-camera to the microscope column, consists of a light-tight flat box in which the round filters enclosed in a black carrier can be moved backwards and forwards. The filters are Kodak calibrated grey-value filters.

Three optical densities are at present available ( $D = 5, 4, 3$ ). The optical filter and camera light controller were used from chapter 7 onwards.

EM902-derived energy filtered transmission electron microscopy (EFTEM) allows the acquisition of various ESI images. The three most commonly used types of images used for ultrathin-sectioned material are:

- 1 global images (Fig. 1.4a), in which all electrons passing the objective aperture are used for image formation and no energy-selecting slit is installed in the energy dispersive plane in front of the second projector lens system.
- 2 Zero-loss filtered images (Fig. 1.4b), in which primary electrons passing the objective aperture are used and the inelastically and elastically scattered electrons are excluded from image formation by the introduction of the energy-selecting slit ( $\pm 20$  eV).
- 3 Electron spectroscopic images (Fig. 1.4c), which are formed by selecting energy-losses with an energy-selecting slit of  $\pm 20$  eV. For ultrathin sections ( $\pm 80$  nm),  $\Delta E = 250$  eV is usually chosen since aspecific energy-losses give a high contrast image. After the Carbon edge (284 eV) this information will be "drowned" in the relatively high carbon-information.

### *The quantitative image analysis module (QIA)*

To obtain images around the various ionization edges of the elements involved (Th, Fe, Ba, Ce, P, S), as a rule, 100 real-time TV-images are acquired, digitized (512 x 512 pixels), averaged and stored on disk (Fig. 2.3a).

To eliminate, for morphological purposes, an inhomogeneous image illumination, a 100 times integrated, out-of focus image of the EPON background is also acquired and subtracted from the original image. After this "shading correction", an eight bit deep grey-value frequency histogram of the image is obtained (Fig. 2.3b). The first derivative of this histogram is used to acquire crossovers between the Gaussian curves for image segmentation (Fig. 2.3c). Subsequently, guided by the results of this segmentation, a binary image of the items of interest, e.g. nucleus or cytoplasm, is obtained (Fig. 2.3d). When necessary, dilatation and/or erosion is used to complete image processing (e.g. to remove remnants of adjacent cells from an image or to convert chromatin area to nuclear area). To eliminate unwanted (noise) remnants in the picture, the IBAS function SCRAP is used.

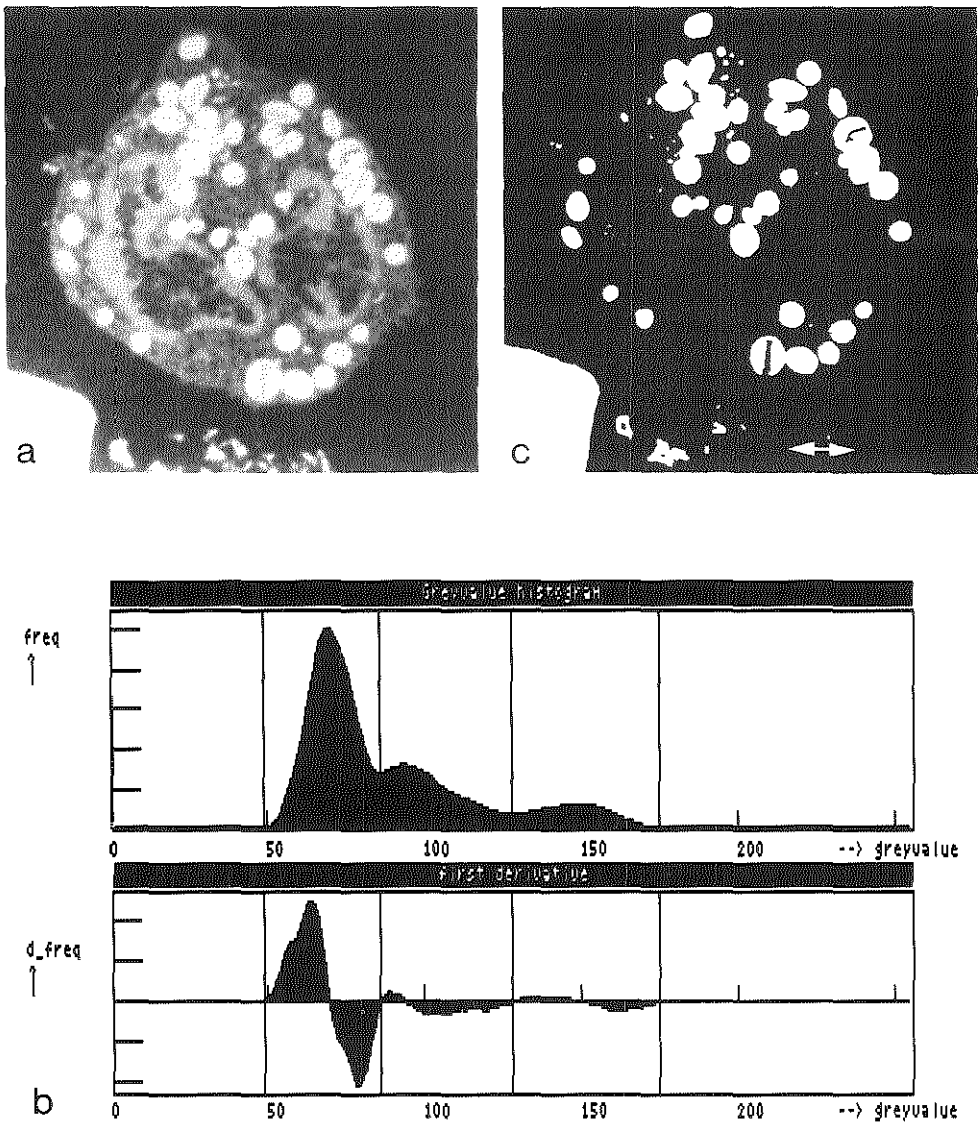


**Figure 2.3,** An example of image analysis as performed on a granulocyte: (a) Image to be segmented ( $\Delta E=250$  eV); (b) Grey-value frequency histogram; (c) First derivative; (d) Binary image of the population with grey-value  $\geq 125$ . The vertical lines in the histogram represent cross-overs between the different grey-value populations in the histogram.

## Chapter 2

---

Binary element-related images are given pseudo colours for better presentation or, for example to visually emphasize co-localization (chapter 5-6). Co-localization, defined by a simultaneous occurrence of pixels at the same place in two images, is established by superposition of an ESI and an element-distribution image, or alternatively, of two or more element-distribution images, by the Boolean operator OR and adapting the pseudo colours accordingly.

The resultant digital images are recorded from the IBAS-screen by a camera (FreezeFrame videorecorder, Polaroid) loaded with colour film (Ektachrome, Kodak).

By comparing the number of pixels inside the items of interest with the total number in a cell or frame, the relative area (in pixel %) may be obtained. Images of a grating replica, acquired under the same conditions, are used to convert relative to real areas or real lengths. Because the grating replica could not be used with magnifications higher than 50,000, "1" nm gold-particles are used for calibration at higher magnifications. The calibration of "1" nm gold particles was performed by first calibrating a large population of "10" nm colloidal gold particles with a grating replica at 50,000 x magnification. Subsequently, a sample from the same "10" nm population was added to the cells bearing the "1" nm particles. The "10" nm particles served then as an internal reference.

## MATERIALS

The materials to be analyzed in the experiments are ultrathin sections of:

- a EPON-embedded Bio-standards loaded with the element of interest (Fe, Ca, Ce, etc).

The use of sectionable Bio-standards for quantitative X-ray microanalysis (XRMA) and electron energy-loss spectroscopic analysis (EELS) has been advocated by us earlier for a variety of reasons [De Bruijn (1981a-b, 1985); De Bruijn *et al.* (1983); De Bruijn & Cleton-Soeteman (1985); Cleton *et al.* (1986); Sorber *et al.* (1990b, 1991a-b)]. These Bio-standards:

- 1 can be loaded with a variety of elements;
- 2 have a known externally determined mean element concentration;
- 3 can aid in the conversion of relative to absolute element concentrations when co-embedded with cells or tissue containing the "unknown" concentration of that element;

- 4 can also be used as test-objects for instrumental variables, since both in EPMA and EELS, the mean  $R_x$ -ratio measured over several cross-sections is relatively constant (=  $R_x$  value).
- b Mouse virus-infected cell lines, which have reacted before embedding with a nominal 1 nm colloidal gold probe, directly conjugated with an anti-body (IC5) directed against viral-coat proteins;
- c Human vaginal epithelial cells which have reacted with colloidal thorium to visualize acid mucopolysaccharide negatively charged ligands [Van der Meijden *et al.* (1988); Groot (1981); Müller (1906)],
- d Rat iron-loaded liver parenchymal cells [Mostert *et al.* (1989); Ringeling *et al.* (1991); Cleton *et al.* (1986, 1989)],
- e Human liver siderosomes.
- f Fibroblasts.
- g Mouse peritoneal resident macrophages cell populations  
Integrated morphometric, multi-element analyses are performed with mouse peritoneal resident macrophage populations, treated with three simultaneously performed cytochemical reactions to detect different enzyme activities within one cell. Enzyme-related element-precipitations expected to be detected, differentiated and measured are:
  - 1 barium and sulphur from aryl sulphatase (AS) activity in rough endoplasmic reticulum (RER) stacks and lysosomes,
  - 2 cerium and phosphor from acid phosphatase (AcPase) activity in lysosomal precipitates,
  - 3 platinum from platinum di-amino-benzidine (DAB) complexes which are formed by endogenous peroxidase (PO) activity in macrophages, granulocytes and erythrocytes (see for cytochemical procedures [Van Dort *et al.* (1987, 1989); De Bruijn *et al.* (1986, 1987)]).

The biological specimens to be investigated are only glutaraldehyde-fixed. After ethanol dehydration the tissue is embedded routinely in EPON. In some cases, prior to embedding, dry Bio-standard-beads loaded with the element of interest are sprinkled around the cube of tissue. The small drop of EPON is first polymerized before the bulk of the capsule is completely filled and polymerized. The wet-sectioned, ultrathin sections are collected on unfilmed 400 mesh copper grids and used for morphometrical determinations, without any additional section staining. The morphometric procedures are applied to images from one of the

## Chapter 2

---

aforementioned imaging modes (global, zero-loss, ESI).

---

# **CHAPTER 3**

## **SPECTRAL ANALYSIS 1 OPTIMIZATION OF THE BACKGROUND-FIT**

CHAPTER 3

SPECTRAL ANALYSIS 1  
OPTIMIZATION OF THE BACKGROUND-FIT

This chapter has been published in *Journal of Microscopy* 162 (1991), p. 23-42.

*Quantitative analysis of electron energy-loss spectra from ultrathin-sectioned biological material. I. Optimization of the background-fit with the use of Bio-standards.*

Sorber C.W.J., Ketelaars G.A.M., Gelsema E.S., Jongkind J.F. and De Bruijn W.C.

SUMMARY

A computer program for quantitative spectral analysis (QSA) is proposed for the elemental analysis of biological material by electron energy-loss spectroscopy (EELS) in a conventional transmission electron microscope (CTEM), the Zeiss EM902. Bio-standards are used to test the performance of this program. The application of a Simplex optimization method for curve-fitting is proposed to separate the ionization edge from the background. Making use of Ce-, Ca- and Fe-Bio-standards, this method is compared to Egerton's well-known 2-Area method, the LogLog method and the Steepest descent method.

INTRODUCTION

*Background-fitting in the electron energy-loss spectrum*

Historically, quantitative spectral EELS-analysis has predominantly been concentrated on the curve-fitting procedures at the pre-ionization-edge (PIE) to acquire, after extrapolation beyond the ionization edge (IE), the core-loss ( $I_K$ ,  $I_L$ , etc) and background ( $I_B$ ) integrals as defined by Egerton [Egerton (1986)] (Fig.

1.5). Several background-fitting methods have been proposed to acquire a good fit for eq. 1.1:

- 1. Bevington proposed a linear least square fitting procedure with or without taking the logarithm of the data [Bevington (1969)] and recently Leapman & Ornberg elaborated on the same procedure [Leapman & Ornberg (1988)] (LogLog-method).
- 2. Egerton proposed the 2-Area-method as a faster method for background-fitting [Egerton (1986)]. In this method the part of the PIE-range used for the fit ( $\Gamma$ -range) is divided into two parts of equal width. The intensity-ratios of these two parts are used to calculate A and r for the fit.
- 3. Liu and Brown proposed improvements on the 2-Area-method for low edges or backgrounds that are highly influenced by other edges just in front of them, to make the method more accurate [Liu & Brown (1987)].
- 4. Colliex proposed to use the Steepest descent-method of Bevington [Colliex *et al.* (1981)].
- 5. Other valuable contributions are from : Leapman & Swyt (1988), Joy & Maher (1980), Ahn & Rez (1985), Steele *et al.* (1985), Reichelt & Engel (1984), Shuman & Somlyo (1987), Bentley *et al.* (1982), Berger *et al.* (1982).

When curve-fitting procedures in ultrathin sectioned biological material are applied, analysis of elements with their ionization edge beyond the Carbon-edge is influenced by the dominant presence of that Carbon-edge. To fit a function through this background, only a small part of the post-Carbon-edge may be usable as in the case of calcium of which the edge lies only 30 eV beyond the Carbon-edge. Therefore we propose the application of another method, namely :

- 6. The Simplex-method [Burton & Nickless (1987); Yarbo & Deming (1974); Shavers *et al.* (1979)].

Simplex optimization is a computational strategy to efficiently locate the optimum of a function of multiple parameters. It originates from the field of Operations Research [Dantzig (1683)], has since undergone various modifications and now exists in a number of variants [Spendley *et al.* (1962); Nelder & Mead (1965)]. A tutorial description of the "Modified Simplex Method" and of its use in Chemometrics may be found in [Burton & Nickless (1987); Morgan *et al.* (1990)]. In order to make this thesis as much as possible self-contained, the Simplex method, in a two-dimensional situation, as is the case in the present application, will be briefly reviewed.

### *Bio-Standards*

Several sections of Chelex<sup>100</sup> Bio-standards were measured with the QSA-module to obtain the inter-bead and the intra-bead variation in elemental concentration. The spectra of such Bio-standards can be used to test various instrumental conditions or the performance of a computational procedure.

In this study sectioned Bio-standards were used with the following purposes :

- 1. To show the usefulness of Bio-standards as a constant testing object.
- 2. To test a computer-program for EELS spectral analysis under various instrumental conditions.
- 3. To calibrate the spectrum.
- 4. To compare several background-fitting procedures.
- 5. To compare spectra of the Bio-standard H<sup>+</sup>-matrix to spectra of aldehyde-fixed cell-matrices.
- 6. To use Ca- and Fe-containing Bio-standards to determine "unknown" elemental concentrations.

### *The Simplex optimization procedure*

Initially, three pairs of parameter values for A and r of eq. 1.1 are chosen such that the three points in (A, r)-parameter space form a triangle (the Simplex), scaled in both directions by judiciously chosen step sizes. At these three initial points, a goodness function G is calculated, which in the present application is the sum of squares of deviations of the parametric curve from the spectrum as measured, where the summation extends over all points in the  $\Gamma$ -region. The technique then relies on the iterative displacement of the Simplex in parameter space, such that the goodness function is optimized. In the Modified Simplex Method, this displacement from one iteration to the other is governed by a set of rules, based on the relative merits of the three parameter combinations defining the current Simplex vertices. These merits, based on the goodness function G are ranked as best (B), next best (N) and worst (W) (Fig. 3.1). The next Simplex is formed by retaining the points B and N and by using the point M halfway between B and N as a reflection centre for W. In the Basic Simplex Method, the reflection point  $W_0$  is used as the third vertex (together with B and N) in the next Simplex (Fig. 3.1). This process is iteratively repeated until a preset criterion ( $t_G$ ) on the goodness function G is met (Fig. 3.2).

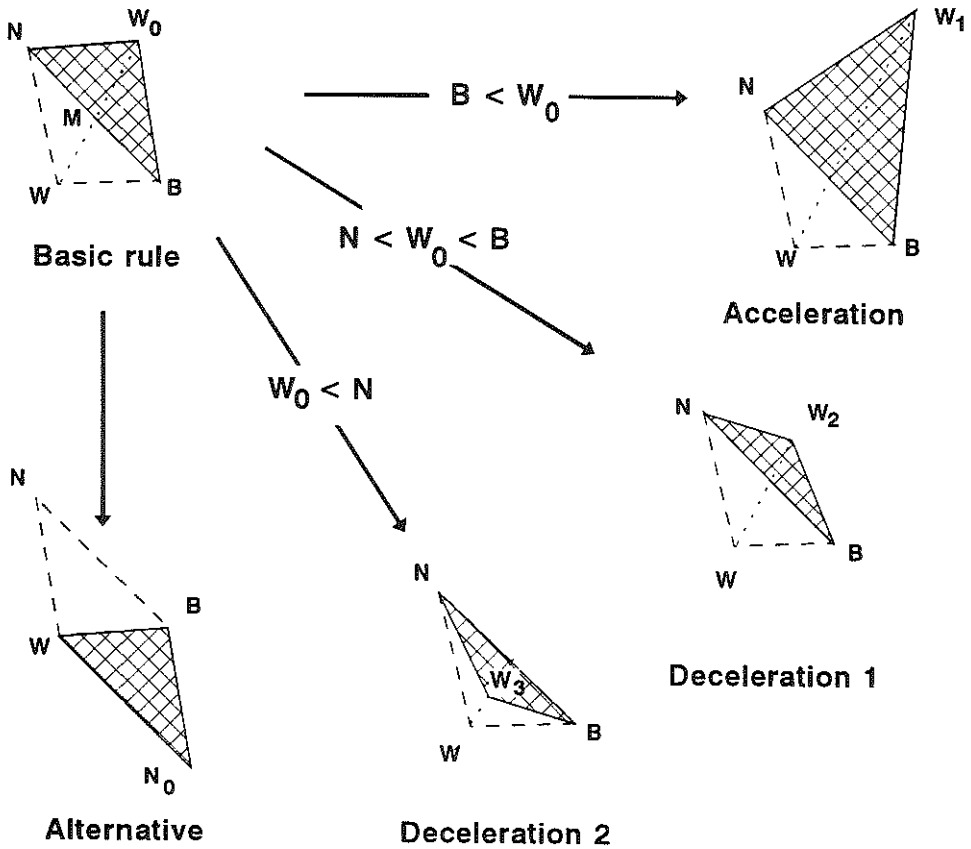


**Figure 3.1,** Illustration of the various rules governing the Simplex displacement between iterations. The Simplex in the current iteration is shown in dotted lines, the new Simplex is hatched. B is the best, N is the next best, W is the worst combination for A and r. The middle of vertex B-N is indicated by M.

The Modified Simplex Method used here brings some refinements to the basic principle, in order to accelerate the process in regions far from the optimum (expansion) and to decelerate in the region of the optimum (contraction). The "alternative" rule prevents the process from preliminary oscillations.

**Acceleration:** If  $W_0$  is the best vertex in the new Simplex, then in addition the point  $W_1$  ( $MW_1 = 2 * MW_0$ ) is also evaluated. If  $W_1$  is still the best,  $W_1$  is taken

## Chapter 3

---

as the third vertex before the next iteration is started. If not,  $W_0$  is retained.

**Deceleration 1:** If  $W_0$  is the next best in the new Simplex, the point  $W_2$  ( $MW_0 = 2 * MW_2$ ) is evaluated. If it is better than  $W_0$ ,  $W_2$  is taken as the third vertex in the next Simplex. Otherwise, the deceleration fails.

**Deceleration 2:** If  $W_0$  is the worst vertex in the new Simplex, then according to the basic rule it would be reflected, returning to  $W$  and the process would start to oscillate. In order to prevent this, the point  $W_3$  ( $WM = 2 * WW_3$ ) is evaluated. If  $W_3$  is better than  $W$ , it is taken as the third Simplex vertex; if not, the deceleration fails.

**Alternative:** In cases of a failing deceleration, the original point  $W$  is retained,  $N$  is discarded and the third new Simplex vertex is  $N_0$ , the reflection of  $N$ .

In Fig. 3.2 part of a theoretical Simplex-pathway is shown using the rules mentioned above. The dotted lines are lines of equal goodness  $G$  in the parameter space. The optimum is marked by "\*". The start-Simplex (1) is first reflected following the acceleration rule forming Simplex (2) and quickly finds its way to the optimum following the rules described above. As mentioned earlier, for the Simplex-method the basis for evaluation is the goodness function  $G$  and the iterative process is discontinued if a vertex is found for which the value of  $G$  is better than a preset threshold  $t_G$ . In the experiments to be described in the following sections, the influence of  $t_G$  on the final result has been investigated.

The 2-Area method relies on the relation between only two roughly estimated areas of the energy-loss spectrum for the estimation of the parameters  $A$  and  $r$ , whereas the Simplex-method uses every available datapoint of the spectrum for the extrapolation into the  $\Delta$ -region. Therefore the Simplex method may be expected to be more accurate than the 2-area method. This will be verified in the following sections, where experiments with different types of spectra will be described.

## MATERIALS AND METHODS

### *Chelex<sup>100</sup>-based-Bio-standards*

In this study it was examined whether the ultrathin-sectioned Bio-standards may

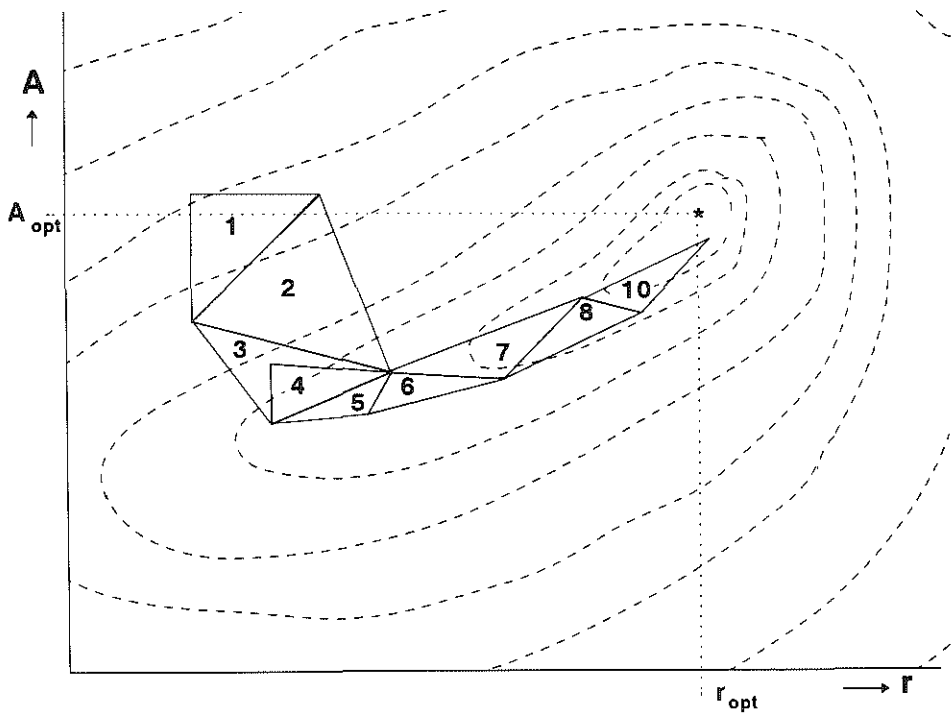


**Figure 3.2,** Example of a Simplex-pathway. The parameter-combinations ( $A$ ,  $r$ ) are changed until the optimum (\*) is reached. The dotted lines are lines of equal goodness  $G$  in parameter space. See text for an explanation of the various rules applied here.

be used as a means of standardizing some of the instrumental conditions in relation to the implementation of a computer program for EELS analysis and as a means to compare the various spectrum characteristics, such as the  $R_x$ -value,  $A$  and  $r$  of the background-fit.

### *Experiments*

#### •1 Accuracy of $R_x$ -determination

A Bio-standard loaded with Iron and another loaded with Calcium were used to determine the accuracy of the relative concentration ( $R_x$ ) for both the 2-Area-method and the Simplex-method. Several such Bio-standard sections in one ultrathin section were measured to obtain the inter-bead and the intra-bead covariation of elemental concentration

### •2 Influence of instrumental conditions on the sensitivity of the measurements

To monitor the influence of instrumental conditions on the acquired mean  $R_x$ -values of the Bio-standards, relative concentrations obtained with objective-lens diaphragms of 30-60-90 $\mu\text{m}$  ( $\mathcal{O}_{\text{O.L.}}$ ), corresponding with aperture variations of 5-20-30 mrad, were compared with respect to the relative concentration. The measurements were done in sequence from 30-60-90 $\mu\text{m}$  and from 90-60-30 $\mu\text{m}$  respectively, at the same sites and under the same conditions.

### •3 Energy-scale calibration

To calibrate the energy-loss scale, a spectrum which contained two edges (Cerium and Carbon) was recorded. The distance between the two edges was obtained from the spectrum and compared to the known value.

### •4 Comparison of the Simplex-method to three conventional methods applied to the same set of spectra

To fit a function through the background one must first determine the  $\Gamma$ -range which is available for the fit (Fig. 1.5). Four methods were compared: The 2-Area method, the Steepest descent method, the LogLog-method and the Simplex method.

To compare the fitting-methods, the A, r and  $R_x$ -values were calculated at a constant  $\Delta$ -range of 50 eV while the width of the  $\Gamma$ -range was deliberately changed from 5 to 100 eV, for all four methods. Further the maximum error ( $t_{\sigma}$ ) which is allowed during the Simplex-fit was changed in order to obtain the best result. The Simplex-fitting results of one spectrum were compared for  $t_{\sigma}$ -values of  $10^{-1}$ ,  $10^{-2}$ ,  $10^{-4}$ ,  $10^{-6}$ ,  $10^{-8}$ , respectively and compared to those from the other methods. Similar comparisons were performed on recorded Fe- and Ca-spectra. To establish that the QSA-program was able to perform the requested fitting with sufficient accuracy, an artificial test-spectrum was made simulating the function  $I(E) = 450 * E^{-4.5}$ , which was assumed to approach the function for an Fe-spectrum in biological material. The aim was to find the minimal  $\Gamma$ -value for a reliable calculation of the A and r-values and to check whether the  $R_x$ -value from then on remained constant.

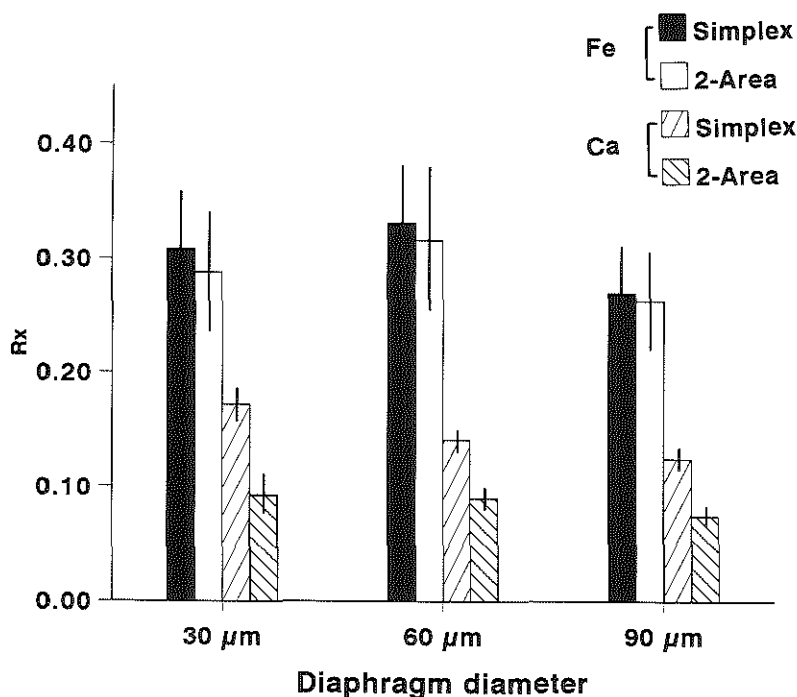


**Figure 3.3,** The mean  $R_x$ -ratio of 25 spectra acquired at three different objective-lens diaphragms for Ca-spectra and Fe-spectra. The vertical bar represents the standard deviation of the 25 values obtained at each diaphragm setting.

## RESULTS

### •1 Accuracy of $R_x$ -determination

The inter-bead and the intra-bead covariation of the elemental concentration in the Iron and Calcium Bio-standards were both 12%-20% ( $n=20$ , Simplex-method).

### •2 Influence of instrumental conditions on the sensitivity of the measurements

To monitor the influence of instrumental conditions, the acquired mean  $R_x$ -values of the Bio-standards obtained with objective-lens diaphragms of 30-60-90 $\mu\text{m}$  ( $\mathcal{O}_{\text{O.L.}}$ ) corresponding with aperture variations of 5-20-30 mrad, were compared. The measurements were done in sequence from 30-60-90 $\mu\text{m}$  and from 90-60-30 $\mu\text{m}$  respectively to reduce the influence of radiation damage, at the same sites and under the same conditions.

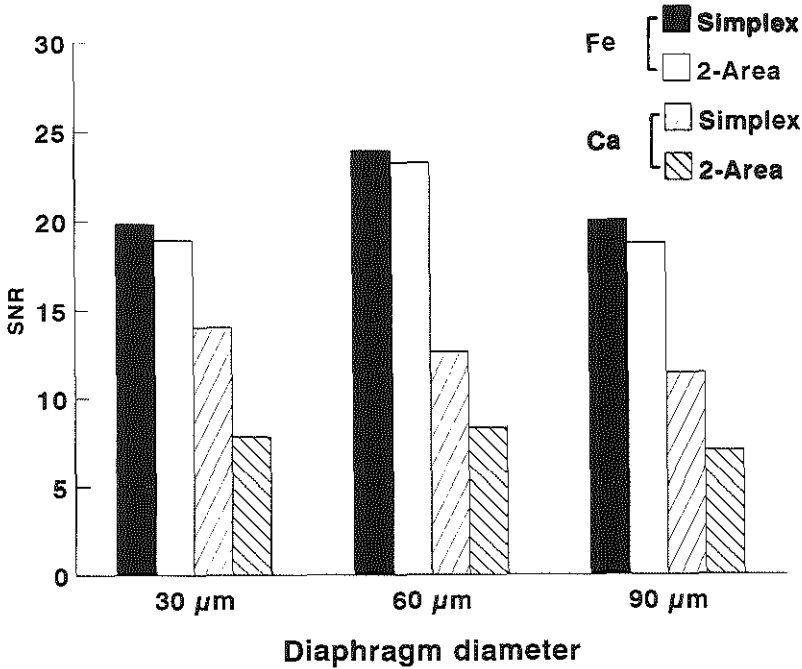


**Figure 3.4.** The Signal-to-noise ratio (SNR) of the 25 Ca- and Fe-spectra as shown in Fig. 3.3. Two curve-fitting-methods are applied to the same spectra: the Simplex- and the 2-Area-method. ( $\Gamma_{\text{Ca}}=25$  eV;  $\Gamma_{\text{Fe}}=50$  eV;  $\Delta=50$ ). The SNR is calculated according to Egerton (1986, p.494) ( $h=14$ ).

The results are given in Fig. 3.3 for Calcium and Iron. The highest mean  $R_{\text{Ca}}$ -value was found with a 30 $\mu\text{m}$  diaphragm. The  $R_{\text{Ca}}$ -values tend to decrease with increasing objective-lens diaphragm. The  $R_{\text{Ca}}$ -values of the Simplex-method were significantly higher than those of the 2-Area-method. Since the Ca-PIE is greatly influenced by the C-edge and therefore has a strong curvature, the 2-Area-method induces a large error because it takes only three data-points in consideration, while the Simplex uses all the data-points. The  $R_{\text{Fe}}$ -values of the Simplex-method were not significantly higher than those of the 2-Area method. The  $R_{\text{Fe}}$ -values for the different diaphragms were not significantly different ( $p>0.05$ ).

In Fig. 3.4, the signal to noise-ratios (SNR) are given for 25 such spectra. SNR is calculated according to Egerton (1986) ( $h=14$ ).

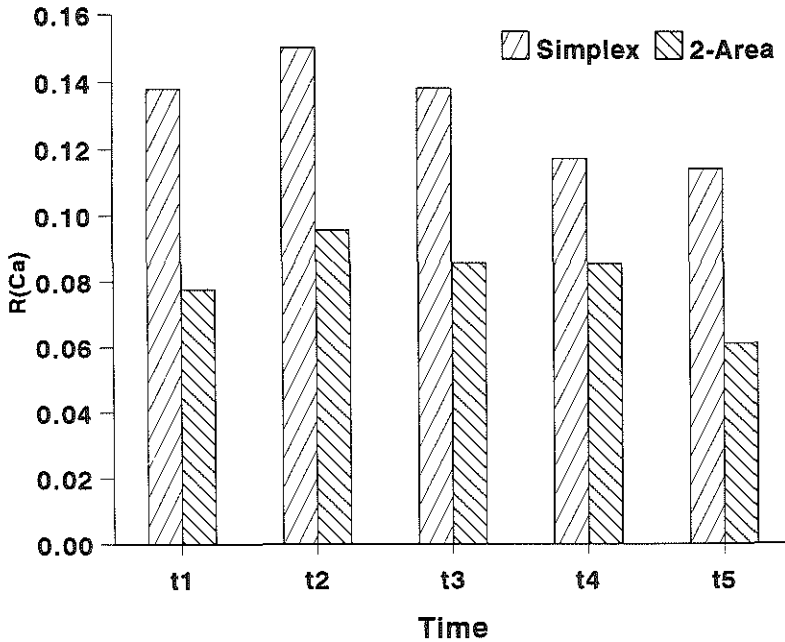
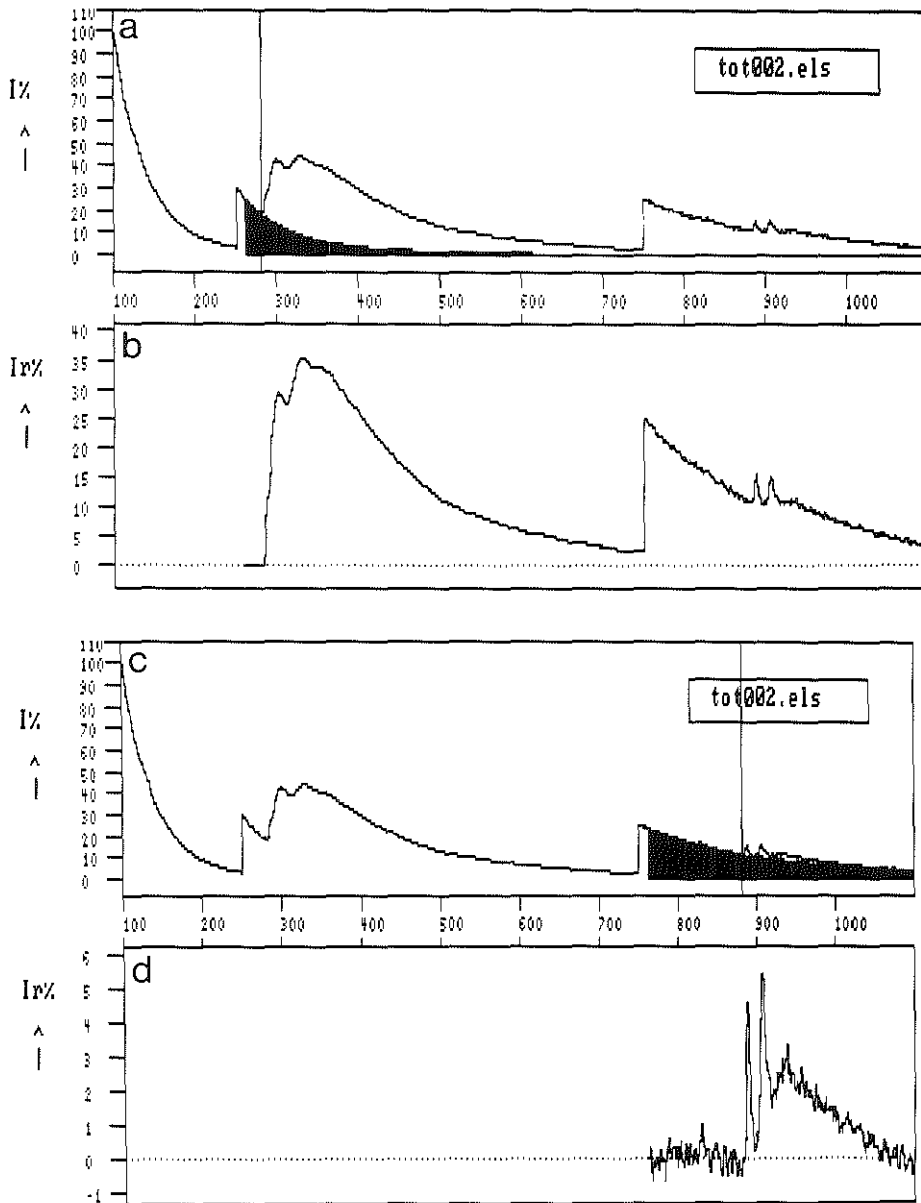


**Figure 3.5.** The mean  $R_{Ca}$ -values obtained from 10 analyzed areas in one section of a calcium-containing standard (6.13 wt%) during 5 consecutive analyses. Two curve-fitting methods are applied to the same spectra: the Simplex- and the two-area method.  $\Gamma = 25$  eV;  $\Delta = 50$  eV;  $\Phi_{O.L.} = 90 \mu\text{m}$ .

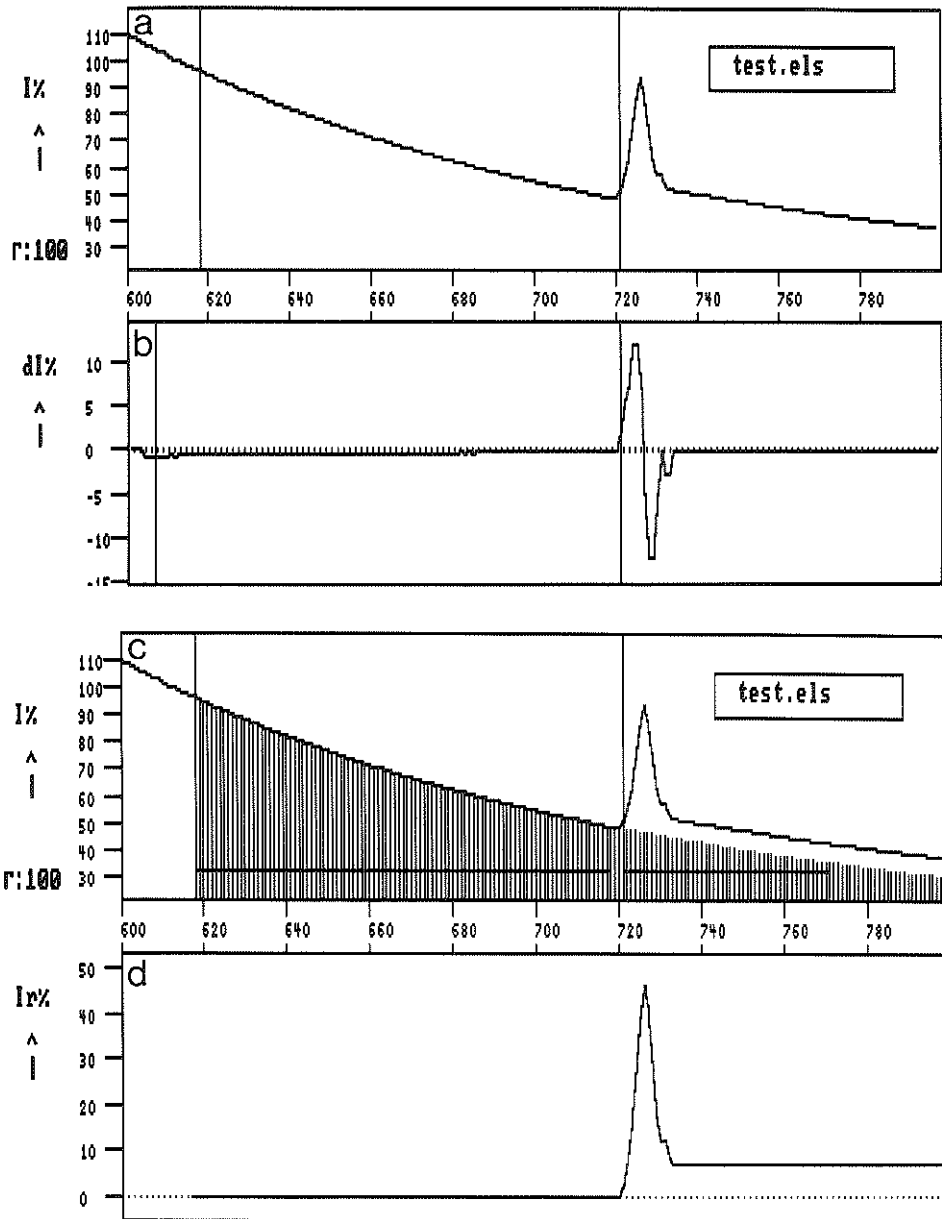
In Fig. 3.5, 10 sectioned beads in one section of a Calcium Bio-standard are measured in 5 time sequences to show the influence of mass loss, expressed as the  $R_{Ca}$ -ratio change, for both the Simplex- and the 2-Area-method ( $\Gamma=25$  eV;  $\Delta=50$  eV;  $\Phi_{O.L.}=90\mu\text{m}$ ). The radiation damage is visible after five measurements as a reduction in the mean  $R_{Ca}$ -value. The electron dose was  $1.6 \cdot 10^{-11}$  C/s  $\mu\text{m}^2$  (magnification = 30.000x) [Cantow (1991)].

### •3 Energy-scale calibration

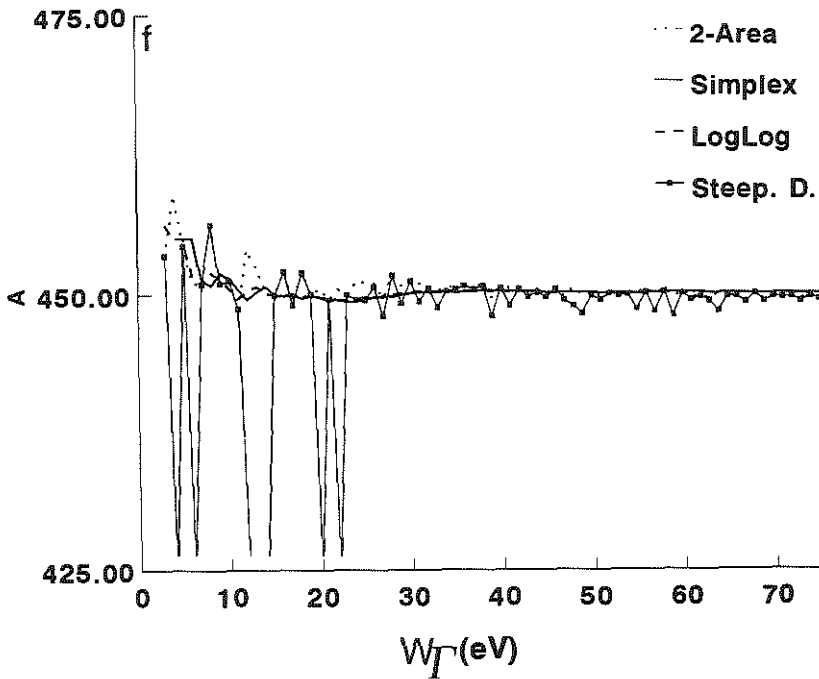
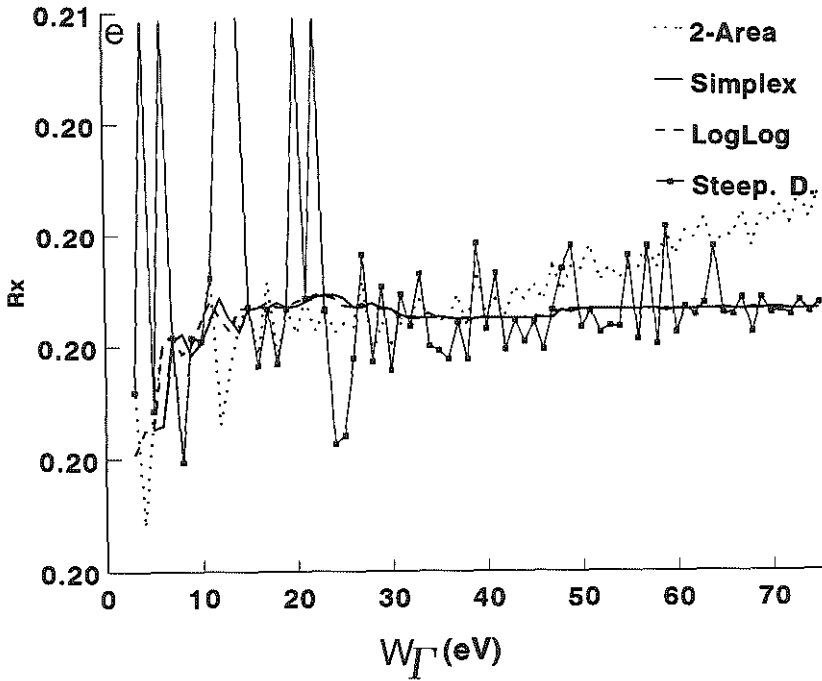
To calibrate the energy-loss scale, a spectrum with both cerium- and carbon-edges was recorded (Fig. 3.6). The distance between the two edges was compared to the known distance (C : 284 eV, Ce : 883 eV; distance = 599 eV). The measured distance was 602 eV which gives a difference of 0.5% ( $\Phi_{O.L.}=90\mu\text{m}$ ).



**Figure 3.6,** Ce- and C-edges in one spectrum for energy-scale calibration. (a) The extrapolation of the PIE of carbon; (b) The subtracted C-spectrum; (c) The extrapolation of the PIE of cerium; (d) The subtracted Ce-spectrum (d). The deviation of the energy-loss scale was 0.5 % ( $\Phi_{O.L.} = 90 \mu\text{m}$ ).



**Figure 3.7,**  $R_x$ -value versus width of the  $\Gamma$ -range for the Simplex-method ( $t_G=10^{-6}$ ), the 2-Area-method, the LogLog-method and the Steepest descent-method. Test spectrum ( $A=450$ ;  $r=4.5$ ); (a-d): processing of the spectrum as described in chapter 2.



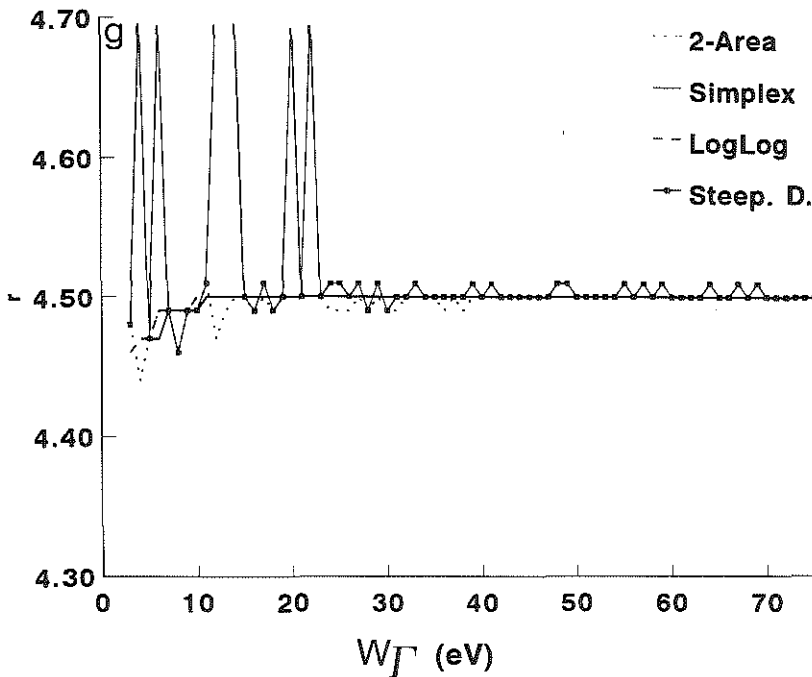


**Figure 3.7** (continued), (e): Simplex-method compared to the two-area-method, the LogLog-method and the Steepest descent-method.  $R_x$  is shown as a function of  $W_\Gamma$ ; (f-g) The variation in A (f) and the variation in r (g) as a function of  $\Gamma$ .

Similarly, the distance of the Ce-N<sub>4,5</sub> to Carbon was calibrated. From this spectrum also the gain-factors could be checked. The standard-deviation of the gain-factors was < 3%.

#### •4 Comparison of the Simplex-method to three conventional methods applied to the same set of spectra

Several spectra were processed various times while the  $\Gamma$ -range was varied. The relation between the width of the  $\Gamma$ -range and the measured  $R_x$ -value was plotted.

First we used an artificial spectrum "Test.els" following an inverse power law with known constants A and r (Fig. 3.7):

$$I(E) = 450 * E^{-4.5}$$

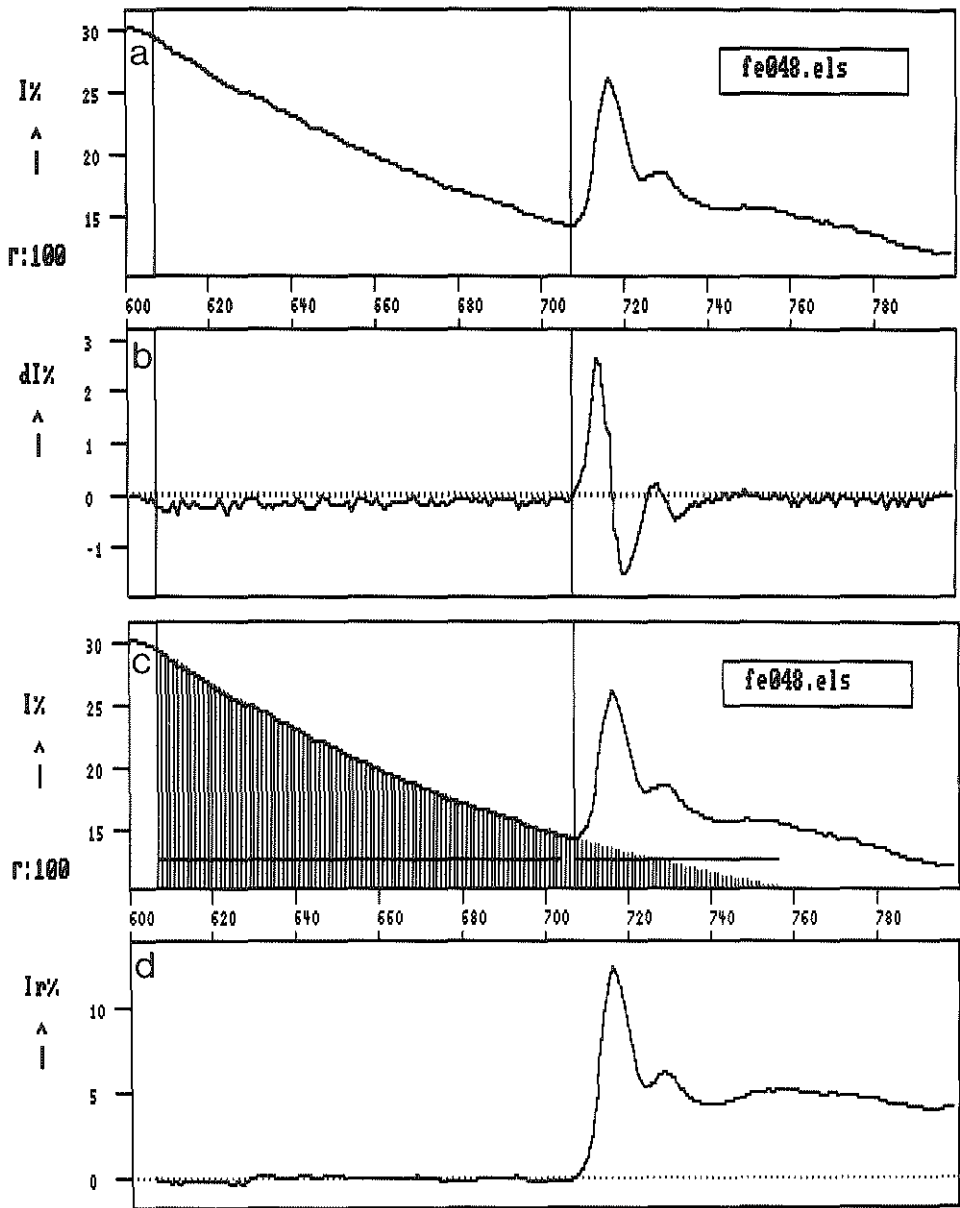
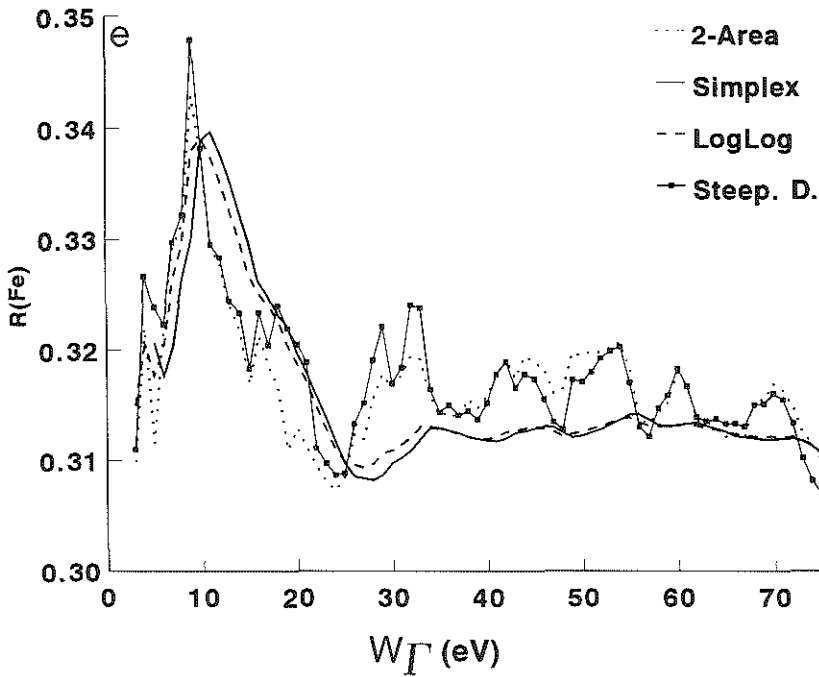


Figure 3.8,  $R_{Fe}$ -value as a function of the width of the  $\Gamma$ -range for the two-Area-method, the LogLog method, the Steepest descent method and the Simplex-method ( $t_G = 10^{-6}$ ). Iron spectrum; (a-d): processing of the Fe-spectrum as described in chapter 2 using the Simplex-method for the continuum-fitting.



**Figure 3.8** (continued), (e): Simplex-method ( $t_G = 10^{-6}$ ) compared to the two-area-method, the LogLog method and the Steepest descent method. The  $R_{Fe}$  is shown as a function of  $W_\Gamma$ .

The results of the  $\Gamma$ -variations ( $\Delta$ -range = 50 eV), shown in Fig. 3.7e-g, demonstrate that, with the Simplex method and the LogLog method, for  $\Gamma \geq 15$  eV the input-values were found. The Steepest descent method frequently shows deviations from these input values. The 2-Area method tends to deviate from the input values with increasing  $W_\Gamma$ . This experiment was repeated for spectra of Fe- and Ca-Bio-standards leading to a similar set of data (Fig. 3.8 and 3.9). For the Fe-spectrum of Fig. 3.8,  $R_{Fe}$ -values for different settings of  $t_G$  are shown in Fig. 3.10. The differences between  $t_G = 10^{-4}$ ,  $10^{-6}$ ,  $10^{-8}$  are too small to be visible in Fig. 3.10. For that reason only the  $t_G$  of  $10^{-2}$  and  $10^{-4}$  are shown. As may be seen in Fig. 3.10,  $t_G$  must be  $10^{-4}$  or smaller to obtain a good fit.

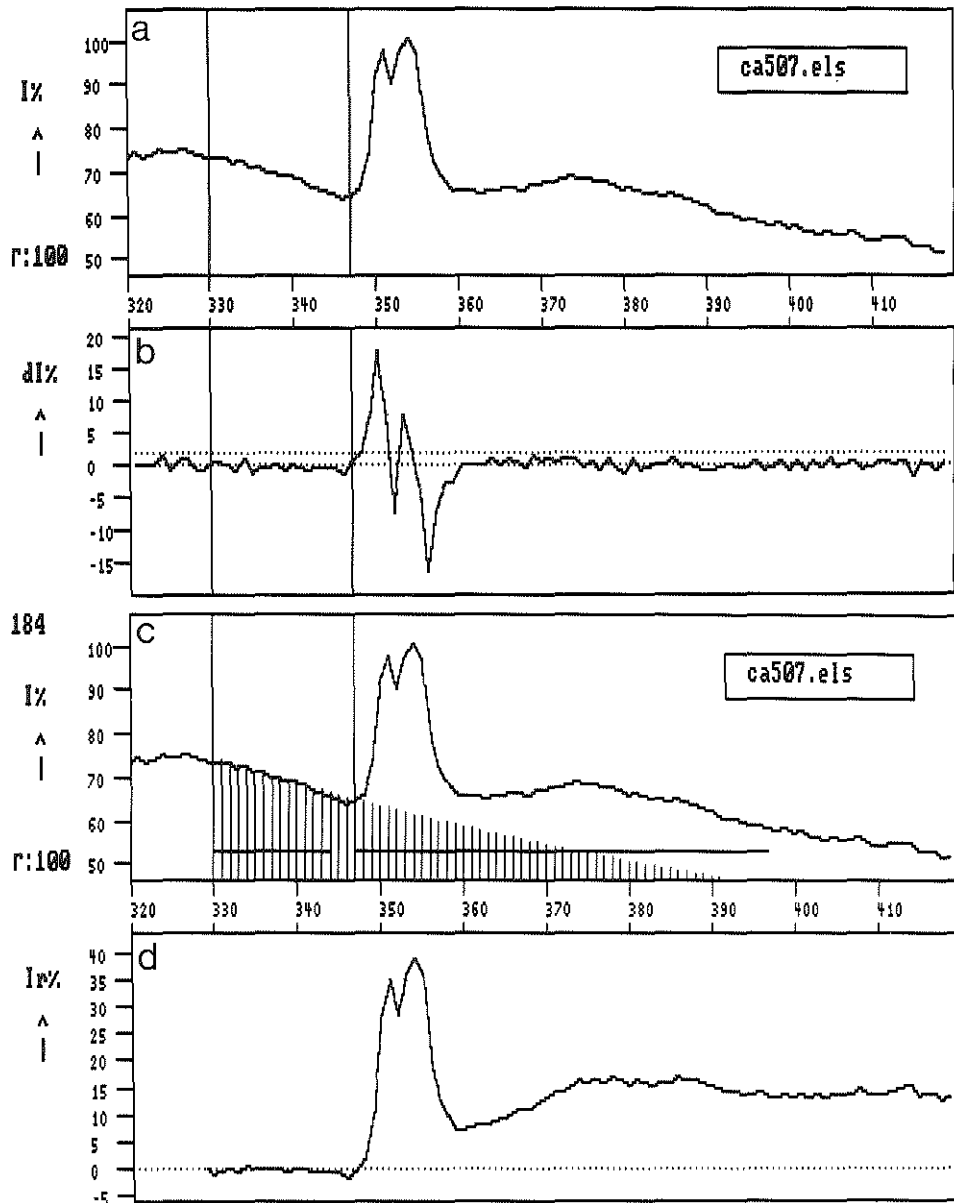
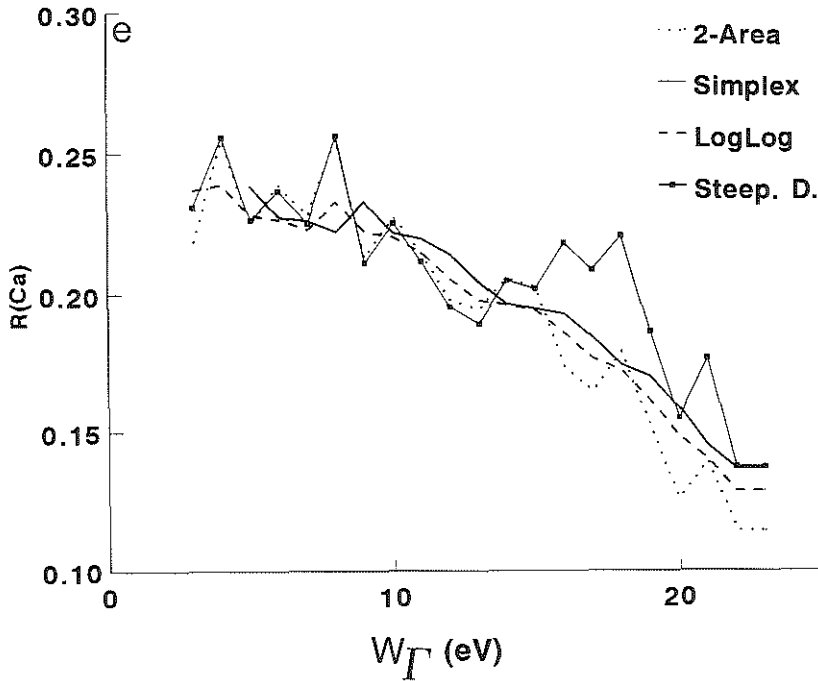


Figure 3.9,  $R_{Ca}$ -value as a function of the width of the  $\Gamma$ -range for the 2-Area-method, the LogLog method, the Steepest descent method and the Simplex-method ( $t_G = 10^{-6}$ ). Calcium spectrum; (a-d): processing of the Ca-spectrum as described in chapter 2 using the Simplex-method for continuum-fitting.



**Figure 3.9 (continued) (e)** Simplex-method ( $t_G = 10^{-6}$ ) compared to the 2-Area-method, the LogLog method and the Steepest descent method. The  $R_{Ca}$  is shown as a function of  $W_{\Gamma}$ .

## DISCUSSION

In EEL-spectra, for curve-fitting of the background in front of a given edge, an inverse power law of the form  $I(E) = A * E^{-r}$  is applied. This works adequately for edges that are widely separated in energy-loss ( $> 100$  eV). However, in biological specimens, edges often are too close together to fit the background properly. Furthermore, core-losses and plasmon-losses influence the fit e.g. as for the carbon edge at 284 eV and the calcium edge at 346 eV. So a fitting method is required that can use every channel available. Like the LogLog-method, the Simplex method fulfils this criterion. Moreover, from the comparison with the test-spectrum (Fig. 3.7) we can conclude that :

1. The accuracy of estimates of  $R_x$ ,  $A$  and  $r$  of the Simplex-method and LogLog-method are within a range of 0.5 % after about 15-20 eV ( $t_G = 10^{-6}$ ).

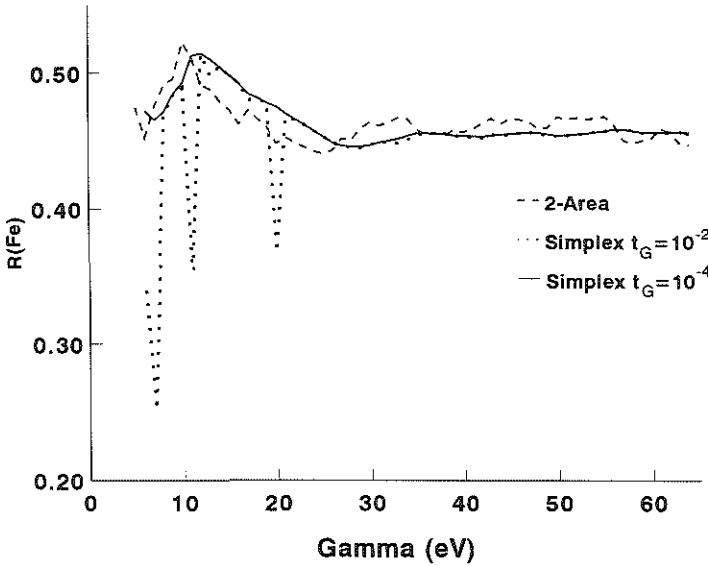


**Figure 3.10**, Illustration of the influence of the value of  $t_G$  on the Simplex-method using Fig. 3.8. For comparison, the results of the two-Area-method are shown as well.

2. For  $\Gamma$ -ranges larger than 20 eV, the values acquired after application of the Simplex-method are virtually independent of the width of the  $\Gamma$ -range, while for the 2-Area-method both  $A$ ,  $r$  and  $R_x$  tend to fluctuate.
  3. The Steepest descent method frequently tends to deviate from the optimum combination for  $A$  and  $r$ , leading to inaccurate estimations for the continuum.
  4. The 2-Area method tends to deviate from the input values with increasing  $W_\Gamma$ .
- From the fits of the real curves of Fe (Fig. 3.8) and Ca (Fig. 3.9) we can conclude that:
3. The  $A$ ,  $r$  (not shown) and  $R_x$  values are less constant than those calculated for the test-spectrum.
  4. For Iron the minimum  $\Gamma$ -range used in the Simplex-fit is slightly larger than for the test-spectrum, while for Calcium the maximum possible  $\Gamma$ -range does not (yet) lead to a constant value for  $R_{Ca}$ ,  $A$  and  $r$  ( $A$  and  $r$  are not shown).
  5. When  $t_G$  is made smaller,  $R_x$ ,  $A$  and  $r$  values become constant after a shorter  $\Gamma$ -range (Fig. 3.10).
  6. The overall conclusion is that the Simplex-method is comparable to the LogLog

method and gives better results than the 2-Area-method and the Steepest descent-method. For some spectra the difference is marginal, for others it is significant.

7. An additional improvement is that the accuracy can be improved by diminishing  $t_G$ , although at the cost of increasing processing-time.

For these experiments the Bio-standards were good test-objects. We can conclude from the experiments performed with these Bio-standards that :

- a. Radiation damage is present after 5 sets of measurements, but is reasonably under control ( $\pm 20\%$ ).
- b. To average out the influence of radiation damage, the spectra were recorded from 30-60-90 $\mu\text{m}$  and from 90-60-30 $\mu\text{m}$ . The radiation damage itself is not dependent on the size of the objective-lens diaphragm since this diaphragm is situated under the specimen. Another solution for radiation damage is to take different spots in the same bead for each objective-lens diaphragm or to take different beads for each diaphragm.
- c. By varying the diameter of the objective-lens diaphragm, the 30 $\mu\text{m}$  diaphragm gave the highest  $R_{\text{Ca}}$ -value. An explanation for this might be that a spectrum recorded with a 30 $\mu\text{m}$  diaphragm has a higher resolution than a spectrum recorded with a 60 or 90 $\mu\text{m}$  diaphragm, leading to a steeper descent of the edges in front of the edge of interest such as is the case with calcium. A steeper descent leads to a steeper extrapolation beyond the IE which leaves more signal being addicted to the  $I_L$ . The measured  $r$ -values for Ca are  $4.98 \pm 0.19$  and  $3.99 \pm 0.20$  for  $\varnothing_{\text{O.L.}} = 30$  and  $90 \mu\text{m}$  respectively and for Fe  $4.31 \pm 0.31$  and  $4.88 \pm 0.36$  for  $\varnothing_{\text{O.L.}} = 30$  and  $90 \mu\text{m}$  respectively. This could be the reason for the change in  $R_{\text{Ca}}$ -values with a varying objective-lens diaphragm while  $R_{\text{Fe}}$ -is hardly influenced at all.  
This steep descent induces a larger standard deviation which is why we recommend the 90  $\mu\text{m}$  diaphragm. Another reason for this recommendation is the fact that with a 90  $\mu\text{m}$  diaphragm the electron-intensity is the highest.
- d. The calibration of the eV-scale using a spectrum containing both carbon and cerium showed a difference of 0.5%.
- e. Bio-standards can be used to compare background-fitting-methods.
- f. For a set of sectioned-beads,  $R_{\text{Ca}}$  and  $R_{\text{Fe}}$  are more or less constant although the inter-bead variation and intra-bead variation in elemental concentration are 12%-20%. A large contribution to this variation comes from the concentration

covariation within and between the individual beads since the standard deviation of the concentration in the Bio-standard itself has been reported to be 12-16% [De Bruijn (1981); De Bruijn & Cleton (1985); Blaineau *et al.* (1987)].

- g. The beads and their ultrathin sections can be used to compare results with different instruments.

Almost every process requires the optimization of a system's response (called the dependent variable) as a function of several experimental factors (the independent variables). The use of Chelex-based Bio-standards allows system response optimization. The Simplex optimization is a way to select the optimal settings among a set of independent parameters. In our experiments there are two such parameters, i.e.  $A$  and  $r$ . For these parameters the optimal combination is formed for a minimum least square value tolerated by the specified value of  $t_G$ . The general principle of this process is illustrated in Fig. 3.1. When the  $\Gamma$ -range is constant e.g. 50 eV, the optimal fit is obtained and accordingly  $R_x$  is established. In these experiments an additional parameter was included by varying the  $\Gamma$ -range from 5 eV to 100 eV (if available !). In this way the minimal width of the  $\Gamma$ -region for a consistent fit can be established. In a similar way the results of the 2-Area method were processed by stepwise increasing the  $\Gamma$ -region by 2 eV.

Recently some articles related to (EELS) signal optimisation have appeared [Pun *et al.* (1985); Burton & Nickless (1987); Shuman & Somlyo (1987); Trebbia (1988); Leapman & Swyt (1988)]. In these papers excellent surveys of the various statistical approaches may be found. Although a Simplex optimisation is mentioned by Fiori *et al.* (1981) and Leapman *et al.* (1984) for X-ray spectra, the paper of Burton & Nickless (1987) prompted us to apply it to EEL-spectra. We had not the intention to prove the superiority of one of the four chosen methods, but to find quality criteria of good use in practice.

---

# **CHAPTER 4**

## **SPECTRAL ANALYSIS 2 THE APPLICATION OF BIO-STANDARDS**

## CHAPTER 4

### SPECTRAL ANALYSIS 2

#### The application of Bio-standards for quantitative analysis.

This chapter has been published in *Journal of Microscopy* **162** (1991), p. 43-54.

*Quantitative analysis of electron energy-loss spectra from ultrathin-sectioned biological material. I. The application of Bio-standards for quantitative analysis.*

Sorber C.W.J., Ketelaars G.A.M., Gelsema E.S., Jongkind J.F. and De Bruijn W.C.

#### SUMMARY

Electron energy-loss spectroscopy (EELS) has been applied to determine elemental concentrations in a true biological situation, viz. ultrathin sectioned cells and tissues. Chelex<sup>100</sup>-based Ca- and Fe-Bio-standards are used for elemental quantification to establish iron and calcium concentrations. These Bio-standards as well as the biological materials are treated in a standard EM-procedure such that "known" and "unknown" sites are localized in one ultrathin section.

Uncertainties and variabilities present in the equations that calculate the concentration in the "unknown" site by comparing Simplex-fitted EEL-spectra from Bio-standards with those from tissue, are outlined in two examples. With the use of a H<sup>+</sup>-Bio-standard, the matrix composition of such biological cell material is analyzed, leading to values, which approach each other closely. Quantitative EELS, using Chelex<sup>100</sup>-based Bio-standards, is advocated.

#### INTRODUCTION

Electron energy-loss spectroscopical (EELS) analysis of elements in ultrathin LX-112 (EPON) sections containing single cells and/or tissue is rather complicated.

Three categories of elements can be analyzed:

- a water-soluble ions,
- b water-insoluble crystalline materials,
- c water-insoluble elements bound to a proteinaceous matrix

In ultrathin sectioned EPON-embedded material, containing endogenous or exogenous elements, EELS analysis is restricted to those of type •b and •c.

The role of Bio-standards as a means to standardize instrumental (EELS) conditions and its use as a freely exchangeable specimen of known composition with an objectively externally-determined element concentration has been shown in the previous chapter [Sorber *et al.* (1991a)]. In this chapter we will elaborate upon the role of Bio-standards to determine, by quantitative EELS analysis, the "unknown" elemental concentration in a cell, by comparing its spectral characteristics with that of the "known" concentration of the element in the ultrathin sectioned Bio-standard present in the same section.

Three questions will be answered:

- 1 Does the matrix composition of the H<sup>+</sup>-Bio-standard, containing the elements C, O, N and H, have a sufficient similarity to the matrix composition of a "Cell"?
- 2 Is it possible to use the iron-containing Bio-standard to determine the iron concentration in co-embedded ferritin particles? How close is this acquired value, to the mean biochemical ferritin-iron value?
- 3 Is it possible to measure the calcium concentration in proximal tubule cells containing calcium containing stone primordia using a calcium containing Bio-standard? How does this result deviate when small pure calcium oxalate monohydrate crystals are analyzed in a similar way?

### *Theoretical considerations*

For quantitative EELS analysis the number of atoms of element x ( $N_x$ ) per unit area is defined by:

$$N_x = \frac{I_K}{I_T} \cdot \frac{1}{\sigma_x(\beta, \Delta)} \quad (4.1)$$

In which  $I_K$ ,  $I_L$ , etc. is the edge intensity,  $I_T$  is the total intensity,  $\sigma_x$  is the "partial" cross-section of element x,  $\beta$  is the aperture present during spectrum acquisition and  $\Delta$  is the width of the integration region. For a definition of  $I_K$  and  $I_T$  see Fig. 1.5.

## Chapter 4

---

Similarly, when a second element (y) is present in the irradiated area, its number of atoms is proportional to:

$$N_y = \frac{I_K}{I_T} \cdot \frac{1}{\sigma_y(\beta, \Delta)} \quad (4.2)$$

In which  $\sigma_y$  is the "partial" cross-section of element y. When absolute values of N are not required, the ratio of two elements in the same irradiated area can be found according to:

$$\frac{N_x}{N_y} = \frac{I_{K(x)} \cdot \sigma_y(\beta, \Delta)}{I_{K(y)} \cdot \sigma_x(\beta, \Delta)} \quad (4.3)$$

In the situation in which two sites with different numbers of the same element x ( $N_{x,1}$  and  $N_{x,2}$ ) in one ultrathin section within two, equally sized analyzed areas, are compared, the two numbers are related as follows:

$$\frac{N_{x,1}}{N_{x,2}} = \frac{I_{K(1)} \cdot I_{T(2)}(\beta, \Delta)}{I_{K(2)} \cdot I_{T(1)}(\beta, \Delta)} \quad (4.4)$$

When one of the sites is the location of a standard with a known externally determined number of element x, (e.g.  $N_{x,2}$ ), the unknown number of elements ( $N_{x,1}$ ) can be found according to:

$$N_{x,1} = \frac{I_{K(1)} \cdot I_{T(2)}(\beta, \Delta)}{I_{K(2)} \cdot I_{T(1)}(\beta, \Delta)} \cdot N_{x,2} \quad (4.5)$$

When two elements are present in one irradiated area, there is only one  $I_T$  value. In this case, strictly speaking  $I_{T(1)}$  is different from  $I_{T(2)}$ . Nevertheless, it is worthwhile to investigate whether, when measured in practice, this difference between  $I_{T(1)}$  and  $I_{T(2)}$  has such a crucial influence on the final result that elimination is forbidden. Especially since in our instrument, like in other instruments with a serial detection system,  $I_T$  has to be measured in a second run, or with a different detector and different gain factor, at the same time. Theoretically, parallel detection might eliminate this problem.

If the mean concentration (C) of the loaded Bio-standard with element x within the analyzed area is determined with neutron activation in wt%, a conversion into atoms/nm<sup>2</sup> (N) is needed:

$$N_x = \frac{t \cdot \rho \cdot C \cdot N_A}{A} \quad (4.6)$$

where  $t$  is the thickness of the specimen,  $\rho$  is the specific density of the Bio-standard,  $N_A$  is Avogadro's number and  $A$  is the atomic mass of the element  $x$ . The thickness ( $t$ ) of the specimen can then be calculated according to Leapman *et al.* (1984a):

$$t = \lambda_{in}(\beta, \Delta) \ln \frac{I_T}{I_0} \quad (4.7)$$

where  $\lambda_{in}$  is the total inelastic mean free path for the collection angle  $\beta$  and width of the integration region ( $\Delta$ ). The method to determine  $\rho$ -values of Bio-standards (though of a different type of bead material) have been outlined before [De Bruijn (1981a, 1981b)].

The application of eq. 4.5 assumes that in both analyzed areas (1 and 2) the element is homogeneously distributed. If that is not the case, like in our experiments with the pea-seed ferritin particles, the concentration of the unknown biological material can still be calculated following eq. 4.5, but for the conversion to atoms per ferritin core, the number of cores counted in the analyzed area must be acquired and the parameters of eqs. 4.6 and 4.7 must be calculated. This value may then be compared with the biochemical value. Due to the large number of uncertainties in the latter calculations as discussed before [Egerton (1986); Sorber *et al.* (1990a)] we prefer, for the time being, to postpone this conversion from wt% to  $N_{Fe}$  until more information about the parameters of eqs. 4.6 and 4.7 ( $\rho$ ,  $t$  and the precise analyzed area) is collected.

Another aspect in quantitative EELS analysis of biological material is related to the dominant presence of matrix elements in addition to the element of interest. For the background integral  $I_B$  an equation analogous to Eq. 4.1 can be written:

$$I_B = I_T \cdot N_T \cdot \sigma_B \quad (4.8)$$

$N_T$  represents the total number of matrix atoms per unit area and  $\sigma_B$  is the averaged matrix cross-section for all EELS-background contributions. In principle,  $N_T$  and  $\sigma_B$  values from element-containing sites inside the cell are unknown.

Among the Bio-standards available there is also the so called  $H^+$ -matrix material, in which all cationic counter ions are replaced by  $H^+$ . Such unloaded

## Chapter 4

material can be co-embedded with aldehyde-fixed single cells to compare the background-differences in the EEL-spectra.

### MATERIALS AND METHODS

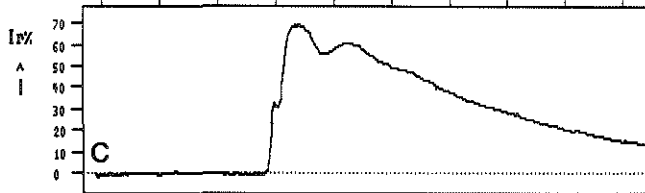
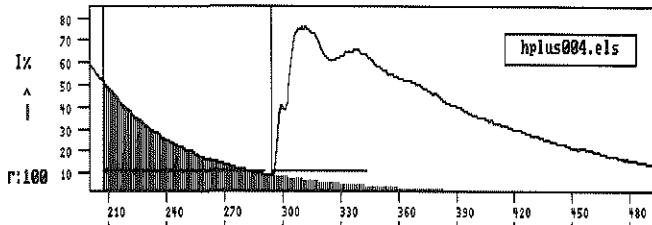
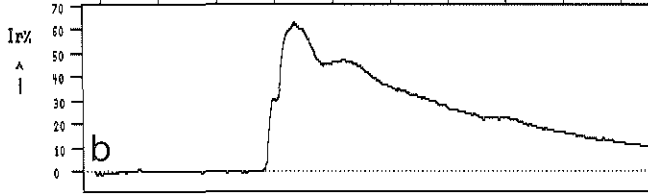
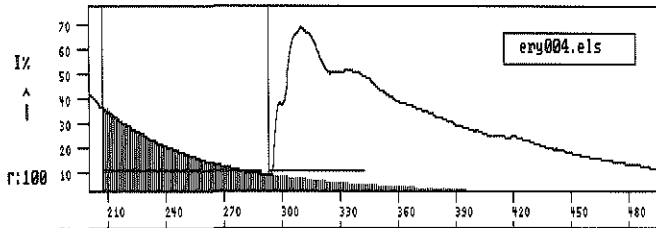
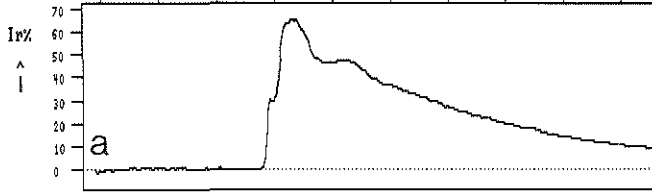
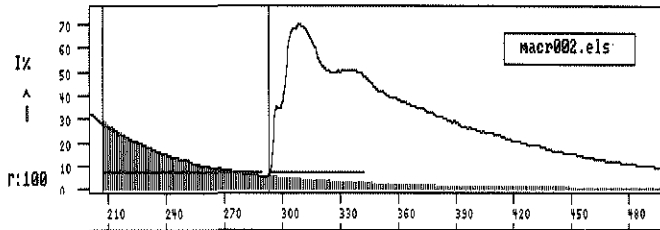
The Bio-standards used in our experiments were unloaded ( $H^+$ -Bio-standard), or loaded with counter iron ions (Fe-Bio-standard) or calcium (Ca-Bio-standard). Properties of these Bio-standards are given in Table 4.1.

Unstained ultrathin sections of the objects of interest with in their periphery the (un)loaded Bio-standards were examined with a Zeiss 902 electron microscope with a 90  $\mu m$  objective lens-diaphragm.

Bio-Standard	Composition (atomic fraction) ( $\times 10^{-3}$ )						M (kDa)	Density ( $g/cm^3$ )	Concentration of counterions (mean $\pm$ 1 SD)
	H	C	N	O	Fe	Ca			
$H^+$ -chelex	450	526	5	10	-	-	7.15	1.06	-
Fe-chelex	442	516	5	19	18	-	8.02	1.18	12.9 $\pm$ 1.0
Ca-chelex	444	519	5	19	-	13	7.57	1.07	6.13 $\pm$ 1.0

**Table 4.1.** Properties of the Bio-standards. Concentration of the counter ions were measured with neutron activation (NAA) and reveals the maximum obtainable loading of Bio-standards. M = molecular weight.

**Figure 4.1,** (Opposite page) Carbon-spectrum (above) with extrapolated background (below) from the cytoplasm of a peritoneal macrophage (a), from the matrix of a red blood cell (b), and from the matrix of a  $H^+$ -Bio-standard (c). ( $\Gamma = 85$  eV,  $\Delta = 25$  eV,  $\Phi = 90$   $\mu m$ ).



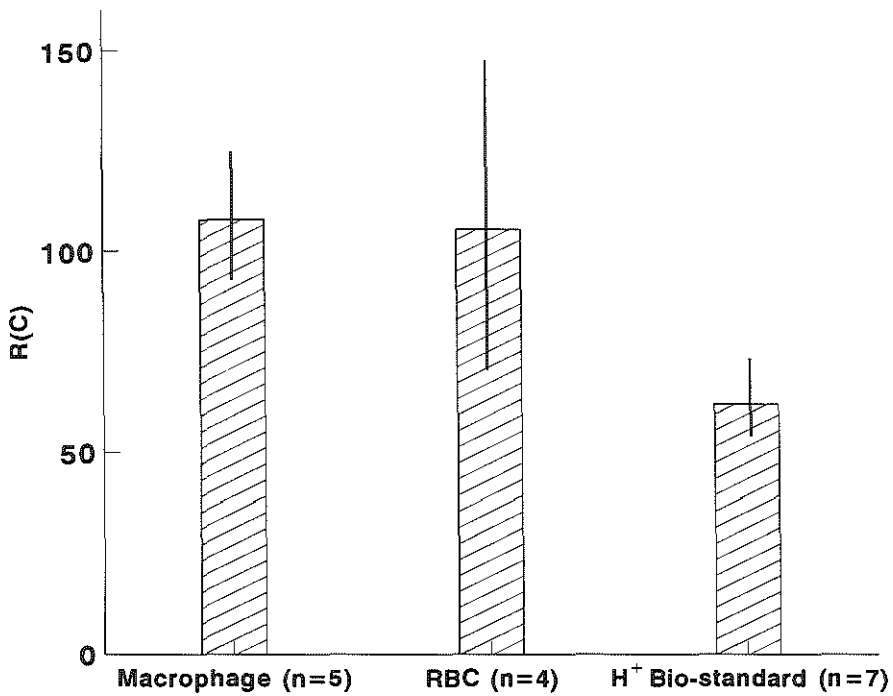


Figure 4.2, Mean relative carbon concentrations in macrophages, red blood cells (RBC) and H<sup>+</sup>-Bio-standards. The vertical bar represents the standard deviation.

## EXPERIMENTS

### *Comparing matrix composition of the Bio-standard with a "Cell"*

To determine the similarity of the Bio-standard with biological material, H<sup>+</sup>-Bio-standards were co-embedded with a glutaraldehyde-fixed cell population from a rat peritoneal cavity. To compare the matrices, spectra containing the carbon-edge were recorded in (a) macrophages (b) red blood cells and (c) H<sup>+</sup>-Bio-standards, all localized in one cross-section.

### *Iron measurements*

For a comparison of EEL-spectra obtained from two different concentrations of the same element, Fe-Bio-standards, with 12,9 wt% iron, were embedded in EPON together with pea-seed ferritin which contains a mean biochemically measured

concentration of 1850 atoms Fe/ferritin core. Spectra from the Fe-Bio-standards and the ferritin were recorded from an analyzed area of  $24 \cdot 10^3 \text{ nm}^2$  in the iron range with gain factor 100 in one ultrathin section under the same conditions.

In a second run, under the same conditions but with gain factor 1,  $I_T$ -spectra were recorded from the same locations as the iron-spectra.

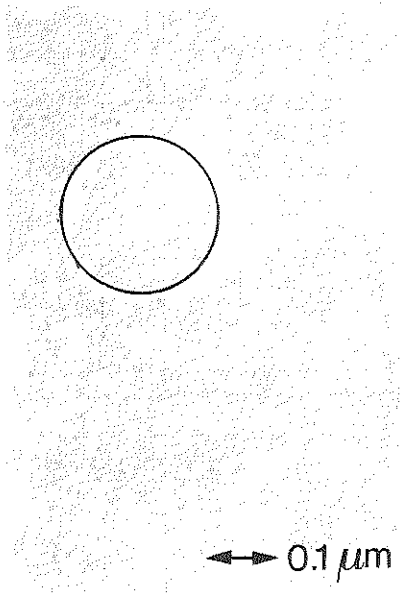


**Figure 4.3,**  
Electron micrograph of pea-seed ferritin cores. The ferritin cores are not homogeneously distributed. For EELS measurements, parts of the specimen were chosen where the cores were almost homogeneously distributed in the analyzed area. The circle represents the analyzed area ( $24 \cdot 10^3 \text{ nm}^2$ ).

### *Calcium measurements*

For this experiment, kidney tissue was used from rats in which calcium oxalate stones were induced by a diet of 0,8  $\text{v}/\text{v}\%$  ethylene glycol plus 1 wt% ammoniumchloride in their drinking water for eight days. The kidneys were perfusion fixed with 1,5 wt% glutaraldehyde in 0,1 M cacodylate/HCl buffer of pH 7,4 and  $1 \text{ mm}^3$  blocks of the cortex were embedded in EPON together with Ca-Bio-standards, with 6,13 wt% calcium.

Earlier investigation of kidney tissue postfixed with osmium tetroxide revealed not only crystal ghosts in the tubular lumens but also small primordial crystal ghosts (referred to as stone-primordia) in the tubular cells [De Bruijn *et al.*, 1990]. Therefore in only aldehyde fixed material from one section, three consecutive spectra from an analyzed area of  $24 \cdot 10^3 \text{ nm}^2$  were recorded in the calcium range in Ca-Bio-standards, stone-primordia and crystals.

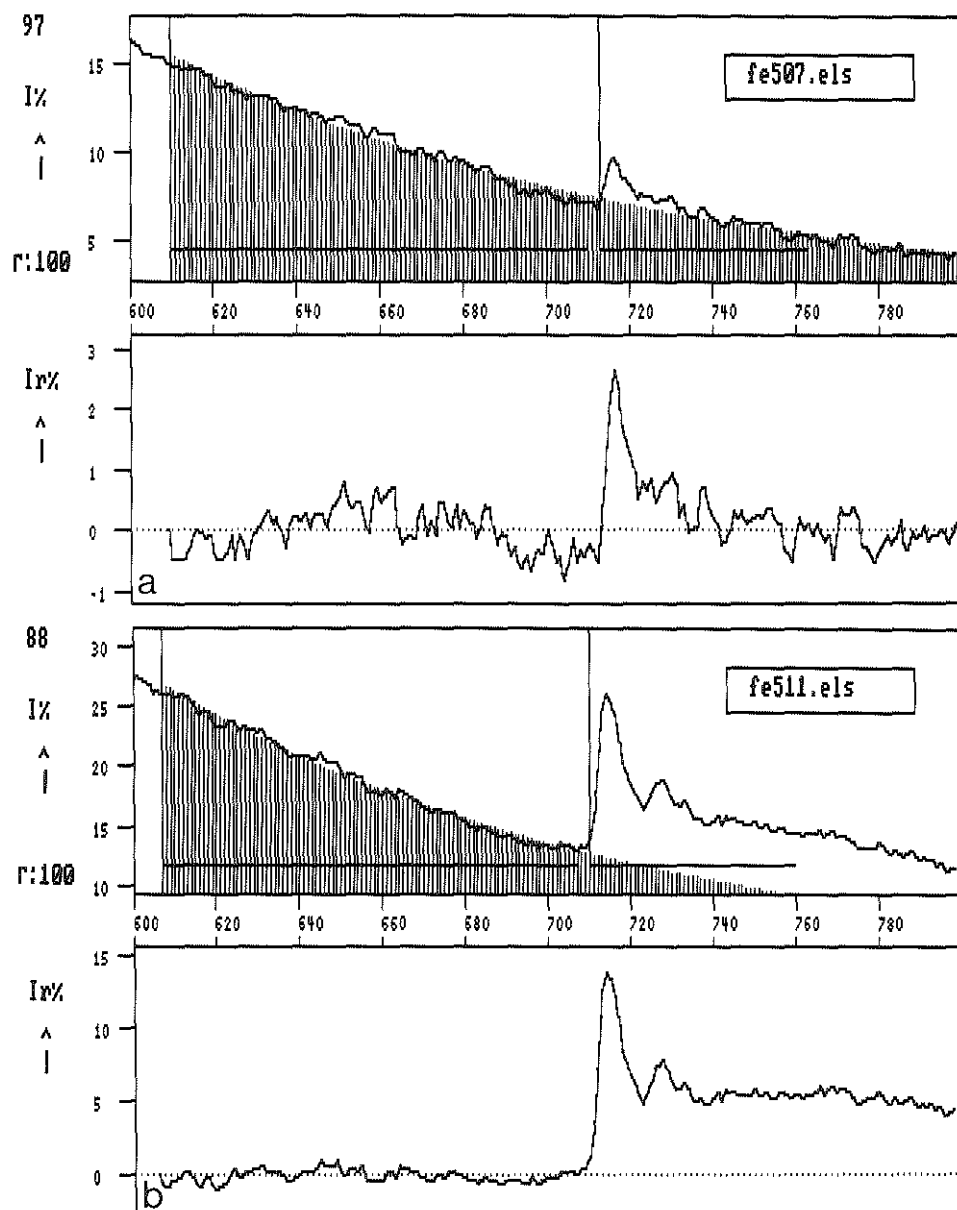
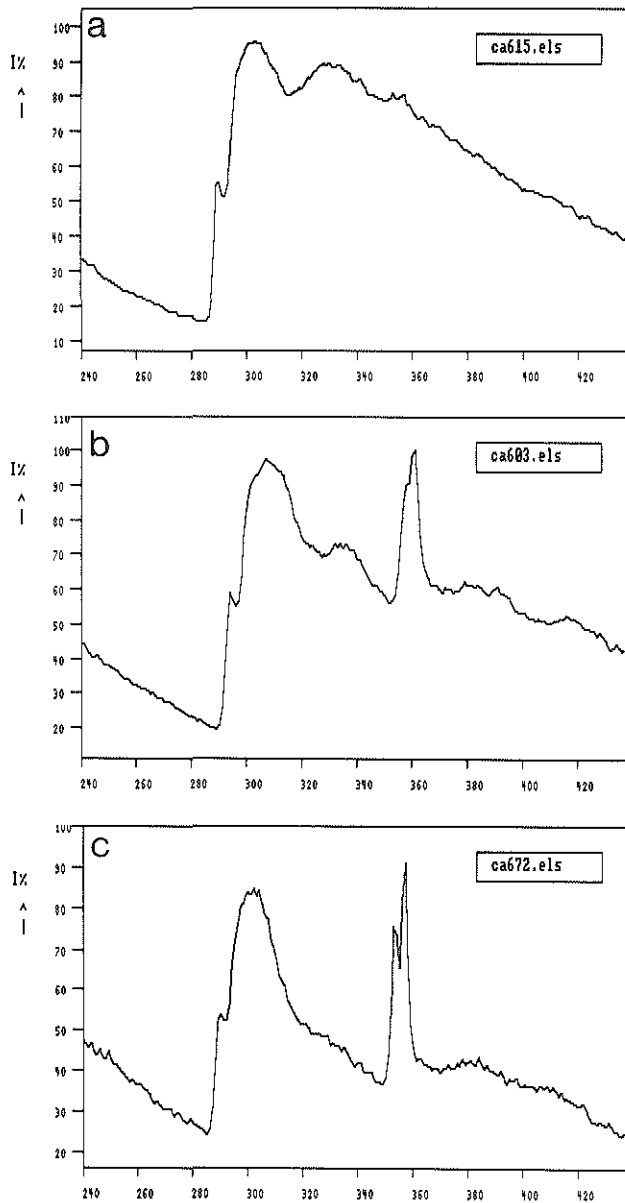
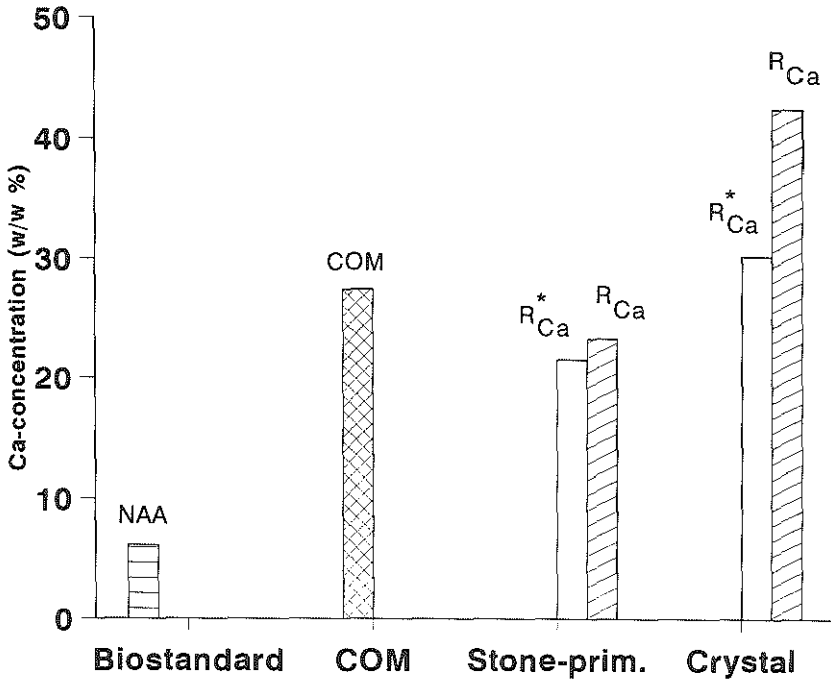


Figure 4.4, Iron spectrum with extrapolated background (above) and after background subtraction (below), from ferritin cores (a) and a Fe-Bio-standard (b), containing the Fe  $L_{2,3}$  edge, both recorded under the same conditions.



**Figure 4.5.** Spectra in the carbon (C) and calcium (Ca) range from a Ca-Bio-standard (a), a stone primordium (b) and a crystal (c), all recorded under the same conditions. The crystal has the highest relative calcium concentration, but the carbon edge outline differs from that of the Ca-Bio-standard and stone-primordium.



**Figure 4.6,** Calcium concentrations of stone primordia and crystals, compared to the 6.13 wt% calcium concentration (as measured with neutron activation (NAA)) of Ca-Bio-standards which is used in eq. 4.5 as the known, externally determined, concentration ( $N_{x,2}$ ) and compared to the 27.43 wt% calcium concentration of pure calcium oxalate monohydrate (COM). The influence of  $I_t$  on the calcium concentrations of the stone-primordium and the crystal is shown: calculations without  $I_t$  ( $R_{Ca}$ ) lead to higher concentrations than calculations with  $I_t$  ( $R_{Ca}^*$ ).

*Specimen thickness*

The section-thickness measurements using eq. 4.7 with a mean free pathlength value  $\lambda_{EPON} = 112.4$  nm [Colliex (1981); Malis *et al.* (1988)], leads to too low values for the actual specimen thickness ( $\leq 10$  nm). Therefore we had to question the correctness of this EPON free pathlength value [Sorber *et al.* (1991b)].  $I_t/I_0$  values were obtained from sections containing EPON embedded Bio-standards on a finder grid. The finder grid was then placed (sections down) in a drop of EPON (containing 1 wt% Ruthenium Red) on top of a flattened polished, pyramidal-shaped piece of polymerised EPON. The ribbon of sections was aligned over the

top of the pyramid such, that the first grid square measured before was over the top of the pyramid, leaving the remainder of the non-section bearing grid in the top of the pyramid. The selected grid square was subsequently sectioned perpendicularly, leaving the cross-section of the section plus the support film to be found in this second section. Due to the presence of the Ruthenium Red in the added EPON, the original section had a different contrast. Images were subsequently transferred to the IBAS 2000 where calibrated thickness measurements were performed for both the EPON and the film.

The obtained value for  $\lambda_{\text{EPON}}$  was used to examine the influence of the section thickness on the obtained relative concentration ( $R_x$ ).  $R_x$ -values of various ultrathin sectioned Bio-standards containing Fe, Co, and Ca, were compared and their values were plotted against estimates of the section thickness.

## RESULTS

### *Comparing matrix composition of the Bio-standard with a "Cell"*

One of the criteria of a good standard is that the organic matrix in the unloaded state has the same composition as the tissue matrices. In Fig. 4.1 spectra are shown in the carbon-range, measured in the cytoplasm of a macrophage (a), matrix of a red blood cell (b) and in the matrix from a  $\text{H}^+$ -Bio-standard (c). All spectra have a similar outline. In the spectrum from the red blood cell, a small nitrogen edge is seen at 402 eV. Relative concentration ( $R_C$ ) values of carbon are given in Fig. 4.2, revealing that macrophage and red blood cell contain about the same quantity of carbon whereas the  $\text{H}^+$ -Bio-standard material has less carbon.

### *Iron measurements*

Pea-seed ferritin molecules are composed of a hydrophilic mantle protein and an electron-dense iron core of approximately 6 nm diameter, which is clearly visible in the electron microscope (Fig. 4.3). The cores are not homogeneously distributed; for EELS measurements parts of the specimen were chosen where the cores were almost homogeneously distributed in the analyzed area.

Fig. 4.4 shows spectra in the Fe  $L_{2,3}$  range from ferritin cores (Fig. 4.4a-b) and a Fe-Bio-standard (Fig. 4.4c-d) (12,9 wt%). Because the conditions for both measurements were the same, it is obvious that the Fe-Bio-standard has a higher concentration of iron than the ferritin. The results of multiple measurements are presented in Table 4.2, where mean relative concentrations are shown.

## Chapter 4

Material	$R_{Fe}$	$R_{Fe}^*$
Pea-seed ferritin (n=5)	$0.103 \pm 0.02$	$0.79 \pm 0.29$
Fe- Bio-standard (n=6)	$0.331 \pm 0.05$	$6.04 \pm 1.64$

**Table 4.2,**  $R_{Fe}$  and  $R_{Fe}^*$ -values (calculated according to eqs. 1.2 and 1.3) with their standard deviations (SD) measured with the QSA program on Simplex-fitted curves (see chapter 3).

Using eq. 4.5,  $R_{Fe}^*$  of the measured ferritin iron concentration in the analyzed area is 1,87 wt%. Assuming that it is allowed to eliminate the differences between  $I_T$  of the ferritin and the Fe-Bio-standard and that there is a linear relation between the elemental concentration and  $R_x^*$ , the concentration of the ferritin in the analyzed area ( $R_{Fe}$ ) is 4,01 wt%. Differences in ferritin-core area and Fe-Bio-standard area are not taken into account.

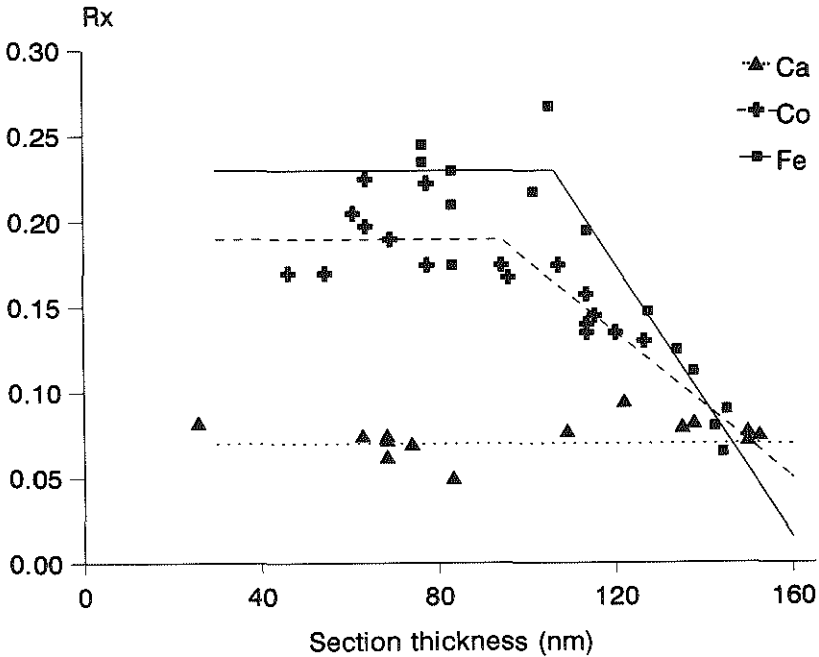
### Calcium measurements

Fig. 4.5 shows EEL-spectra from a Ca-Bio-standard (a), a stone-primordium (b) and a crystal (c), respectively. The spectra were measured between 220 and 420 eV, and contain the carbon K-edge in addition to the calcium  $L_{2,3}$ -edge. The crystal has the highest relative calcium concentration but this spectrum has a different outline, compared to that of the Ca-Bio-standard and stone-primordium.

In Fig. 4.6 the concentrations (in wt%) of the two measured biological objects are compared to the concentration of the Ca-Bio-Standard, which contains 6,13 wt% calcium, as measured with neutron activation. In order to determine the influence of differences in  $I_T$  on the concentration, both  $R_{Ca}$  as  $R_{Ca}^*$  are presented. Calculations without  $I_T$  ( $R_{Ca}$ ) lead to higher concentrations than calculations with  $I_T$  ( $R_{Ca}^*$ ).

$\ln(I_t/I_0)$	$t_1$	$t_2$	$t_2, \text{Film}$
0.217	$24.4 \pm 0.53$	$46.4 \pm 4.0$	$6.5 \pm 1.5$

**Table 4.3,** Comparison of the thickness in the original (1) section (eq. 4.7,  $\lambda_{EPON} = 112.4$  nm) with that of the re-embedded (2) section, leading to the conclusion that  $\lambda_{EPON}$  is 209.1 nm in this case.  $N=10$ .



**Figure 4.7,**  $R_x$ -values from various ultrathin sectioned Bio-standards related to the section thickness in nm. Calcium concentration measurements are insensitive to the section-thickness. The constancy of the mean  $R_x$ -values of iron and cobalt concentration measurements are influenced by the section thickness (thickness > 100 nm).

### *Specimen thickness*

Table 4.3 shows that the examined sections were in fact approximately twice as thick as the calculations obtained from the original sections with  $\lambda_{\text{EPON}} = 112.4$  nm. This led to the new value of 209.1 nm for the mean free pathlength of EPON.

The results obtained from Bio-standards with varying section-thicknesses are shown in Fig. 4.7. It is noticed that for "routine" ultrathin sections the  $R_x$  values are constant within certain limits. The  $R_x$ -values start to decrease beyond a certain section thickness, which value depends on the chemical element examined. There seems to be a relation between the  $Z$ -number of the element loaded and the deviation point from constancy.  $R_x$ -values from ultrathin sections of Ca Bio-standards were relatively insensitive for section-thickness increase, whereas those from iron Bio-standards and Cobalt Bio-standards were sensitive for this increase.

### DISCUSSION

Quantitative EELS analysis is becoming a well known technique, usually applied to elemental foils or sputtered elements on carbon films [Leapman *et al.*, 1984; Liu & Brown, 1987]. Elemental quantification in biological tissue still gives rise to problems due to the low concentration of elements, difficulties in estimating the mean cross-section, the electron mean free paths etc. Estimating biological concentrations requires a good standard. In this chapter Chelex<sup>100</sup>-based Bio-standards are proposed. These Bio-standards can be loaded with various counter ions, which are homogeneously distributed among and within the bead; with EELS analysis some inter- and intra-bead variations are measured [Sorber *et al.* (1991a, 1991b)].

In theory, the Bio-standards resemble biological tissue by the common presence of H, C, O and N in their matrix. EEL-spectra in the carbon range from unloaded Bio-standards and cells, indicate that the number of C-atoms in the analyzed area of the H<sup>+</sup>-Bio-standard is less than in the cells.

Bio-standards give us the opportunity to measure biological concentrations by EELS analysis, provided that several conditions and parameters (Eq. 4.7) are known:

- 1 Because the Bio-standards and tissue are localized in one ultrathin section, one could assume that  $I_T$  for both subjects is equal. The calcium measurements however prove that  $I_T$  from the Ca-Bio-standard differs from that in the tissue. Calculations for the concentrations without  $I_T$  ( $R_x$ ) lead to higher concentrations than calculations with  $I_T$  ( $R_x^*$ ) (Fig. 4.6). As the iron measurements show the same result (Table 4.2), elimination of  $I_T$  is not recommended.
- 2 Specific density ( $\rho$ ) depends on the atomic composition, which for biological material is often unknown. For the Bio-standards used here, we have calculated the atomic composition, from which weight and specific density were derived (Table 4.1). Measuring  $\rho$  by determining mean volume, number and weight of a sample of Bio-standards (as performed by De Bruijn (1981a, 1981b)) still has to be performed.
- 3 Specimen thickness ( $t$ ) has to be measured, assuming that the thickness of a cross-section of loaded Bio-standards and biological tissue is equal for all parts of the section. For the iron measurements we have recorded several  $I_T/I_0$  spectra of the embedding medium EPON (data not shown). Calculations

according to eq. 4.7, with an inelastic mean free path ( $\lambda_{in}$ ) of 112,4 nm for EPON at an accelerating voltage of 80 keV (as calculated from data from Colliex *et al.* (1984)), resulted in unacceptable  $t$  values. When specimen thickness was calculated according to Malis *et al.* (1988),  $t$  was found to be 20 nm. In subsequent experiments  $t$  was measured by re-embedding the specimen and variations in  $t$  between cross-sectioned beads and surrounding EPON were established. A new value was found for  $\lambda_{EPON}$ : 209.1 nm, which was confirmed by measurements of R. Door *et al.* (1991).

It was demonstrated in fig. 4.7 that there is a relation between  $R_x$  and the section thickness when the thickness exceeds the mean free pathlength for the element under investigation.

- 4 The last parameter necessary to determine the total number of atoms of an element is the size of the analyzed area. We have calculated this for each magnification according to Bihl *et al.* (1988). This value is not verified yet, nevertheless we have used this value to determine the total number of ferritin cores in the analyzed area by a counting procedure as outlined before for other ferritin [(Sorber *et al.* (1990b))].

Despite these uncertainties, we have followed eqs. 4.6 and 4.7 to determine the only "unknown" parameter: the section thickness of the Fe-Bio-standard/ferritin specimen using all calculated and measured values ( $\rho$ ,  $M$ ,  $I_K$ ,  $I_T$ ; see Table 4.1 and 4.2). This resulted, in order to obtain a concentration of 1850 Fe-atoms/ferritin core, in a specimen thickness of 74 nm when  $R_{Fe}^*$ -values were used and 31 nm when  $R_{Fe}$ -values are used, which are values of the same order of magnitude. Therefore we suggest that eq. 4.6, applied to measure Bio-standards and biological tissue with EELS, can be used and, instead of the number of atoms, also weight percentages can be calculated.

To determine the calcium concentrations in stone primordia and crystals, the proposed eq. 4.6 in wt% was used. This resulted in 21,56 ( $R_{Ca}^*$ ) or 23,31 ( $R_{Ca}$ ) wt% calcium for primordia and in 30,27 ( $R_{Ca}^*$ ) or 42,58 ( $R_{Ca}$ ) wt% calcium for crystals. It remains uncertain whether it is allowed to compare the ( $R_{Ca}^*$ )-values from the crystal with those from the Ca-Bio-standard, since a crystal has a different specific density (the specific density of calciumoxalate monohydrate is 2,2 g.cm<sup>-3</sup>) and it is not proved that there is a linear relation between  $R_{Ca}^*$  and the calcium-concentration. However, the calcium concentration in pure calciumoxalate monohydrate is 27,43 wt%, which is about the measured  $R_{Ca}^*$ -value (30.27).

When eq. 4.6 in wt% is used, one has to consider that the calculated

## Chapter 4

---

concentration is in wt% of the analyzed area. This is no problem if the object of interest covers the total analyzed area homogeneously, like the stone primordium, but it gives difficulties in the case of ferritin, where the cores are inhomogeneously distributed over a part of the analyzed area.

The introduction of Bio-standards with an externally determined, known concentration in the same ultrathin section as biological material, eliminates most of the risks and the need for precautions, mentioned by Trebbia (1988). Moreover, such ultrathin sectioned Bio-standards open the possibility for unbiased comparisons of results obtained by various instruments, as both ultrathin sections of the material and the Bio-standard material itself are exchangeable. In addition, this material may be used as a means to find the minimal detectable signal and hence, the minimal detectable mass, as we have shown before for X-ray microanalysis [De Bruijn (1981a, 1981b)].

The presence of the  $H^+$ -Bio-standard offers, in addition to its role as a material with a certain similarity to the cell matrix, the possibility to perform the subtraction procedure as proposed previously by Berger & Pennycook (1982) and recently by Shuman & Somlyo (1987) and Leapman & Swyt (1988) to improve the detection sensitivity with EELS.

Although some of the parameters to calculate the concentrations accurately need to be confirmed by direct measurements, the data presented here indicate that the loaded Bio-standards allow measurements of elemental concentrations in tissue by EELS analysis.

---

# **CHAPTER 5**

## **IMAGE ANALYSIS 1 MORPHOMETRICAL ANALYSIS WITH ELECTRON SPECTROSCOPIC IMAGING OF NON-ELEMENT RELATED IMAGES**

## CHAPTER 5

### IMAGE ANALYSIS 1

#### Morphometrical analysis with electron spectroscopic imaging of non-element related images.

This chapter has been published in *Ultramicroscopy* 32 (1990), p. 55-68.

*Quantitative energy-filtered image analysis in cytochemistry I. Morphometric analysis of contrast related images.*

Sorber C.W.J., De Jong A.A.W., Den Breejen N.J. and De Bruijn W.C. (1990)

#### SUMMARY

A combination of energy filtered electron microscopy (EFTEM) and an image analyzing system (IBAS 2000) is used for morphometric analyses of cells and (reaction) products. Image contrast is objectively established and segmentation is based upon intrinsic contrasts, in ultrathin sections.

Cross-sectioned platinum-stained erythrocytes are used as a model to determine optimal conditions for a reliable determination of contrast, area and perimeter. The influence of the following parameters is investigated:

- The objective-lens diaphragm diameter
- Three most frequently used contrast modes obtainable by electron spectroscopical imaging (ESI) in a Zeiss EM902 transmission electron microscope (Global, Zero loss ( $\Delta E = 0$  eV) and  $\Delta E = 250$  eV) (chapter 2).
- The number of image integrations (1x - 250x) acquired by real time video.

A thresholding procedure is proposed for objective segmentation of such contrast-related images and applied to measure the area fraction of nuclear chromatin and the diameter of nominal 1 nm colloidal gold particles.

---

## INTRODUCTION

When integrated cytochemical and morphometric image analysis is used to monitor the increase or decrease in product volume and elemental concentration in cells, attention has to be paid to:

- Morphometry, to determine area or area fractions, which are related to the requested volume fraction.
- The determination of elemental concentrations in the items of interest.
- The integration of morphometric information and concentration.

In this chapter only the morphometry will be discussed.

The recently introduced energy filtered electron transmission microscopy (EFTEM) [Adamson-Sharpe & Ottensmeyer (1984); Arsenault & Ottensmeyer (1983, 1984); Hezel *et al.* (1987); Reimer *et al.* (1991); Cleton *et al.* (1989)] certainly has not yet proved to overcome all mentioned limitations, but its electron spectroscopical imaging potentials [Hezel *et al.* (1986, 1987)] prompted us to investigate its application for a morphometric analysis using:

- ESI/TEM images.
- EELS/TEM elemental distribution images.
- ESI/TEM and EELS/TEM image integration.

This chapter will be restricted to ESI/TEM images. Items of interest in ESI images will be morphometrically analyzed based upon their intrinsic contrast (i.e. the difference in greyvalues). Morphometric analysis of such ESI images, after transfer to an image analyzer, will be performed in a type of post-acquisition digitization. Attention will be focused upon two questions:

- 1 How are (objectively determined) image contrasts from the two additional contrast modes (Zero loss, and  $\Delta E = 250$  eV) present in the Zeiss EM902 related to the "classical" global contrast mode present in conventional TEM instruments.
- 2 How can ESI contrast variations influence area and perimeter determinations.

The area and perimeter of platinum-stained erythrocyte cross-sections will be compared, following application of:

- The three aforementioned contrast modes
- Different objective-lens diaphragm diameters
- Different image-integration cycles for noise reduction.

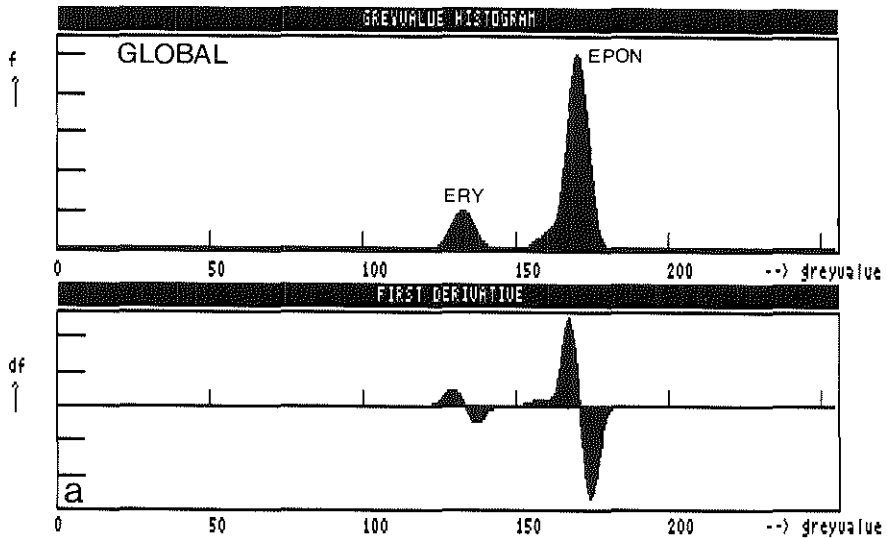
A procedure for objective image segmentation will be proposed to determine areas and area fractions. This procedure will be applied to measure the diameter of

## Chapter 5

nominal 1 nm colloidal gold particles, and chromatin/cell area fractions. In the next chapter, EELS/TEM element-distribution images will be morphometrically analyzed, and such images will be integrated with ESI/TEM images.

Image	$\Delta GV$ at aperture		
	30 $\mu\text{m}$	60 $\mu\text{m}$	90 $\mu\text{m}$
Global	38	-	31
Zero-loss	54	51	51
$\Delta E = 250 \text{ eV}$	54	95	101

**Table 5.1,** Contrast related to image modes and objective-lens diaphragm diameter. One single observation.



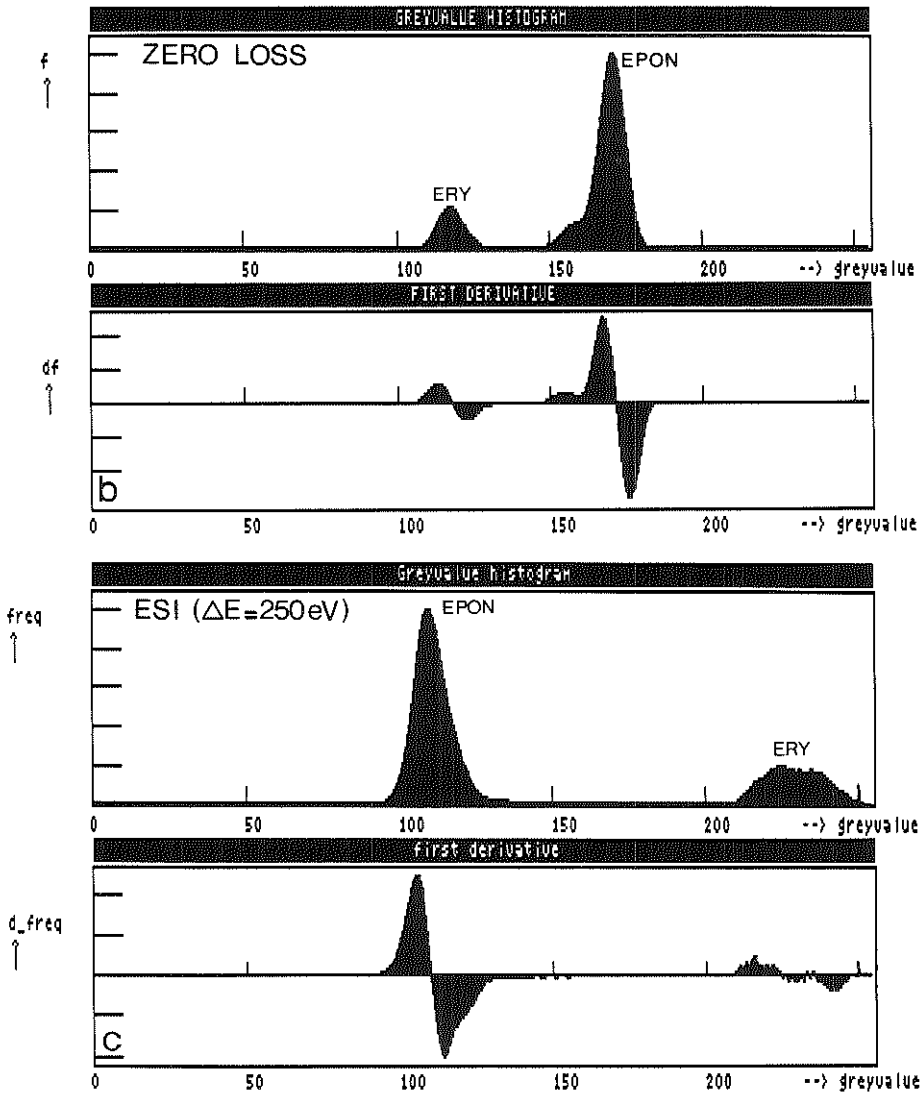


**Figure 5.1,** Greyvalue frequency histogram and its first derivative of an erythrocyte taken in the global image mode (a, opposite page), in the Zero-loss image mode (b) and in the  $\Delta E = 250$  eV ESI mode (c). All images are recorded with a  $90 \mu\text{m}$  objective diaphragm. Note the increase in contrast, defined as the distance between peak maxima ( $\Delta\text{GV}$ ). In the ESI image ( $\Delta E = 250$  eV) the increased contrast between erythrocyte and EPON is reversed.

### RESULTS

#### *Image contrast*

The influence of three different objective-lens diaphragms diameters (30, 60 and 90  $\mu\text{m}$ , giving apertures of 5, 10, 20 mrad), and of three imaging modes (global, Zero loss, ESI at  $\Delta E = 250$  eV) on the image contrast is first objectively established.

As a model, images acquired from the same, platinum-containing, cross-sectioned erythrocyte, surrounded by EPON, are used. One single image of each condition is acquired and analyzed. From this set of 9 images, the greyvalue frequency histograms and their first derivatives are acquired. Three such histograms are shown in Fig. 5.1. The corresponding images are acquired with a 90  $\mu\text{m}$  objective-lens diaphragm and 100 images are integrated. The image conditions are: global (Fig. 5.1a), Zero loss (Fig. 5.1b) and  $\Delta E = 250$  eV (Fig. 5.1c). The greyvalues vary from 0 (black) to 255 (white). Two crossover types can be noticed in the first derivatives:

- a from positive to negative, indicating the top of the peaks and
- b from negative to positive, indicating the separation between the two distributions.

When we use the first set of crossovers •a, the contrast between two populations can be defined as the distance between two peaks on the greyvalue scale ( $\Delta\text{GV}$ ). Changes in contrast can now objectively be determined. Contrast changes as measured in the various imaging modes and with various objective-apertures at 80 keV are shown in Table 5.1.

From Table 5.1 we may conclude that:

- the global image contrast increases with diaphragm diameter reduction;
- the relatively higher Zero-loss image contrast is less influenced by diaphragm-diameter variation;
- in the  $\Delta E = 250$  eV-images, the (inverted) contrast increases with larger diaphragm diameters.

When the experiments are repeated ( $n=5$ ) with the same erythrocyte under the same imaging conditions, the instrumental contrast variations, expressed as a coefficient of variance ( $C.V. = \text{Standard Deviation}/\text{mean value} \times 100\%$ ), appeared to be smaller than or equal to 1% (Table 5.2).

Image	Integration	$\Delta$ GV	CV
Zero-loss	100x (n=5)	59.6	1.0 %

**Table 5.2,** Contrast as measured by repeated observations of the same cell with a 30  $\mu$ m aperture (at 80 keV).

The influence of the variation in the number of the integrated images (1x as compared to 200x) upon the contrast is shown in Fig. 5.2-5.3. In Fig. 5.2, greyvalue tracings are shown along a line crossing the erythrocyte. In these images the variation in greyvalues between a minimum and maximum are indicated for both the EPON surroundings and the erythrocyte.

In Fig. 5.3, greyvalue histograms of the total images are given. It can be noticed that the contrast is only slightly influenced by this integration procedure.

In Table 5.3, the greyvalues from single images as compared to the mean of the values of 5x, 25x, 50x 100x and 250x are shown. The influence of the various objective-lens apertures upon the contrast of global images at 50 and 80 keV acceleration voltage is investigated. It is noticed that:

- The mean contrast is slightly decreased when images are integrated.
- The reproducibility is slightly changed by multiple image integrations, (C.V. = 1.5% as compared to <1%).
- The contrast is increased at lower acceleration voltage.
- An increase in diaphragm-diameter causes a decrease in  $\Delta$ GV.

Voltage (keV)	Integration	30 $\mu$ m		60 $\mu$ m		90 $\mu$ m	
		$\Delta$ GV	CV	$\Delta$ GV	CV	$\Delta$ GV	CV
80	5x - 250x	35.3	1.5 %	29.8	1.3 %	26.2	1.5 %
50	5x - 250x	49.8	0.9 %	46.8	0.9 %	47.8	0.9 %
50	1x	51.0	-	47.0	-	48.0	-

**Table 5.3,** Contrast related to the microscope acceleration voltage, integration frequency and diaphragm diameter (global imaging).

## Chapter 5

Image	30 $\mu\text{m}$		60 $\mu\text{m}$		90 $\mu\text{m}$	
	$\Delta\text{GV}$	CV	$\Delta\text{GV}$	CV	$\Delta\text{GV}$	CV
Global	50	-	43	-	40	-
Zero-loss	63.8	< 1 %	60.8	< 1 %	64.6	< 1 %
$\Delta\text{E} = 250 \text{ eV}$	116.0	1.7 %	128.0	< 1 %	132.5	6.9 %

**Table 5.4,** Contrast as measured by multiple observations of the same erythrocyte in the Zero-loss ( $\Delta\text{E} = 0 \text{ eV}$ ) or ESI mode ( $\Delta\text{E} = 250 \text{ eV}$ ) as compared to one single observation under global image conditions.

In Table 5.4, for a different erythrocyte cross-section, the same relation is shown for the Zero-loss and  $\Delta\text{E} = 250 \text{ eV}$  images (100 x integrated and frequent ( $n=5$ ) observations) as compared to a single global image observation:

- contrast is uninfluenced by multiple Zero-loss observations;
- contrast is highly variable by multiple  $\Delta\text{E} = 250 \text{ eV}$  observations;
- the same trends, as shown in Table 5.1, for single observations are present.

### Area

When the crossovers from negative to positive are used to separate the two distributions, the areas occupied by each population can be defined as the number of pixels in each distribution/total pixel number, x 100. (Area in pixel%).

Areas of the cross-section from one single erythrocyte (shown before in Table 5.1) are compared by changing either the objective aperture or the imaging mode. Table 5.5 shows the influences on area measurements:

- the calculated erythrocyte area is largest (16.8 pixel %) when measured with the smallest (30  $\mu\text{m}$ ) diaphragm and smallest (16.1 pixel%) when using the 60  $\mu\text{m}$  diaphragm. At this magnification 1 pixel % = 232.1  $\text{nm}^2$ ;
- when the smallest diaphragm is installed, the measured area is independent of the imaging mode;
- with the largest diaphragm installed, the measured area does depend on the imaging mode.

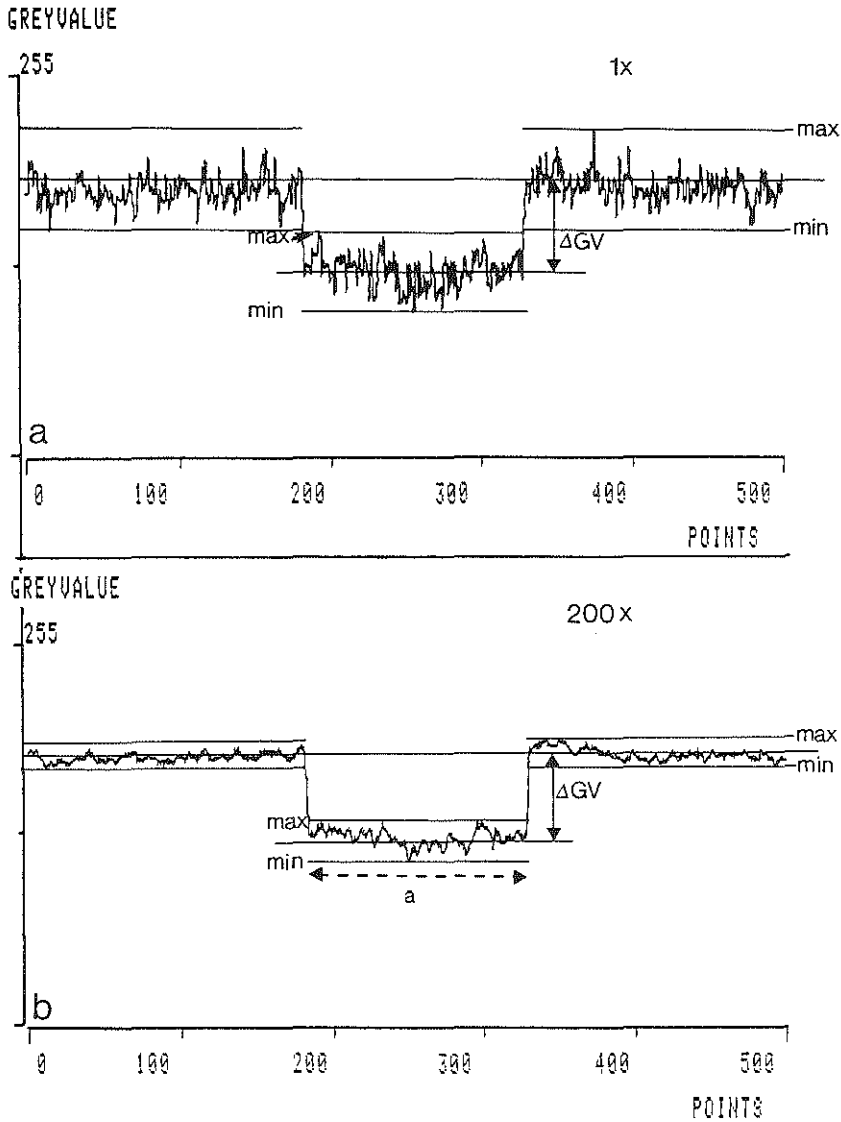


**Figure 5.2.** Contrast tracing through a platinum containing erythrocyte used for the contrast experiments shown in Fig. 5.1. Greyvalue fluctuations are indicated between minimal and maximal values for both the erythrocyte and the EPON surroundings.  $\Delta GV$  = distance between the two greyvalue populations,  $a$  is the cross-section through the erythrocyte. Imaging conditions: Zero-loss image ( $\Delta E = 0$  eV),  $90 \mu\text{m}$  objective diaphragm (1x (a) and 200x (b) integration).

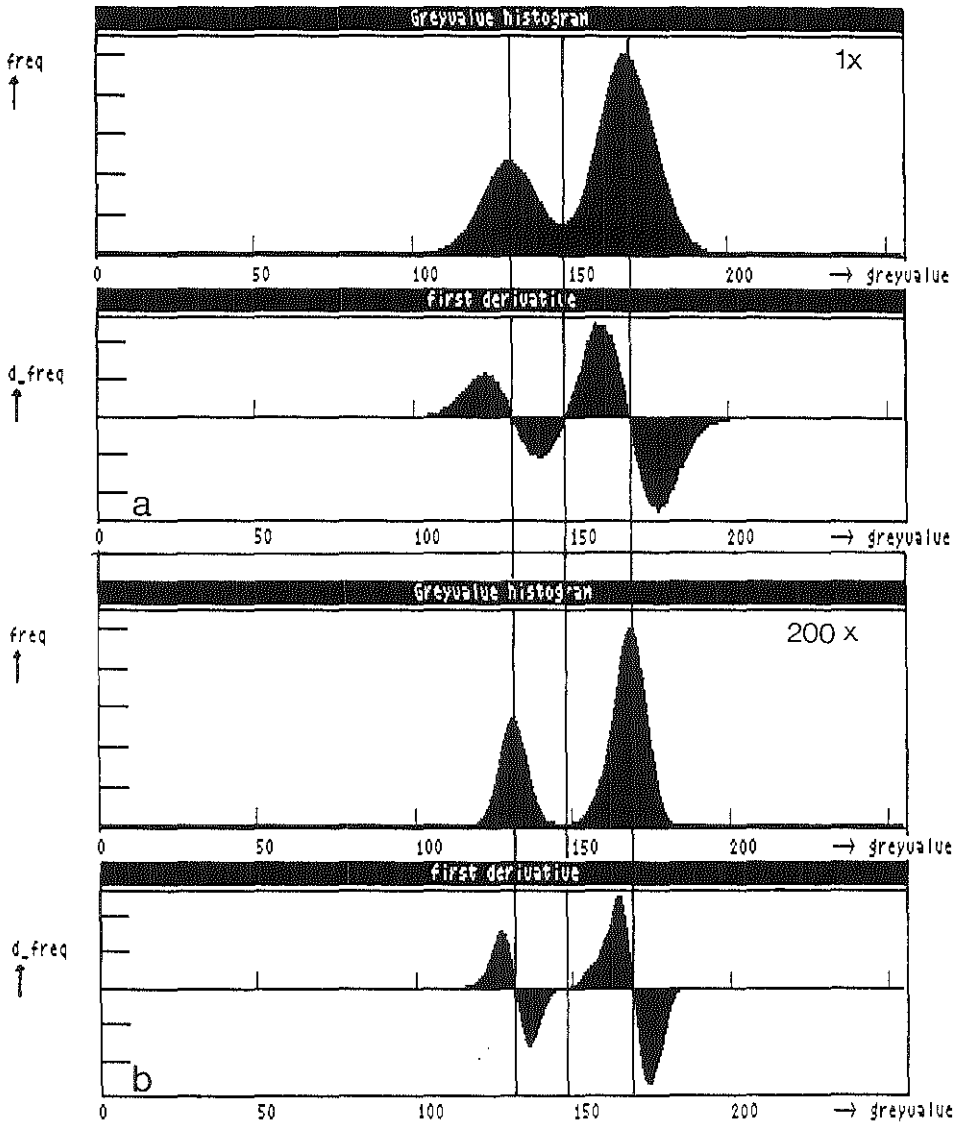


**Figure 5.3,** Greyvalue frequency histogram and its first derivative from the same erythrocyte as shown in Fig. 5.2. Note the virtual equality of the contrast between Fig. 5.3a (1x) and Fig. 5.3b (200x), and the improved separation between the erythrocyte and EPON populations upon integration.

Image	Area erythrocyte (pixel %)		
	30 $\mu\text{m}$	60 $\mu\text{m}$	90 $\mu\text{m}$
Global	16.8	-	16.7
Zero-loss	16.8	16.2	16.5
$\Delta E = 250 \text{ eV}$	16.8	16.1	16.4

**Table 5.5,** Area as measured in the three image modes and with various objective diaphragm diameters. One single observation.

The influence of integration frequency and objective aperture on the erythrocyte area (measured in global images) is shown in Table 5.6:

- the area is significantly increased when images are integrated;
- the differences in area induced by the diaphragm diameter variations are, at least for these global images, not significant. (1 pixel % =  $120.2 \text{ nm}^2$ ). In Figs. 5.2-3, it can be observed that the number of integrations improves the separation of the two populations.

In Table 5.7, the influence of the same parameters on the area measured in the Zero-loss and  $\Delta E = 250 \text{ eV}$  images of the same erythrocyte is shown:

- Differences in area, among the multiple measurements ( $n=5$ ) are small ( $\text{CV} < 1\%$ );
- Differences in area between the various objective apertures for the Zero-loss images are small, though significant;

Image	Integration	30 $\mu\text{m}$		60 $\mu\text{m}$		90 $\mu\text{m}$	
		Area	CV	Area	CV	Area	CV
Global	5x - 250x	37.12	1.1 %	38.74	< 1 %	37.54	< 1 %
Global	1x	36.40	-	34.30	-	31.90	-

**Table 5.6,** Area related to image integration frequency in global images. The acquired area differences are not significant, among the various diaphragms using multiple integrations ( $p > 0.05$ ).

## Chapter 5

Image	Integration	30 $\mu\text{m}$		60 $\mu\text{m}$		90 $\mu\text{m}$	
		Area	CV	Area	CV	Area	CV
Global	100x	28.20	-	27.90	-	-	-
Zero-loss	100x	28.32	< 1 %	28.04	< 1 %	28.42	< 1 %
$\Delta E = 250 \text{ eV}$	100x	25.35	< 1 %	24.80	< 1 %	28.00	< 1 %

$\Delta E$	Aperture ( $\mu\text{m}$ )	Significance p					
		Zero-loss			$\Delta E = 250 \text{ eV}$		
		30 $\mu\text{m}$	60 $\mu\text{m}$	90 $\mu\text{m}$	30 $\mu\text{m}$	60 $\mu\text{m}$	90 $\mu\text{m}$
0	30	-	<0.05	>0.05	<0.05	-	-
0	60	<0.05	-	<0.05	-	<0.05	-
0	90	>0.05	<0.05	-	-	-	<0.05
250	30	<0.05	-	-	-	<0.05	<0.05
250	60	-	<0.05	-	<0.05	-	<0.05
250	90	-	-	<0.05	<0.05	<0.05	-

**Table 5.7,** Area determined from multiple ( $n=5$ ) observations of the same cell under Zero-loss and ESI conditions compared to a single global mode observation. The majority of the areas acquired are significantly different ( $p < 0.05$ ) both among the image modes and the diaphragms selected;  $p$  is the significance between area and diaphragm diameter.

- Differences in area between the various apertures for the  $\Delta E = 250 \text{ eV}$  images are significant.
- Differences in area measured with Zero-loss or  $\Delta E = 250 \text{ eV}$ , are significant for each aperture (except for the diaphragms of 30  $\mu\text{m}$  versus 90  $\mu\text{m}$ ).
- The single measurement ( $n=1$ ) of the global image shows the same trends as in Table 5.5. (1 pix% = 120.2 nm<sup>2</sup>).

### Perimeter

Variations of the erythrocyte's relative perimeter as a function of the same parameters are given in Table 5.8 for global images:

- The perimeter is highly influenced by the differences in integration;
- The perimeter decreases with increasing integrations and stabilizes after about 50 x (C.V. = 2 - 4%);

Image	Integration	30 $\mu\text{m}$		60 $\mu\text{m}$		90 $\mu\text{m}$	
		Perim.	CV	Perim.	CV	Perim.	CV
Global	50x - 250x	1390	1.8 %	1515	3.5 %	1467	2.2 %
Global	1x	2392	-	3125	-	2788	-

**Table 5.8,** Perimeter related to integration frequency and diaphragm diameter for the global image mode.

- The perimeter differences for different apertures and the image mode are significant (except for the diaphragms of 60  $\mu\text{m}$  versus 90  $\mu\text{m}$ ).

In conclusion:

- A 100x image integration seems to be a fair compromise between speed and noise reduction for both area and perimeter.
- Different objective apertures induce significant area differences.
- Different image modes (Zero-loss or  $\Delta E = 250$  eV) induce small though significant variations in the areas measured.

At increased  $\Delta E$  values, the reduction in beam intensity favours the choice of the 90  $\mu\text{m}$  objective-lens diaphragm. As a consequence, a 90  $\mu\text{m}$  objective-lens diaphragm has been used in two experiments performed to measure items of interest based upon their intrinsic contrast and after application of the proposed objective segmentation procedure:

In Table 5.9, results are collected from measurements of 1 nm colloidal gold particles. From the same microscope fields, Zero-loss images are acquired at two different magnifications to monitor the accuracy of the measurements. For both magnifications the mean diameter, the number of pixels/particle and the shape factor is calculated.

M	$D_{\text{circle}}$ (nm)	$\sigma$	n	$N_{\text{pix/part}}$	Shape-factor
225,000x	1.67	0.26	48	25	0.57
400,000x	1.32	0.35	25	50	0.38

**Table 5.9,** Colloidal gold particle diameter (nominal 1 nm) measured at two magnifications.

In Fig. 5.4, and colour plate Fig. 5.5a-b, images and a histogram are shown from an experiment to obtain the area fraction of the chromatin in an unstained nucleated mouse peritoneal macrophage.

The greyvalue frequency histogram of the  $\Delta E = 250$  eV-image shown in Fig. 5.4a is given in Fig 5.4b. In this greyvalue histogram three populations are present:

- 1 EPON.
- 2 Cytoplasm.
- 3 Nuclear chromatin.

The nuclear-chromatin population has the highest greyvalue. To separate these three populations, crossovers (type b) between three distributions are found by the first derivative, obtained from the histogram (Fig. 5.4c). The images are made binary by two thresholds positioned at the two selected crossovers, thus segmenting the image in cell/EPON (Fig. 5.5a) and nuclear chromatin/cytoplasm (Fig. 5.5b). Binary images are used to calculate relative cell and nuclear chromatin areas, and hence the area fraction of the nuclear chromatin (0.17). Alternatively, when a dilatation step is used "to fill-in" the holes in the nucleus, the area fraction nucleus/cell is obtained (0.22). Prior to measuring, we used an erosion step to remove parts of the neighbouring cells in the corners.

## DISCUSSION

Segmentation of electron microscopic images is intimately related to the image contrast. When intrinsic cell organelles are to be separated and staining has to be avoided, instrumental contrast manipulation is the first choice for optimal results. The answer to this problem in dedicated-STEM instruments was ratio contrast [Shuman *et al.* (1986)]. Zero-loss and ESI-contrast has become an alternative in TEM instruments [Hezel *et al.* (1988); De Bruijn *et al.* (1989); Peachy *et al.* (1988); Trinick & Berriman (1987)]. The announced contrast improvements [Hezel *et al.* (1988)] are confirmed in this chapter by objective measurements. The influence of the image mode, the integration frequency and objective aperture upon the two morphometric parameters area and perimeter is considered.

However, the nature of the intrinsic contrast is enclosed in the chemical composition of cellular material visualized. The endogenous contrast between the nuclear chromatin and the cytoplasm as shown at  $\Delta E = 250$  eV might be induced

by several possible factors:

- The spectral position of the phosphorus  $L_{1,2}$  edge below the carbon K edge at  $\Delta E = 286$  eV.
- The chromatin versus cytoplasmic phosphorus concentration.
- The section thickness.

Moreover, Carlemalm *et al.* (1984), indicated that the difference in hydrogen concentration might play a dominant role. Section thickness has not successfully been determined in our material. Methods to determine objectively layer/section thickness have become available [Berriman & Leonard (196); Leapman *et al.* (1984a); Liu & Brown (1987); Malis *et al.* (1988)]. However, these methods need adaptation for extremely thin, unfilmed sections of biological material due to the virtual absence of a low loss edge.

Once an averaged, shading-corrected ESI image is acquired, objective threshold determination is the next step. Conversion of the image into greyvalue histograms is generally advocated [De Bruijn & Van Miert (1988); Russ & Russ (1984, 1987); Gundersen (1986)]. The first derivative-based method we used is reproducible and fast, but sometimes requires a (median or moving boxcar filter) smoothing step to eliminate additional unwanted minor crossovers [De Bruijn & Van Miert (1988)]. Other methods proposed [Malis & Cheng (1988); Russ & Russ (1984, 1987); Gundersen (1986); Johannsen & Bille (1982); Verbeek *et al.* (1988); Meyer (1981)] which may give more precise results, still have to be investigated in the future.

Once the images are segmented, relative areas (pixel %) or area ratios can directly be measured, or relative areas can be converted to real areas. Limitations encountered with our procedure are:

- When greyvalues of items of interest are present in low numbers and hence a small peak is present, it is hard to detect the crossovers when the peaks overlap in the greyvalue histogram. A solution for this problem can be a larger initial magnification or a post-magnification step in the IBAS, or a segmentation procedure based upon the "background" population alone (mean + (3-5) x standard deviation).
- When the contrast between the item of interest and its surroundings is too small, two peaks will overlap, which makes it impossible to separate populations completely.
- When images are noisy, pixels which do not belong to the item of interest are segmented as well.

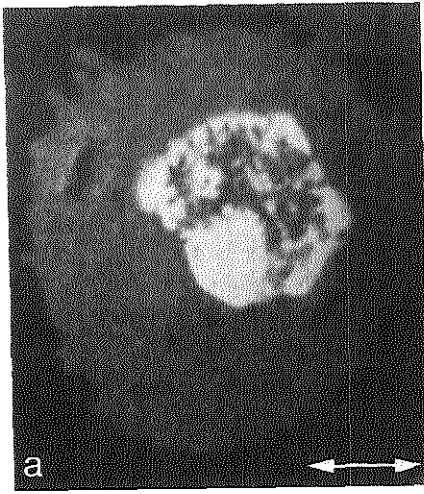
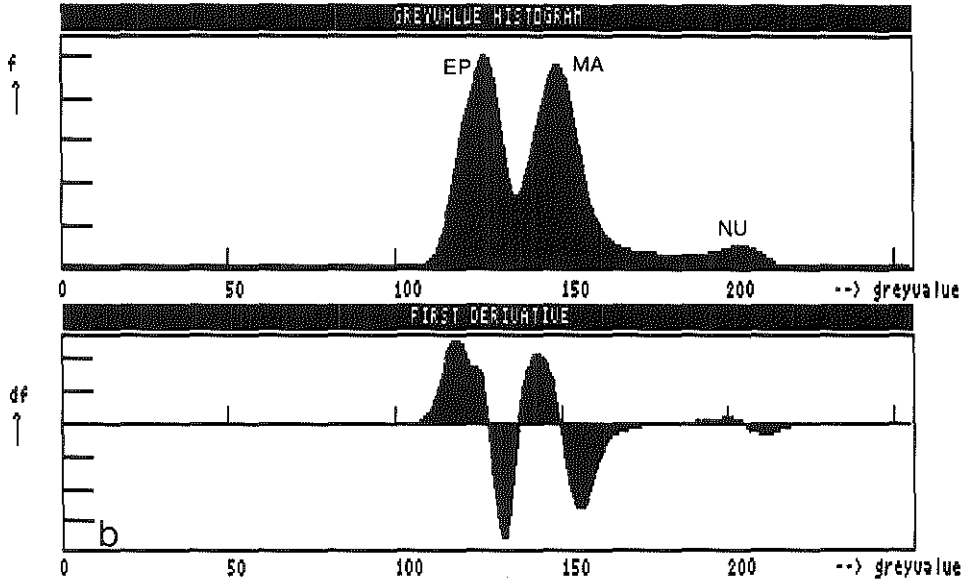


**Figure 5.4,**  
 (a) Unstained ultrathin sectioned mouse peritoneal macrophage. Imaging condition  $\Delta E = 250$  eV and  $90 \mu\text{m}$  objective diaphragm, showing the intrinsic contrast in the bright nuclear chromatin. Bar =  $1 \mu\text{m}$ . (b) Greyvalue frequency histogram and first derivative of the same macrophage, showing three populations, EPON/ cytoplasm/ nuclear chromatin. EP = EPON, MA = Cytoplasm, NU = nucleus. The binary images are shown in the colour plate Fig. 5.5a-b.



There might also be a difference in the degree of confidence in the delineation of the items of interest present in the final image [Trebbia (1989)]. When in our first derivative-based method, the peaks are completely separated (Fig. 5.1) the

degree of confidence of segmentation is unimpaired. Confidence is challenged when two curves overlap and the crossover indicates the lowest value in between the two (Fig. 5.4, cytoplasm/EPON).

Another aspect is the degree of accuracy of the acquired area's, induced by (the choice of) the number of pixels per particle for the area determination of very small particles, as demonstrated by our measurements of the colloidal-gold particles shown in Table 5.9. Theoretical aspects of this kind of inaccuracies are well known [Young (1988)].

When staining is permitted (performed) the choice of stain is important. It has to be realized that most of the staining strategies in the past intended to increase elastic scatter. Recently Reimer *et al.* [Reimer *et al.* (1988); Reimer (1991); Reimer & Ross-Messemer (1990a, 1990b)] have calculated the gain in contrast between global and Zero-loss images using, among other examples, 100% evaporated platinum films on pure carbon films. In this paper we used platinum containing erythrocytes for similar contrast experiments. From such erythrocytes, from the same EPON block as we used here, we have calculated before with EPMA a platinum weight percentage of 46% [De Bruijn *et al.* (1979)].

Once an optimal contrast condition is obtained, noise reduction and shading correction are the next steps to consider. Although these steps are vital for a good final result, we just followed the (Zeiss/IBAS/Kontron) instructions as described and selected initially an averaging of 100 images. The noise/contrast aspect related to segmentation is outlined in Fig. 5.2, by a greyvalue cross-section through the erythrocyte used for the contrast experiments after 1x and 200 x averaging. The horizontal lines indicate the mean (residual) greyvalue in each population (EPON/erythrocyte). The residual texture (noise or knife marks) in each population is indicated by the original tracing. The width of the erythrocyte (a) as determined from this cross-section depends on whether the highest (max) or the lowest points (min) of the noise curves are interconnected. Various solutions to this problem have been proposed, like linear and non-linear Laplace filtering [Russ & Russ (1984); Gundersen (1986)].

Recently, Verbeek *et al.* (1988) proposed the use of a min/max filter, which located (a) halfway between ( $\Delta GV$ ) and midway between the (min) and (max) noise curves at that height. Our decisions for segmentation in noise-reduced images are in principle similar (halfway between the two peaks). It has to be realised that our choice to use erythrocyte cross-sections as an object for segmentation reduced the risk of loosing high resolution information due to image integration. When high

## Chapter 5

---

resolution aspects in the images are to be expected and have to be preserved other strategies have to be chosen [Trebbia (1989)].

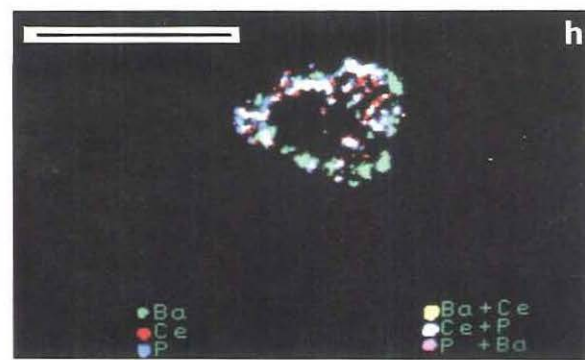
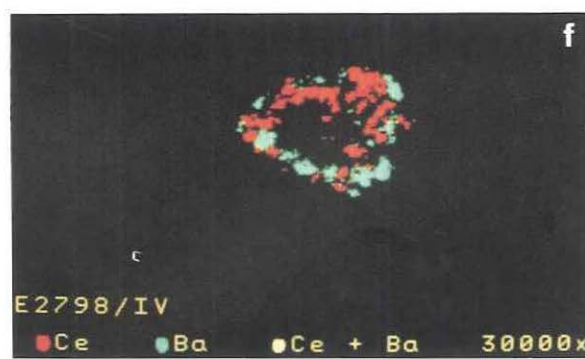
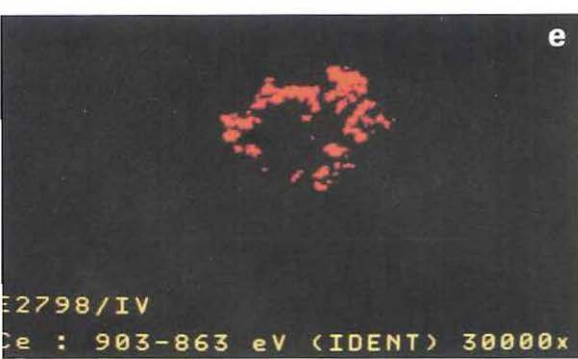
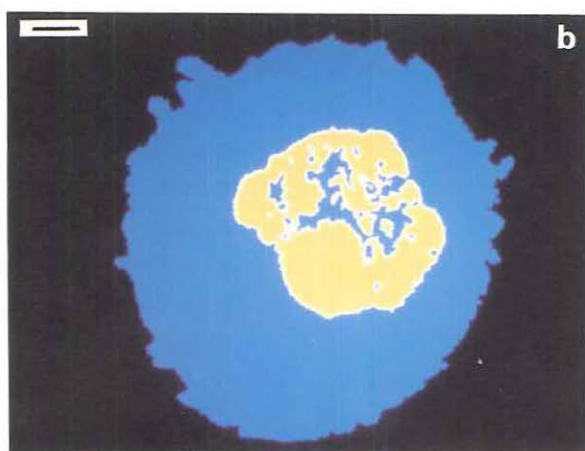
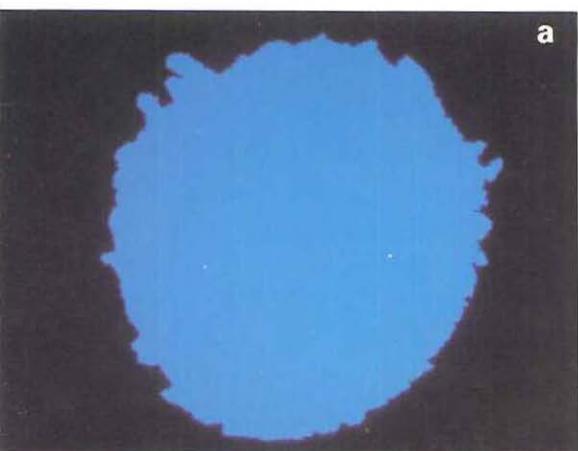
The use of a 90  $\mu\text{m}$  objective-lens diaphragm during ESI analysis is chosen for brightness reasons, but includes the risk of significantly different area values to be obtained. This brings us to the semantic question: which value will represent the true value. Future experiments on specimens with externally verifiable values might bring the answer to the question about the degree of systemic error which is present in our (mainly global) observations.

**Figure 5.5,** Binary image of a mouse peritoneal macrophage (a) ( $\Delta\text{GV} > 135$ ) and of the nuclear chromatin ( $\Delta\text{GV} > 175$ ) and the cytoplasm ( $135 < \Delta\text{GV} < 175$ ) of the same cell (b), objectively segmented according to the greyvalue histogram in Fig. 5.4b-c. Pseudo-colour image. Bar = 1  $\mu\text{m}$ .

**Figures. 5.5c-h** Pseudo-colour images described in chapter 6.

(c) Phosphorus semi net-intensity element-distribution image of a lysosome, in which three lysosomal enzymes will be differentiated; (d) Superposition of the cerium and phosphorus leading to a new white colour at the places where the two images coincide; (e) Cerium semi net-intensity element-distribution image of the same lysosome; (f) Superposition of cerium and barium net-intensity images showing the virtual absence of the new (yellow) colour at the places of coincidence; (g) Barium semi net-intensity element-distribution image of the same lysosome; (h) Superposition of three net-intensity element-distribution images, showing the slight coincidence of barium and phosphorus as a new colour at a few places. Bar valid for Figs. 5.5c-5.5h = 550 nm.

# Image analysis 1



## Chapter 5

---

In conclusion the following statements can be made:

### I. Image contrast analysis.

- The first derivative of the greyvalue histogram of ESI images allows an objective determination of the image-contrast values present in 46 wt% platinum stained erythrocytes and 100% colloidal-gold particles.
- The contrast improvement of the two EFTEM imaging modes used in the Zeiss EM902 (Zero-loss and  $\Delta E = 250$  eV) are objectively established.

### II. Morphometric analysis.

- A method, based upon the first derivative of the image greyvalue histogram is also used for objective segmentation. By that procedure, cell components can be segmented by their intrinsic contrast.
- The success of objective segmentation is limited by small intrinsic contrast between the item of interest and its surroundings, the low occurrence of the item of interest and the high noise in the original image.
- It is possible to get area fractions from ESI-images from unstained, only aldehyde-fixed cells by energy-filtering with  $\Delta E = 250$  eV electrons when conditions •1 and •2 are fulfilled.
- Significantly different area and perimeter values are obtained with various objective-lens diaphragms and image modes.

## CHAPTER 6

### IMAGE ANALYSIS 2

#### Morphometrical- and qualitative analysis of electron energy-loss images.

This chapter has been published in *Ultramicroscopy* **32** (1990), p. 69-79.

*Quantitative energy-filtered image analysis in cytochemistry II. Morphometric analysis of element-distribution images.*

Sorber C.W.J., Van Dort J.B., Ringeling P.C., Cleton-Soeteman M.I. and De Bruijn W.C.

#### SUMMARY

A combination of energy-filtered transmission electron microscopy (EFTEM) and an image-analysis system (IBAS-2000) is used for a morphometric analysis of chemical reaction products in cells. Electron energy-loss spectroscopic element-distribution images are acquired from cytochemical reaction products in a variety of cellular objects:

- (1) colloidal thorium particles in extra-cellular coat material,
- (2) iron-containing ferritin particles in liver parenchymal cells,
- (3) barium-containing reaction products in endoplasmic reticulum stacks,
- (4) elements present in lysosomal cerium- and barium-containing precipitates connected with acid phosphatase (AcPase) or aryl sulphatase (AS) enzyme activity.

Areas or area fractions are determined from such element distribution images by application of an objective image segmentation method. By superposition of two or more element-distribution images, mutual element relations are qualitatively established in lysosomal cerium- and barium-containing precipitates connected with acid phosphatase (AcPase) or aryl sulphatase (AS) enzyme activity.

By comparing electron spectroscopic (ESI) with element-distribution images, the mutual contrast per element relations are quantitatively investigated. The

obtained gain in resolution in such electron energy-loss spectroscopic element-distribution images will be explained and discussed.

## INTRODUCTION

To monitor, for integrated cytochemical and morphometric image analysis, changes in cytochemical product volume in patient material, attention has to be paid to the morphometric determination of area or area fractions in element-distribution images. In addition to the qualitative information about mutual element relations, the relation of the area(s) occupied by the element(s) to the total area of the item of interest has to be established.

Energy filtered transmission electron microscopy (EFTEM) [Adamson-Sharpe & Ottensmeyer (1981); Arsenault & Ottensmeyer (1983, 1984); Peachy *et al.* (1986); Trinick & Berriman (1987); Zaluzec (1985); Hezel *et al.* (1986); Hezel *et al.* (1987)] potentially allows morphometric analysis of element-distribution images and image integration of element-distribution images to those defined by contrast.

In this chapter net-intensity element-distribution images will be morphometrically analyzed with the use of an image analyzer (IBAS 2000, Zeiss/Kontron), in a type of post-acquisition digitization. Element net-intensity image acquisition has been used before in TEM [Adamson-Sharpe & Ottensmeyer (1981); Arsenault & Ottensmeyer (1983,1984); Peachy *et al.* (1986), Trinick & Berriman (1987), Hezel *et al.* (1986), Hezel *et al.* (1987)] and STEM [Zaluzec (1985); Sorber *et al.* (1990a); Colliex *et al.* (1984); Colliex (1985); Colliex *et al.* (1986)]. Quantification of such images is considered to be rather complicated, because spectrum deconvolution is still a subject of investigation [Pun *et al.* (1984); Egerton (1986)]. In this chapter a two-window method is used as proposed before by Arsenault & Ottensmeyer (1983), Ottensmeyer (1984), which leads to semi-net-intensity element-distribution images. Programs for multi-window subtraction procedures (chapter 7-8) were not installed in our computer at the time of investigation. Morphometric analysis of such semi net-intensity element-distribution images will be performed by an objective segmentation method similar to that proposed for the ESI images (chapter 5).

Co-localization of elements introduced by multiple cytochemical reactions will be investigated by super-position of semi-net-intensity images [Arsenault & Ottensmeyer (1984); Colliex *et al.* (1984)]. Finally, the area of a lysosome

## Chapter 6

( $\Delta E = 250$  eV) will be determined and, by combining ESI images with element-distribution images, the sum-area of all elements enclosed will be compared with the area acquired by contrast.

The anticipated gain in chemical spatial resolution of EFTEM over electron probe microanalysis (EPMA) [Colliex (1985)] will be demonstrated and the improvement of the morphometric accuracy obtained by EFTEM (as compared to EPMA) will be discussed.

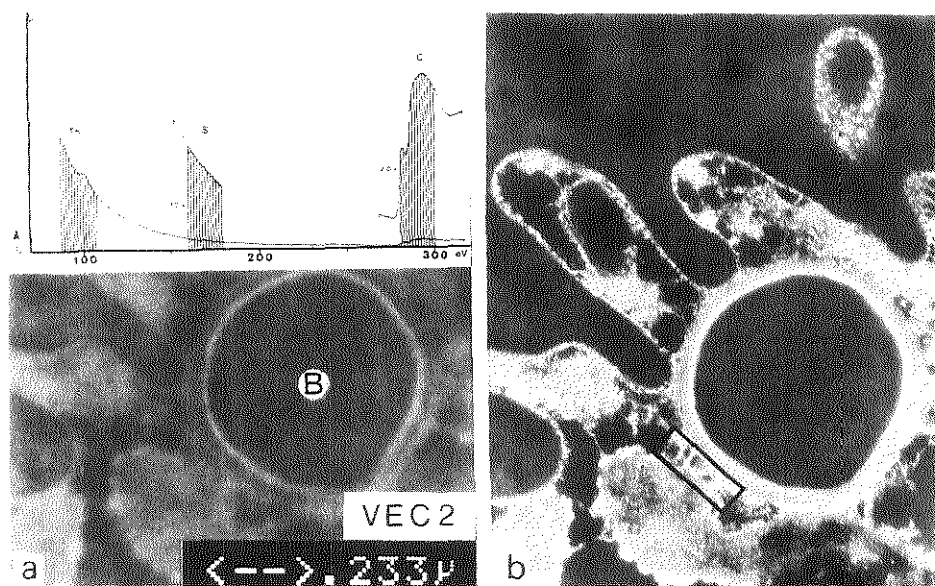


**Figure 6.1.** Colloidal thorium particles reacted with acid mucopolysaccharides in the cell coat from human vaginal epithelial cells. (a) The pre-ionization edge image (PIE); B indicates a bacterium present in that habitat; (b) The ionization-edge image (IE) at  $\Delta E = 88$  eV. In the inset in (a) a spectrum of the colloidal thorium product is shown plus the width of the thorium window. In (b) the area is indicated in which the diameter of the colloidal thorium particles is measured at high magnification.

## RESULTS

Morphometric analysis is divided in two main parts:

- single net-intensity element-distribution images and,
- multiple net-intensity element-distribution images.

For morphometric analysis of single element-distribution images, three examples will be described. The particle area/diameters will be measured in binary images from:

- (a) monomorphic colloidal-thorium particles in a cell coat at the cell surface. Whereas the area fractions will be determined for two different situations:
- (b) for monomorphic particles present in cells in a tissue,
- (c) for heteromorphic particles present in single cells.

### *Monomorphic particles at a cell surface*

In Fig. 6.1, the reaction of the acid mucopolysaccharide ligands in the cell coat with positively charged colloidal thorium particles is shown. In the PIE image (Fig. 6.1a) no colloidal particles are observed. In the IE image (Fig. 6.1b) the presence of the colloidal particles is evident. In the inset of Fig. 6.1a, a spectrum of the extra-cellular colloidal thorium particles is shown. The absence of sulphur is indicated; the presence of carbon is shown. In Fig. 6.1b, the area in which the particles are measured at higher magnification is surrounded by a rectangle. The mean particle diameter measured from the binary net-intensity thorium images was  $2.44 \pm 0.33$  nm ( $n=65$ ). The mean minimum diameter of the oval particles was 1.60 nm. The shape factor was 0.64, morphometric accuracy: 25 pixels/ particle.

### *Monomorphic particles in cells in a tissue*

In Fig. 6.2, ferritin particles present in rat liver parenchymal cells are shown. Fig. 6.2a shows the acquired net-intensity iron-distribution image of the lysosomal and cytoplasmic area. Fig. 6.2b shows part of a spectrum, between 680-740 eV, from the iron-containing lysosome. The 20 eV wide energy bands used for the PIE and IE images are indicated. Fig. 6.2c shows the zero-loss image from the same site. In the square areas in Figs. 6.2a and 6.2c, single iron cores are marked. To determine the area fraction of ferritin-particles in iron-loaded rat liver parenchymal cytoplasm, iron net-intensity images are acquired from randomly chosen cytoplasmic areas at constant magnification. In that case the frame area is the reference area. Cytoplasmic ferritin particles are initially assumed to be sufficiently

separated to be measured individually. We used the first derivative- of the grey-value frequency histogram for objective segmentation as described in chapter 5. In the cytoplasmic areas the total area of the ferritin iron-core particles is measured. As the total area of the frame is known, the ferritin iron-core area fraction can be determined ( $2.758 \times 10^{-3}$ ). In addition, the number of iron-core particles per cytoplasmic area is determined with the IBAS program COUNT. The mean ferritin iron-core particle area is subsequently established by dividing the total particle area by the number of particles. Assuming the cytoplasmic iron cores to be spherical, the averaged mean core diameter is calculated from 19 ( $0.54 \mu\text{m}^2$ ) cytoplasmic fields, leading to a mean value for ferritin iron-cores of  $5.93 \pm 0.46 \text{ nm}$  (morphometric accuracy = 54 pixels/Fe-core, shape factor = 0.8139, n = 2400 particles).

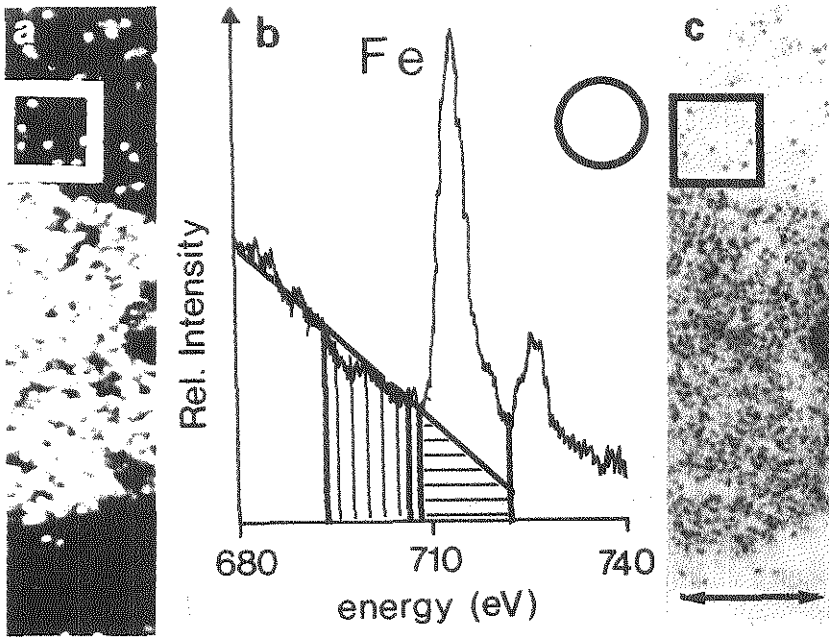


**Figure 6.2.** Cytoplasmic (square) and lysosomal ferritin particles in a rat liver parenchymal cell. (a) The iron net-intensity image; (b) Spectrum of a lysosomal ferritin containing area. The PIE (///) and IE (≡) windows are indicated. The circle represents the analyzed area to scale. (c) The zero-loss image. The square areas in (a) and (c) indicate identical cytoplasmic ferritin iron-cores. Bar = 270 nm.

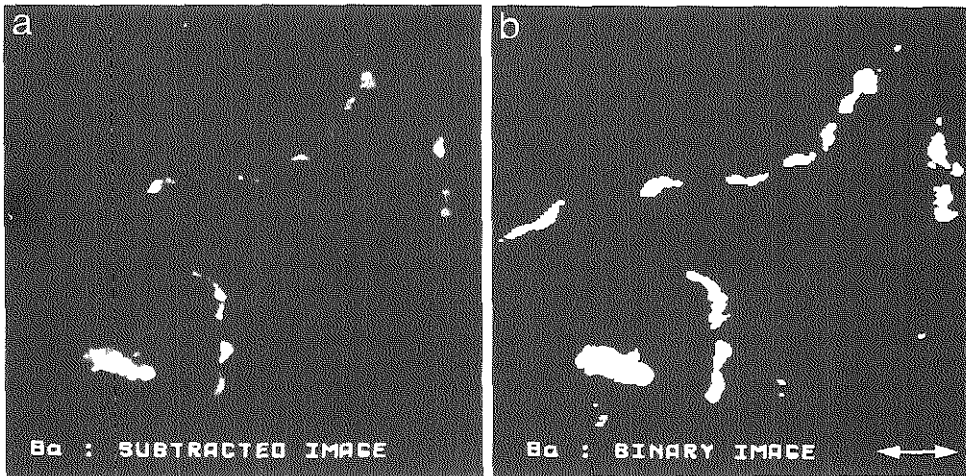


**Figure 6.3,** Barium precipitates in the endoplasmic reticulum stacks of a mouse peritoneal macrophage. (a) The barium net-intensity image. (b) The binary image after objective segmentation. Bar = 150 nm.

#### *Irregularly shaped particles*

Barium precipitates in intracellular rough endoplasmic reticulum stacks are measured in a similar way as described for ferritin iron cores. The net-intensity barium image is shown in Fig. 6.3a. The segmented binary image is shown in Fig. 6.3b. In the binary image the total barium-containing area is determined. Then the total area cross-section of the cell is determined (see colour plate in chapter 5, Fig. 5.5a) and the area fraction of this precipitate is calculated ( $1.5 \times 10^{-3}$ ).

The morphometric analysis of multiple element semi-net-intensity images is shown in Figs. 6.4-6.5. In Fig. 6.4a, part of a spectrum ( $\Delta E = 750$  to  $950$  eV) from a lysosomal area ( $232 \text{ nm}^2$ ) containing barium and cerium is shown. Much smaller edges have been obtained from phosphorus between  $\Delta E = 100$  eV and  $200$  eV (Fig. 6.4b), whereas a sulphur edge failed to show up clearly. In Figs. 6.5a-6.5h, a lysosomal aryl sulphatase-derived barium sulphate precipitate is used to demonstrate that when in a spectrum a clear ionization edge is present, (IE)-(PIE) subtraction procedures result in a bright image, (Figs. 6.5d, 6.5f, 6.5h) comparable to the ESI image at  $\Delta E = 250$  eV (Fig. 6.5b).

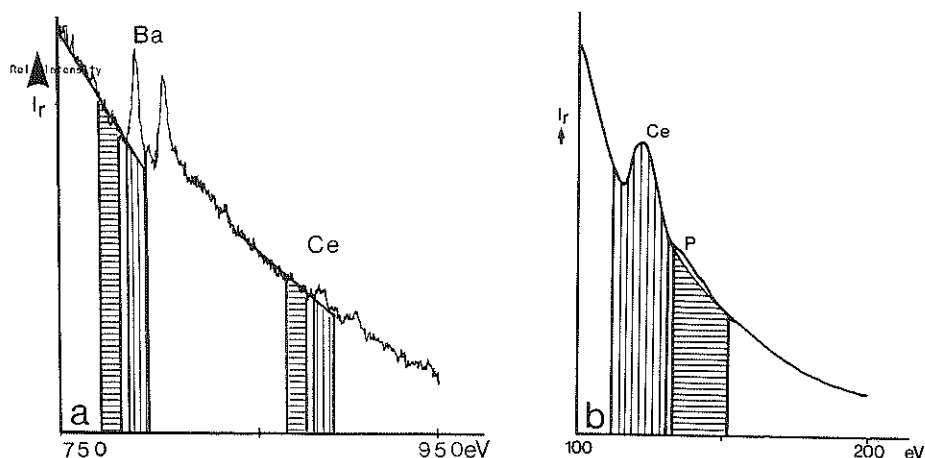
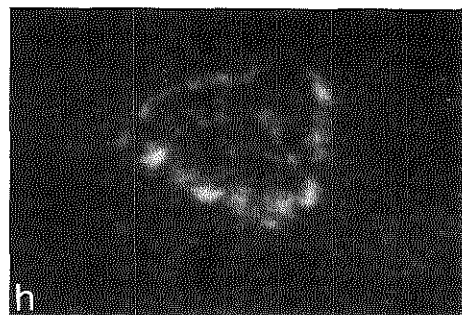
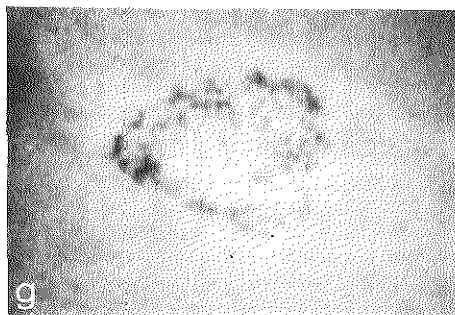
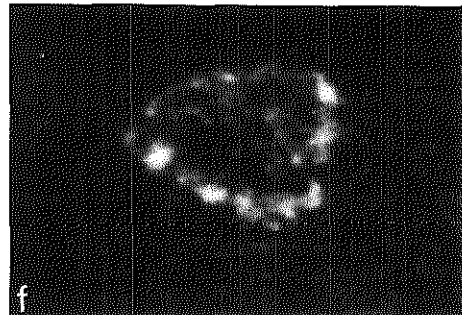
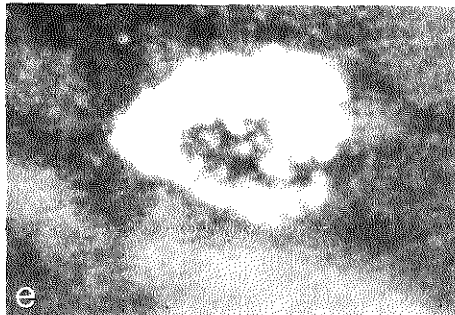
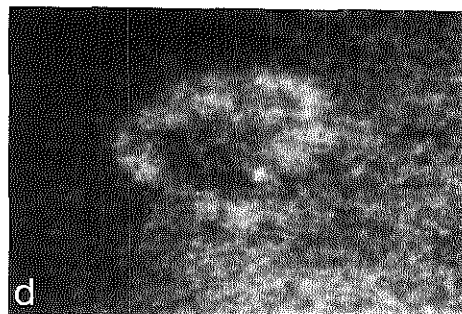
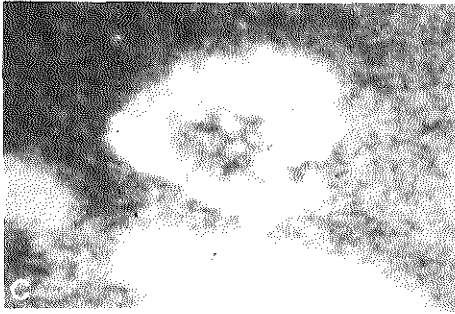
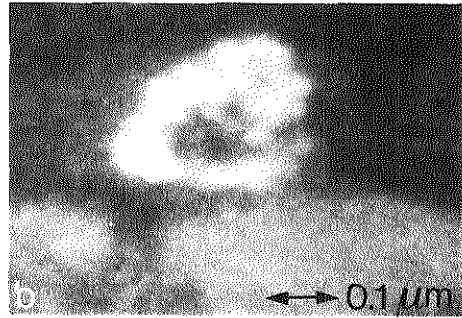
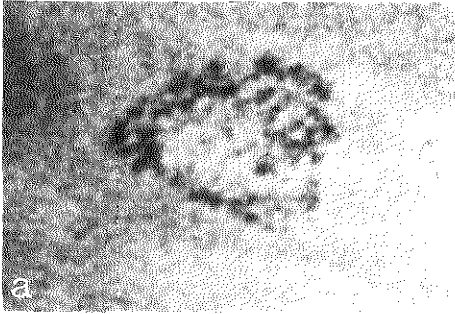


**Figure 6.4.** Spectra from a multiple element-containing lysosomal precipitate. In (a) the presence of barium and cerium is indicated and the PIE (≡) and IE (///) windows. In (b) the phosphorus edges are shown plus the cerium  $N_{4,5}$ -edges and the phosphorus PIE (///) and IE (≡) windows.

**Figure 6.5.** (Opposite page) Multiple images from the same mouse peritoneal macrophage lysosome in which it will be shown that subtraction of the PIE image (d) from the IE image (f) results in a bright image (barium net-intensity image (h)) of which the intensity is comparable with the  $\Delta E = 250$  eV ESI-image (b), provided clear edges are present in the spectrum (see Fig. 6.4a). When in the spectrum edges are absent, like for sulphur (see Fig. 6.4b), IE-PIE subtraction (e, c) gives a resultant image with black "holes", which is comparable with the zero-loss image (a). Bar = 550 nm. (c) PIE-image of sulphur  $\Delta E = 144$  eV + 20 eV; (d) PIE-image of barium  $\Delta E = 761$  eV + 20 eV; (e) IE-image of sulphur  $\Delta E = 184$  eV + 20 eV; (f) IE-image of barium  $\Delta E = 801$  eV + 20 eV; (g) Difference image (IE-PIE) of sulphur showing the absence of any semi net-intensity sulphur as black holes; (h) Difference image (IE-PIE) of barium showing the presence of semi net-intensity of barium as white particles.



When in the spectrum the edge is very low and riding on a steep continuum (e.g. the sulphur peak at  $\Delta E = 164.8$  eV) the resultant image after a similar subtraction operation (Figs. 6.5c, 6.5e, 6.5g) shows black holes, comparable to the particles in the zero-loss image (Fig. 6.5a).

Spectral information (Fig. 6.4a-b) indicated already the co-occurrence of AcPase-related cerium phosphate and AS-related barium in the analyzed lysosomal area. From all three elements involved (barium, cerium and phosphorus) element-distribution images are acquired as described above.

From each element-distribution image, binary images are obtained by grey-level histogram-based segmentation. These images are collected in a colour plate in chapter 5, Figs. 5.5c-h. In Figs. 5.5c, 5.5e, 5.5g, binary distribution images are shown from the individual elements in pseudo colours. To demonstrate presence or absence of co-localization, we used superposition of two images and new bright pseudo colours (white, yellow) were attached to the overlapping pixels (Figs. 5.5d, 5.5f, 5.5h) In this particular case, cerium and phosphorus were expected to be found in register, whereas barium (and sulphur), preferably should be located at a different location. In Figs. 5.5c and 5.5e, cerium and phosphorus are depicted separately. In Fig. 5.5d, these images are combined visualizing both elements in the original colours, and showing in white, the pixels, where the two elements coincided. In Fig. 5.5g, the presence of barium is shown. In Fig. 5.5f, cerium and barium images are superimposed showing the virtual lack of coincidence by the absence of the yellow colour. In Fig. 5.5h, cerium, phosphorus and barium are superimposed to show some additional (undesired) coincidence between barium and phosphorus.

Morphometric analysis, also results in area fractions from these irregular-shaped lysosomal element-containing particles (chapter 5, Figs. 5.5a-b). By converting relative area into real area, two particle areas are obtained from the same lysosome. ESI-image segmentation (Fig. 6.5b) results in an area of 23,480 nm<sup>2</sup>. The area calculated by summation of all element binary images (Fig. 5.5h) is 23,020 nm<sup>2</sup>, lacking 460 nm<sup>2</sup> ( $= \pm 1.5\%$ ). As an element-distribution image of the peroxidase-related platinum-containing poly DAB reaction product is not acquired, theoretically the missing area could be occupied by this reaction product.

## DISCUSSION

A two-population distribution is obtained in the greyvalue histogram of element-distribution images which similarly can be used for an objective segmentation procedure. Limitations encountered with our segmentation procedure based upon contrast, described before for ESI images, are not different from the ones encountered for element-distribution images. Recently Trebbia (1989) indicated, that the degree of confidence about the absence or presence of the items of interest in final images is determined by the signal to noise ratio (SNR) (see also Egerton (1986)). He warned not to easily accept the presence of elements at sites where they are expected. Trebbia considers the two-window acquisition procedure for net-intensity element-related images followed in this chapter, inappropriate. However, when edge-intensities are high (as in cytochemical precipitates) and the IE-window in the energy spectrum is at a large distance from the origin (Fe = 708 eV, Ba = 781 eV, Ce = 883 eV) subtraction of the PIE image from the IE image may be acceptable. We realize that this aspect is more complicated and needs further investigation, hence we call our resultant images "semi-net-intensity images", to indicate our awareness of the restriction. Correct procedures for quantification of EEL spectra have been outlined [Pun *et al.* (1984); Egerton (1986); Joy & Maher (1981)].

The two-window method becomes critical when the element edges are located on the steep flank at the low-loss side of the spectrum (thorium  $O_{4,5}$  = 88 eV, phosphorus  $L_{2,3}$  = 132 eV, sulphur  $L_{2,3}$  = 165 eV). However, only sulphur failed to appear, while phosphorus and thorium were clearly detected. However, the subtraction procedure at the phosphorus edge (and probably also the sulphur edge) suffers from the cerium and barium  $N_{4,5}$  edges at 105-125 eV and 100-120 eV, respectively. So the confidence level of our phosphorus distribution image is low. Our (disputable) subtraction procedure may lead to an under-estimation of the area. This might be a reason why in the examples chosen (*viz.* cerium/phosphorus) the localization does not completely coincide. In the case of barium and cerium the obtained separation might be caused by this underestimation.

The high spatial resolution in EELS analysis reported earlier [Adamson-Sharpe & Ottensmeyer (1981); Arsenaault & Ottensmeyer (1983, 1984); Zaluzec (1985); Ottensmeyer (1984)] has been confirmed. In the element semi net-intensity images shown here (Fig. 6.1b, Th: 2.4 nm; Figs. 6.2a-c, Fe: 5.9 nm; in chapter 5, Figs. 5.5c-5.5h, Ce, Ba and P: < 10 nm), the spatial element-related resolution is better

than that obtained earlier with EPMA from similar material [Van Dort *et al.* (1989); De Bruijn *et al.* (1987)]. This improvement is not only related to EELS as an analytical tool or to the microscope system to which it is attached, but is predominantly attributable to the acquisition systems employed: TEM versus STEM. Recently the following instrumental magnitudes have been formulated for high resolution STEM/EPMA [De Bruijn *et al.* (1987)], which determine the interpixel distance (IPD) at the specimen level and hence the resolution:

$$IPD_{sp} = d_{sp} = \frac{d_{sc} F^*}{M N F} \quad (6.1)$$

In this equation  $d_{sp}$  and  $d_{sc}$  are distances on specimen and screen respectively,  $M$  is the magnification,  $N$  is the number of pixels/points (per line) and  $F$  and  $F^*$  are reduction factors when part of the screen ( $F$ ) or fewer than 1024 points ( $F^*$ ) are used. For STEM records four lines per particle were proposed to be acceptable as a minimum, resulting in a resolution of:

$$d_{min} = 4 IPD_{sp} \quad (6.2)$$

Accordingly, 16 pixels/particle determines the minimal accuracy.

There are no theoretical limitations to obtaining high spatial resolution images with STEM systems, when a sufficiently intense field emission source with 1 nm spot size can be used. But in practice EFTEM images can be acquired at much lower magnification without sacrificing spatial resolution due to the employed post-acquisition image-analyzer system. For years, ferritin particles have been used as a test specimen [Zaluzec (1985)]. Our failure to acquire iron net-intensity images from such particles in situ by EPMA/STEM analysis [De Bruijn *et al.* 1987] could be attributed to the spot size/maximal intensity which can be obtained in practice with the LaB<sub>6</sub> cathode. Our ESI/TEM and (colloidal) particle-area analyses in element-distribution images provide arguments in favour of the combination of EFTEM with a post-acquisition analyzing system, especially when the aspect of morphometric accuracy is taken into account (25 or 50 pixels/particle). However, Young calculated for the digitization of a perfect circle, analyzed in a similar way, a percentage absolute area error of 7-8% for such low sampling densities [Young (1988)].

Additional gain by EFTEM acquisition can be found in the total acquisition time per digitized image, as compared to the time needed to acquire the EPMA/

STEM- images. The acquisition of a STEM/EPMA full screen 256 x 256 image using a dwell time of 1 sec. per pixel/point requires a total acquisition time of 18.2 h [De Bruijn *et al.* (1987)]. One (100 x integrated) shading corrected, 512 x 512 full screen, TEM image takes four acquisitions of about 10s each.

Several images can be taken in a short time from the same specimen, as long as computer image-storage capacity is not limited. However, differences in total electron dose favour the use of STEM instruments. On the other hand, the time needed to calculate true EFTEM element concentration images might take several hours, although in that case such calculations can be performed off-line (chapter 7-8).

An additional advantage of EFTEM analyses might be the reduction of the influence of beam-broadening, by the absence of a (tilted) support film. On the other hand, element EELS quantification has just started [Pun *et al.* (1984); De Bruijn & Van Miert (1988); Liu & Brown (1987)]. Chelex<sup>100</sup>-based Bio-standards (Bio-Rad/Polaron, Hemel Hempstead, Hertfordshire, U.K.) used extensively already for EPMA analysis [Arsenault & Ottensmeyer (1983); De Bruijn *et al.* (1987); Mostert *et al.* (1989); De Bruijn (1981a, 1981b); De Bruijn (1984); Roos & Barnard (1984)] have been shown to be as successfully applicable for EELS analysis [De Bruijn *et al.* (1989); Van Dort *et al.* (1988)].

In conclusion, the following statements can be made:

- 1 Application of a two-window subtraction procedure results in semi-net-intensity images, if the ionization edge is far beyond the low-loss region and sufficiently high (barium, cerium, thorium). If that is not the case (sulphur), the procedure breaks down. For phosphorus, in spite of the positive results, the degree of confidence of such net-intensity element distribution images is low, due to the presence of a cerium edge in the PIE window of the phosphor edge.
- 2 Morphometric analysis of such semi-net-intensity element-distribution images results, after objective image segmentation, in binary element-related images from which areas or area fractions can be determined.
- 3 The spatial resolution obtained in such element-distribution images from regularly and irregularly shaped particles is shown to be between 1.5 and 5.9 nm.
- 4 Superposition of pseudo-coloured images of multiple-element-containing precipitates is used to visualize the presence (cerium and phosphorus) or absence (cerium and barium) of co-localization.

## Chapter 6

---

- 5 The gain in accuracy following the application of image analysis with the combination Zeiss EM902/IBAS 2000, as compared to EPMA/STEM, is related to the differences in digitization of the two systems: during image acquisition (EPMA/STEM) or after image acquisition.
- 6 As a consequence of these differences (•1-•5), the use of the Zeiss EM902/IBAS 2000 combination will result in:
  - a high element-related spatial resolution at low magnification,
  - multiple images that can be acquired in a relatively short time,
  - a situation in which shading correction and noise reduction can be incorporated in the acquisition,
  - a reduction of beam broadening due to the use of thin sections and the absence of a supporting film, and
  - improvement of geometric accuracy due to absence of specimen tilt.

---

# **CHAPTER 7**

## **IMAGE ANALYSIS 3 CONCENTRATION MEASUREMENTS IN ELECTRON ENERGY-LOSS IMAGES**

### CHAPTER 7

#### IMAGE ANALYSIS 3

##### Concentration measurements in electron energy-loss images

### SUMMARY

For the quantification of the concentration of the various elements in an ultrathin section several basic steps have to be performed.

Since relative elemental concentrations ( $R_x$ ) to be calculated are based upon the data beyond the edge, a reliable determination of the ionization edge is a prerequisite. Several methods to determine the ionization edge objectively in EEL-spectra are investigated. Furthermore, an analysis of the influence of the location ( $E_\Delta$ ) and width ( $W_\Delta$ ) of the  $\Delta$ -region (the region beyond the edge used for quantitative analysis) on the acquired  $R_x$ -value in Bio-standards is presented.

Based upon these results, experiments to determine  $R_x$ -values in images are described. Several methods (Two-area, linear and power-law) to calculate the background image ( $I_B$ ) are investigated. The power-law method gives the best results.

Subsequently several aspects to acquire concentration distribution images are considered.

Relative concentrations as obtained from images were compared with  $R_x$ -values as obtained from spectra. To obtain image results comparable to spectral results, the ionization edge images are to be recorded with a 15 eV slit-width at least 10 eV beyond the ionisation edge.

### INTRODUCTION

Several basic steps have to be performed to allow quantification of the concentration of the various elements in ultrathin sections. Much effort has been put in the development and implementation of various methods for concentration measurements. In this chapter the following problems will be addressed:

- 1 Stability of the position of the ionisation edge ( $E_{IE}$ ).

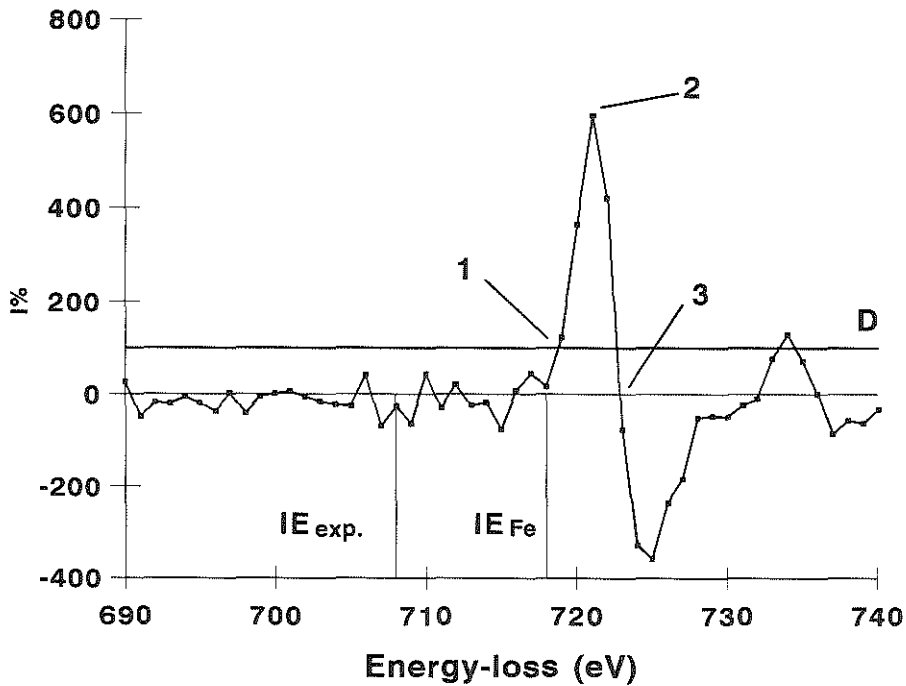


**Figure 7.1.** Three methods for determining the position of the ionization edge ( $IE$ ) using the first derivative of the EEL-spectrum.  $IE_{Fe}$ : The ionization edge position;  $IE_{exp.}$ : The expected ionization edge position; D: Preset noise-dependent detection level.

- 2 Dependence of the relative iron-concentration in spectra ( $S_{R_x}$ ) on position ( $E_{\Delta}$ ) and width ( $W_{\Delta}$ ) of the  $\Delta$ -region.
  - 3 Determination of the relative iron-concentrations in images ( $I_{R_{Fe}}$ ).
  - 4 Calculating element-distribution images using element specific energy-loss images and zero-loss images.
  - 5 Comparison of the  $I_{R_{Fe}}$  and  $S_{R_{Fe}}$  values from siderosomes and Fe-Bio-standards.
- 1 For quantitative analysis, many parameters, reflecting instrument-settings and/or properties of analytical procedures may influence the results obtained. One of the parameters is the location of the ionization edge. Both in quantitative spectral analysis (QSA) and quantitative image analysis (QIA) the ionization-edge position ( $E_{IE}$ ) plays an important role, so its determination must be reliable. To determine

the ionization edge objectively, three methods were tested, all involving the calculation of the first derivative of the spectrum (Fig. 7.1). The edge is then identified at the energy-loss where:

- a The first derivative crosses a preset noise-limit ( $D$ ) which is usually  $3\sigma$  of the base-line.
- b The first derivative reaches its maximum value.
- c The first derivative becomes negative beyond its maximum.

The last two methods do not depend on a preset noise level whereas the first one does. With all three methods a constant has to be subtracted to obtain  $E_{IE}$ , since the methods do not determine the edge itself but a position just beyond the edge. In most cases procedure •a is used.

Instrumental drift of the ionization edge over time may cause false interpretation of the obtained results. Multiple spectra were taken over a time period of two hours to examine whether a correction for instrumental drift has to be performed to allow identification of the edges. Recalibration of the energy-loss scale between the spectral acquisition is a possible correction-method for this drift. Zero-loss correction, however, may cause problems of instrumental nature (overflow). Therefore, the possibility of the use of the C-edge for calibration purposes (chapter 3) will also be investigated using method •a.

•2 Another set of instrumental settings to be investigated is the width ( $W$ ) and position ( $E$ ) of the fitting-region ( $\Gamma$ ) and of the region used for the analysis ( $\Delta$ ). The  $R_x$ -values, acquired from homogeneously-loaded ultrathin-sectioned Bio-standards have been shown to be constant within the beads and between beads ( $\pm$  a standard deviation of 12-20% (chapter 3)). The constant value from sectioned Bio-standards was acquired with a fitting- and integration-region of 50 eV each ( $W_\Gamma/W_\Delta = 50/50$ ). In some cases the  $\Gamma$ -region was restricted to a width of 30 eV e.g. for calcium ( $W_\Gamma/W_\Delta = 30/50$ ).

Very recently, the new developments in relation to EELS-spectroscopy and -imaging have been reviewed in retrospect [Reimer & Ross-Messemer (1991); Krivanek *et al.* (1991)] and in prospect [Stobbs & Boothroyd (1991)]. For qualitative image analysis with the Zeiss EM902, the use of 10-15 eV-wide slits is advocated. In most cases the ionization edge image is recorded directly beyond  $E_{IE}$  but other positions can be chosen. The acquisition of images with 50 eV wide slits has been considered to be undesirable (e.g. because of chromatic aberration [Kruit & Shuman (1985); Titchmarsh & Malis (1989)]). The influence of the position and

width of the slit on the value of  $R_x$  was experimentally determined by quantitative spectrum analysis. Since QIA is QSA repeated many times, the results are valid for QIA as well.

•3 For years the quantitative determination of the element concentration has been performed by the acquisition of spectra from an analyzed area in an image. Much attention has been paid to the mathematical aspects of the fitting of an appropriate function through the continuum of an EEL-spectrum [Egerton (1986); Pun *et al.* (1985); Sorber *et al.* (1991a); De Bruijn *et al.* (1991)]. In most cases it is assumed that the continuum of EELS-spectra is described by an inverse power law model (eq. 1.1). Similarly, several background estimation techniques can be applied to image-analysis. Thus, a number of images in the pre-ionisation edge (PIE) region ( $I_{PIE}$ ) is acquired to estimate a background-image ( $I_B$ ) by extrapolation beyond the ionization edge. Such a background-image is then subtracted from the ionization edge image ( $I_{IE}$ ) to yield a net-intensity element-distribution image ( $I_L$ ).

The average grey-value of all pixels in the images was used as an equivalent of the integral of the images. The net-intensity image value ( $I_L$ ) is then related to the IE-image value ( $I_L + I_B$ ) in order to obtain an estimate of  ${}^1R_x$ :

$${}^1R_x = \frac{I_L}{I_L + I_B} = \frac{I_{IE} - I_B}{I_{IE}} \quad (7.1)$$

Three alternatives of background-estimation were investigated (Fig. 7.2), one using a single PIE-image as the background-image (a), the others calculating the background-image as an extrapolation of several PIE-images either linearly (b) or according to an inverse power-law (c). The results of these three methods were compared using the area-fractions and  ${}^1R_x$ -values. The slitwidth initially used was 15 eV.

•4  $R_x^*$ -measurements have always been a problem with serial EELS, both for spectra and images. The high intensity-differences between the ESI-region and zero-loss region cause instrumental overflows. To solve this problem for images, attenuation filters were introduced in the optical pathway to the camera when recording zero-loss images with ESI-settings (chapter 2). Element concentration images were calculated as the ratio of the resultant net-intensity image and the zero-loss image.

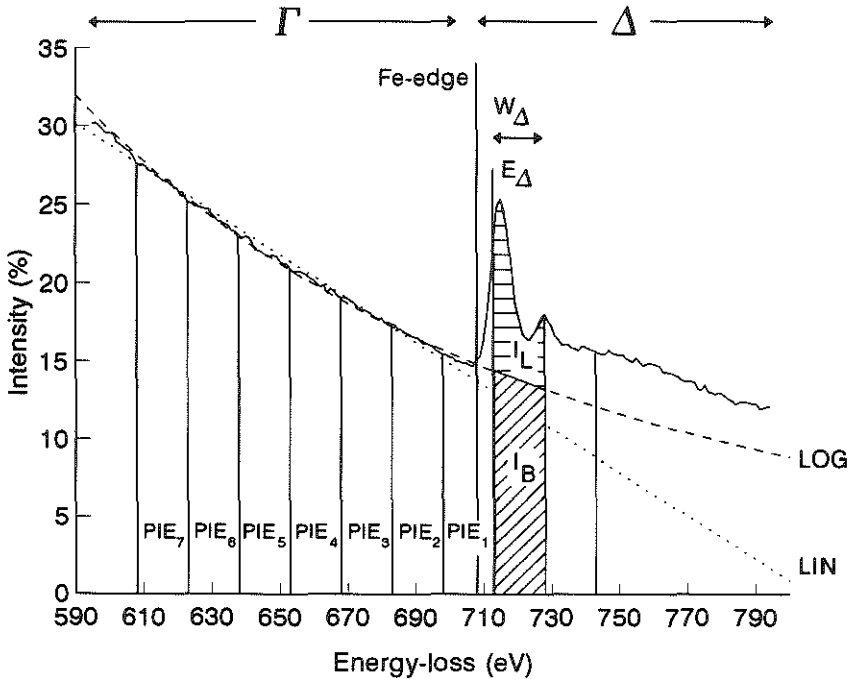


**Figure 7.2,** Illustration of three possible methods to estimate the background image ( $I_B$ ): Using the  $PIE_1$ -image as background-image, linear (LIN) and logarithmical (LOG) extrapolation of the continuum.  $PIE_{1,2,n}$ : pre-ionization edge images;  $I_L$ : the element-related part of the ionization-edge image;  $I_B$ : the background part of the ionization-edge image;  $\Gamma$ : part of the spectrum used for continuum estimation;  $\Delta$ : part of the spectrum used for quantification of the element;  $W_\Delta$ : width of the  $\Delta$ -region;  $E_\Delta$ : energy-loss position in the  $\Delta$ -region.

•5  $R_x$  values obtained with QSA and QIA from the same analyzed area ( $1.54 \mu\text{m}^2$  at a 30,000x magnification in the Zeiss EM902) were compared using Bio-standards.

## MATERIALS AND METHODS

The EEL-spectra acquisition chain and the image acquisition chain have been

described in chapter 2.

•1 The three methods to determine the position of the ionization edge  $E_{IE}$  mentioned in the introduction were investigated using two series of 13 spectra each. For each of the two series, a standard deviation of the  $E_{IE}$ -values, as obtained using the three methods, was determined. The first derivative of an original Fe-spectrum, obtained by convolution with the kernel [1,-1], is shown in Fig. 7.1.

For the determination of the IE-edge stability, two series of 13 spectra each were recorded over one hour and over two hours, respectively.

•2 Experiments to determine the influence of the position and width of the integration region on the calculated  $R_x$ -values in spectra were performed using three Bio-standards (Fe, Ca and Ce). To investigate the effect of the width  ${}^S W_{\Delta}$  and position  ${}^S E_{\Delta}$  on  ${}^S R_x$ , 4 different values for  ${}^S W_{\Delta}$  were selected (5, 10, 15 and 20 eV) and  ${}^S E_{\Delta}$  was incremented with one eV from  $E_{708}$  onwards. For each position  ${}^S R_x$  was determined automatically. The computer program first estimates the background using the Simplex method [Sorber *et al.* (1991a); De Bruijn *et al.* (1991)] with a  $\Gamma$ -region of 50 eV, then it calculates  ${}^S R_x$ .

•3 To determine  ${}^I R_{Fe}$  with three different background-estimation methods, two ionization edge images of an iron Bio-standard were examined (713 eV and 728 eV). Slit width = 15 eV. Two PIE-images were recorded (648 eV, 688 eV).

•4 For the determination of iron concentration-distribution images, 8 energy-filtered images were serially acquired over a 100 eV range between 638-738 eV, at 20 eV intervals. Subsequently an attenuation filter of O.D.=5 is introduced in the light path to the TV-camera and with the same camera setting two images in the zero-loss region are recorded (0 and 20 eV). After extrapolation of the continuum using a linear fitting algorithm calculated from the 6 pre-edge images,  $I_B$ -images of the 718 eV and 738 eV images were calculated and divided by the zero-loss images to obtain  ${}^I R_x^*$ -images. This was done both for a siderosome and a Bio-standard. The results from three alternatives were investigated ( $I_{718}/I_0$ ,  $I_{738}/I_0$  and  $(I_{718} + I_{738})/(I_0 + I_{20})$ ).

•5 Ultrathin sections from haemosiderin-containing siderosomes in liver parenchymal cells, co-embedded with iron Bio-standards, were used to compare

relative concentrations as obtained with spectra and images. First 4 images ( $W_{\Delta} = 15$  eV) were acquired (658, 678, 698 and 718 eV) of five siderosomes and five Bio-standards. Next several spectra of the analyzed area were recorded and analyzed, keeping the conditions of the microscope as constant as possible.

### RESULTS

•1 The results of the three methods to obtain an estimate of  $E_{IE}$  applied to iron Bio-standard spectra show that for the noise dependent method •a, the reproducibility as expressed by the standard deviation, is similar to the reproducibility obtained using the noise independent methods 2 and 3 (4.3 eV). In an additional study the standard deviation of  $E_{IE}$  of 200 randomly chosen previously recorded Fe-spectra was found to be 4.3 eV with a mean of 708.9 eV, (using method 1 for the edge-determination).

Recalibration of the energy scale using the C-edge is possible. However, the standard deviation (3.5 eV) did not improve significantly.

The stability test of the ionization edge position showed that the estimate of  $E_{IE}$  decreases with the duration of the experiment (calculated over a period of two hours) the drift being of the order of -0.06 eV/min.

•2 Results of the experiments to test the influence of the location and width of the integration-zone ( $\Delta$ ) on the determination of the  $S_{R_{Fe}}$ -values are illustrated in Fig. 7.3 for the iron Bio-standards. Fig. 7.3 displays the  $S_{R_{Fe}}$ -value as a function of the distance of the lower limit of the  $\Delta$ -region from the real edge ( $E_{\Delta} - E_{IE}$ ). Four curves are acquired with different widths of the integration-zone ( $W_{\Delta} = 5, 15, 30$  and 50 eV, respectively). From these results it is established that:

- (1) With increasing  $S_{E_{\Delta}}$  beyond the IE, the  $S_{R_x}$  value becomes more stable.  $E_{\Delta} - E_{IE}$  must be at least 15 eV, using a slitwidth larger than 15 eV.
- (2) With higher values of  $S_{W_{\Delta}}$ , the  $S_{R_x}$  becomes stable at lower  $S_{E_{\Delta}}$ -values than with small values of  $S_{W_{\Delta}}$ .

The same behaviour is to be expected for images. To obtain reproducible results while recording images, the ionization-edge image should be acquired at least 10 eV beyond the ionization edge.

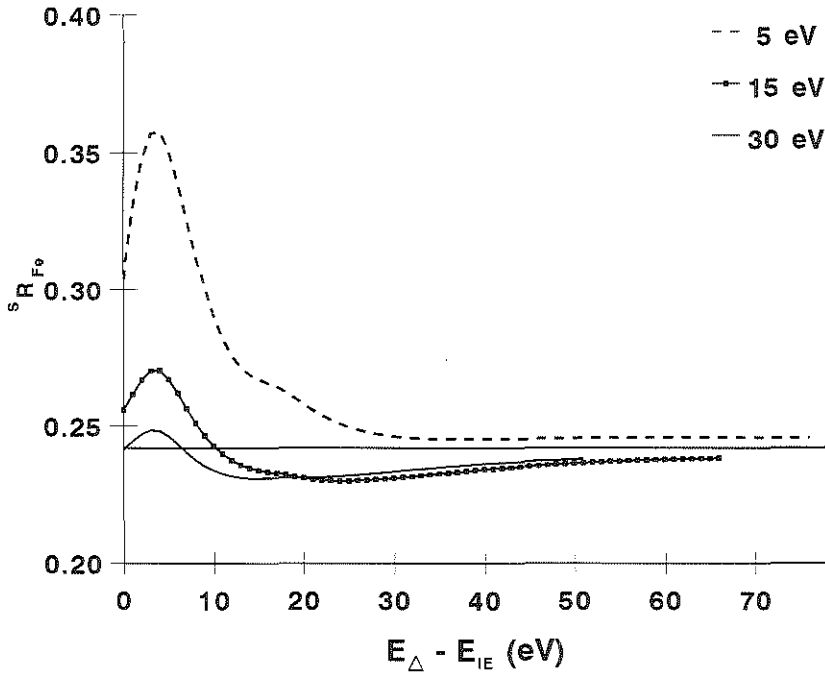


**Figure 7.3.** Influence of the position ( $^S E_{\Delta}$ ) and width ( $^S W_{\Delta}$ ) of the  $\Delta$ -zone on  $^S R_{Fe}$  in Bio-standard spectra.  $E_{\Delta}$ : energy-loss position in the  $\Delta$ -zone,  $E_{IE}$ : ionization edge position.  $^S W_{\Delta} = 5, 15$  and  $30$  eV. The solid horizontal line is the  $^S R_{Fe}$ -value as obtained with  $W_{\Gamma} = W_{\Delta} = 50$  eV.

Method	PIE		Linear		Logarithmical	
	$^I R_x$	Area ( $\mu m^2$ )	$^I R_x$	Area ( $\mu m^2$ )	$^I R_x$	Area ( $\mu m^2$ )
$\Delta E = 713$ eV	0.10	1.54	0.16	1.58	0.13	1.46
$\Delta E = 728$ eV	0.17	1.57	0.20	1.58	0.19	1.57

**Table 7.1.** Results of the comparison of the three methods of background estimation as illustrated in Figs. 7.2 and 7.4. The  $^I R_x$  and the area fractions with respect to the frame area.

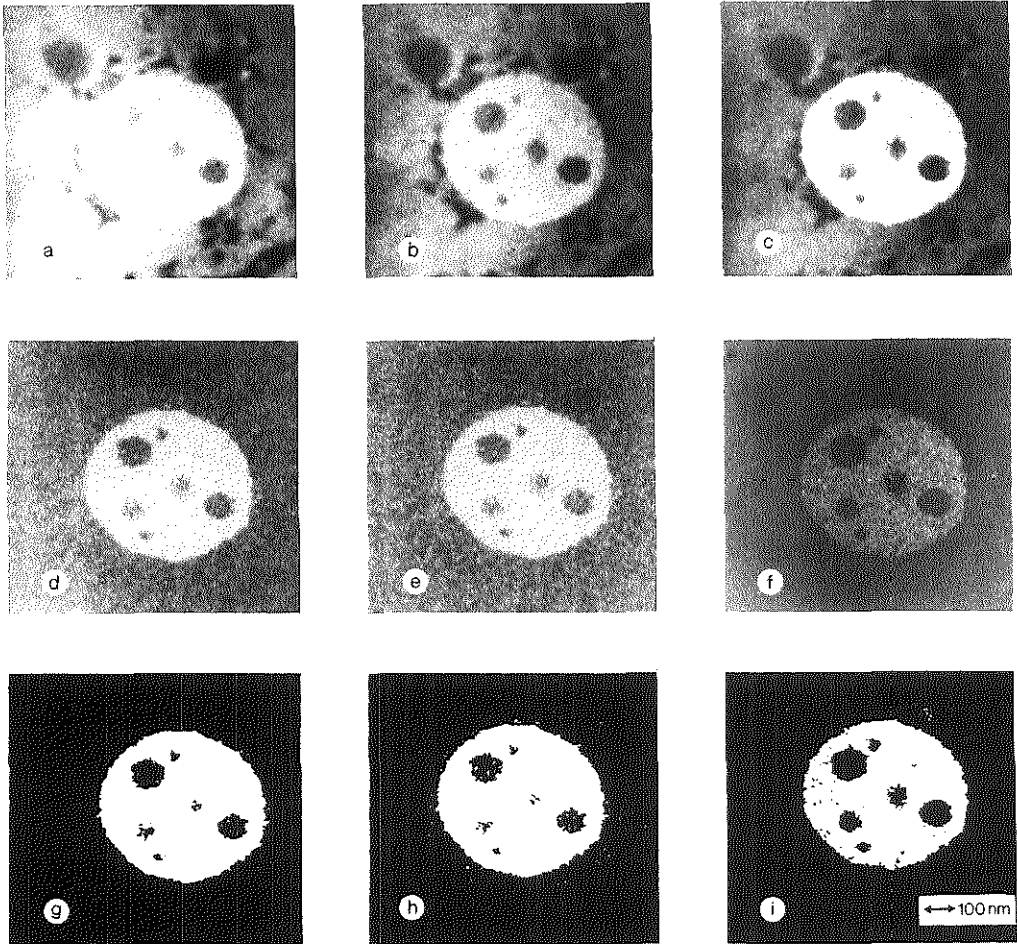


**Figure 7.4,** Comparison of the results of the different background correction methods of Fig. 7.2 as performed on an iron-containing siderosome: PIE<sub>2</sub>-image (a), PIE<sub>1</sub>-image (b), IE-image (c). Resultant images and binary images of: the logarithmical method (d, g), linear method (e, h), PIE-method (f, i). Segmentation was performed as described in chapter two.

•3 For the estimation of the background-image ( $I_B$ ), three methods were investigated (Fig. 7.2). The resulting images are collected in Fig. 7.4. The use of a single PIE-image (Fig. 7.4b) to be subtracted from the IE-image (Fig. 7.4c) clearly gives an over-estimation of the background-image (Fig. 7.4f, i) and thus an under-

estimation of the iron concentration. Much information is lost especially at the boundaries of the siderosome. The linear method preserves more of the iron in the siderosome but also shows extra "iron" around the siderosome (Fig. 7.4e, 7.4h). The method gives a slight under-estimation of the background image resulting in a surplus of iron. Results of the power-law method are intermediate (Fig. 7.4d, 7.4g). These results are in accordance with the expectations as shown in Fig. 7.2. A comparison of the resulting iron area-fractions and the  ${}^1R_{Fe}$ -values (Table 7.1), confirms this observation. Since the background is supposed to follow an inverse power-law, the values acquired by the power-law method are considered to be close to the true area and  ${}^1R_{Fe}$ . Similar results were obtained at the higher  $E_{\Delta}$  position (Table 7.1, 728 eV). The  ${}^1R_{Fe}$  and area-fractions of 728 eV are slightly higher than for 713 eV (which is closer to the ionization edge).

•4 The results of the experiment to obtain element-concentration distribution images using one zero-loss image is shown in Fig. 7.5. After extrapolation of the continuum and subtraction of the background-image thus obtained, the resultant element image is divided by the acquired zero-loss image. The greyvalues in this Fe-concentration distribution image are divided into three regions, representing three different iron concentrations. The mean greyvalue of the centre of the Bio-standard was used for calibration. In the siderosome, areas were observed with a concentration three times as high as this Fe-Bio-standard. The final mean concentration of the analyzed area in the siderosome may be calculated according to:

$$N_{sid} = \frac{R^*_{sid}}{R^*_{st}} \cdot N_{st} \quad (7.2)$$

in which  $N$  stands for the number of atoms in respectively the siderosome (sid) and the Bio-standard (st).

In Table 7.2 the area-fractions of the different greyvalue-regions are shown.

•5 Five iron-containing Bio-standards and five siderosomes, present in the same section were analyzed both with spectra (using the Simplex method, chapter 3) and with images (using the power-law method). The values for  ${}^1R_{Fe}$  and  ${}^5R_{Fe}$  displayed in Fig. 7.6, show the relation between five individual measurements of  ${}^1R_{Fe}$  and  ${}^5R_{Fe}$ .  ${}^5R_{Fe}$  is systematically larger than  ${}^1R_{Fe}$  but the variation is quite high.

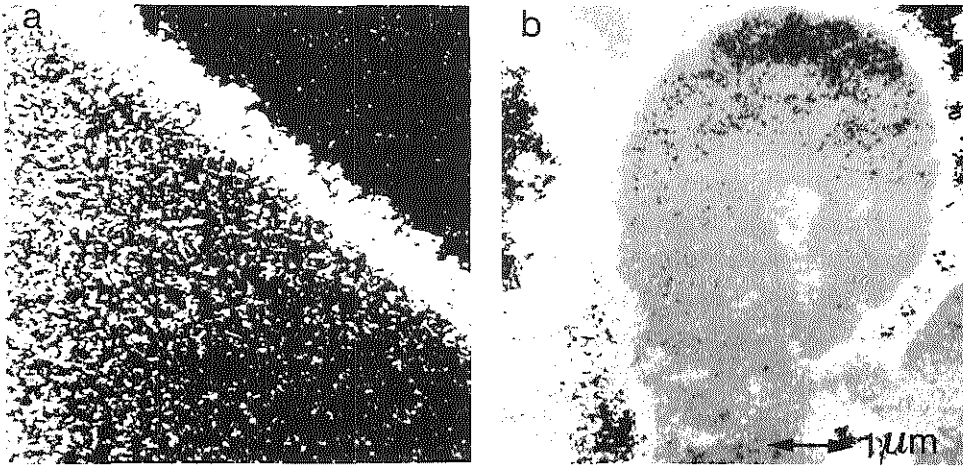


**Figure 7.5.** Element-concentration distribution images as obtained by dividing an iron net-intensity image by the zero-loss image. (a) Rim of a Fe-Bio-standard. (b) Siderosome. The different grey shades represent different iron-concentrations (darkgrey > lightgrey > white). The black spots at the periphery of the image is the non-iron containing background. The ferritin-cores (white) surrounding the siderosome have approximately the same iron-concentration as the Bio-standard.

## DISCUSSION

From these experiments it is concluded:

- 1 In QSA several methods may be used to detect the ionisation edge objectively. There was no difference in performance between the three implemented methods. We used the noise dependent method (1) to determine  $E_{IE}$  and obtained a reproducibility of 4 eV and an accuracy of 1.4 eV, with the usual zero-calibration. The method for calibrating the energy scale (at the zero-loss position) may be replaced by a calibration procedure relative to the carbon edge. Although for C→Fe-calibration, the reproducibility was not improved (3.5 eV), the accuracy was slightly better (0.6 eV) and more importantly this method allows intermediate calibration without an intensity overflow of the photomultiplier (PMT). The drift calculated over time is negative, in absolute value not exceeding 0.1 eV/min, which is within the specifications of the Zeiss microscope (0.2 eV/min).

Calculation	Object	Area ( $\mu\text{m}^2$ )			
		I black	II white	III lightgrey	IV darkgrey
<u>Nett(718 eV)</u>	Siderosome	16.3	61.4	22.2	0.1
Z.L.	Bio-standard	90.7	8.7	0.4	0.2
<u>Nett(738 eV)</u>	Siderosome	11.1	40.4	46.2	2.3
Z.L.	Bio-standard	69.9	27.6	1.9	0.6
<u>Nett(718 eV) + Nett(738 eV)</u>	Siderosome	8.9	37.4	49.2	4.5
Z.L. + L.L.	Bio-standard	74.8	23.2	1.4	0.6

**Table 7.2.** Area-fractions of increasing iron-concentrations I-IV using the two IE-images separately and combined. Nett: nett iron-distribution image; Z.L.: zero-loss image (0 eV); L.L.: low-loss image (20 eV).

•2 From an analysis of the spectra, varying the  $\Delta$ -range in position and width, with a constant  $\Gamma$ -region of 50 eV, we can conclude that a constant  $S_{R_x}$  value (within 10%) is obtained for  $W_{\Delta} \geq 15$  eV at  $E_{\Delta} \geq E_{IE} + 10$  eV. The 10 eV region beyond the  $E_{IE}$  may be used as a guard region because it eliminates the influence of the white lines and the ionisation edge variation and drift. It is to be expected that other edge-types (delayed-, H-type) have different optima.

The QSA-experiments suggest that for the acquisition of images, slits must be positioned 10 to 20 eV beyond  $E_{IE}$ , with a slit width  $\geq 15$  eV. Under such conditions relatively stable  $I_{R_x}$ -values may be obtained. Assuming the same behaviour for images, the ionization-edge image should be recorded 10 eV or more from the actual ionization-edge.

•3 In QIA, element-related images can be co-localized with structure-related images from the same area. It has been shown that the morphometric parameters (area, perimeter, etc) can be determined objectively and reproducibly in QIA [Chapter 5-6; Zondervan *et al.* (1989); Ringeling *et al.* (1991)]. For concentration measurements in images several problems still have to be solved. Among these are the correct determination of  $I_{R_x}$  and  $I_{R_x}^*$ , as equivalents of the  $S_{R_x}$  and  $S_{R_x}^*$  in

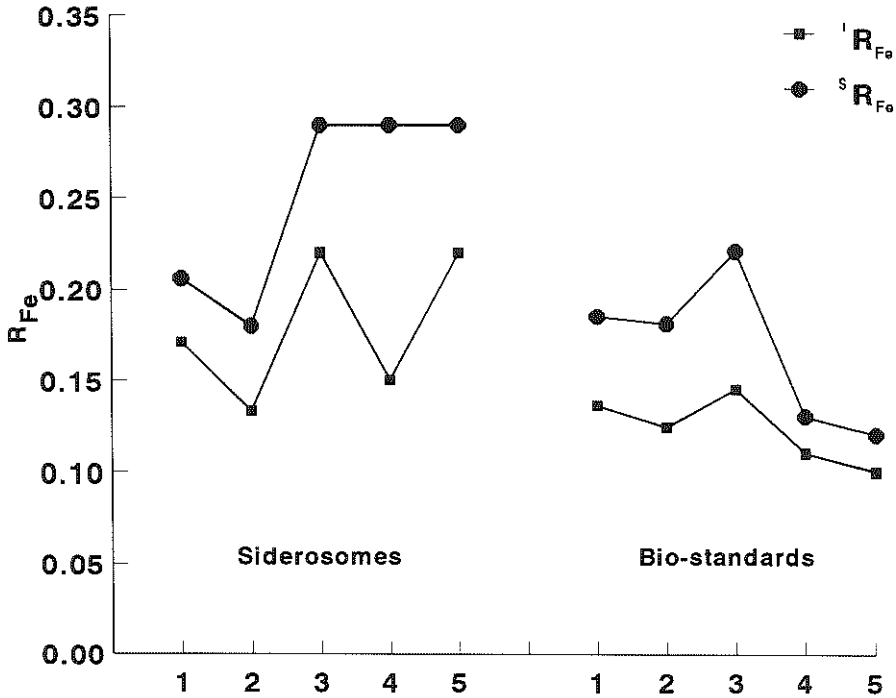


Figure 7.6, Spectral relative concentrations ( $^S R_{Fe}$ ) compared to the ones obtained with images ( $^I R_{Fe}$ ) of 5 Bio-standards and 5 siderosomes in liver parenchymal cells.

QSA, respectively.

To extrapolate the continuum and obtain the background-image beyond the ionization-edge, the power-law model is to be preferred over the PIE- and linear extrapolation methods, considering that the power law function is generally accepted as a good model for the background-fit. However, another possible method [Trebbia and Bonnet (1990); Trebbia and Mory (1990)] will be investigated in the next chapter.

•4 The determination of  $^I R_x^*$  has been a problem until now. The optical filter which has been inserted allows to record images in the element-specific region and the zero-loss region under the same instrumental conditions. This makes it possible to obtain  $^I R_x^*$  with images by using eq. 7.2. The validity of the application of eq. 7.2 is based on the assumption that  $t_{st} = t_{sid}$ ,  $\sigma_{st} = \sigma_{sid}$  and that there is a linear relationship between concentration and  $R_x^*$ .

The presence of an outer rim in the Bio-standard with a slightly different iron concentration as shown in Fig. 7.5 is not a common observation in cross-sectioned Bio-standard beads in ultrathin sections. In most cases the more homogeneous central parts of the beads are used. Because of the inter- and intra-bead concentration variations, detected before by using spectra, a mean iron concentration value from several such bead images has to be obtained for a more reliable estimation of the iron concentration in the unknown siderosome.

More than one IE-image may be used for concentration measurements. However at the cost of different results. Great care must be taken in thresholding the different concentrations. A standard procedure must be maintained to allow combination of the information as obtained from several objects.

•5 The differences in Fig. 7.6 between the mean values of  $I_{R_{Fe}}$  and  $S_{R_{Fe}}$  from the siderosomes can partially be explained by the differences in electron detectors for image and spectral analysis. Also the projected circular spot from the analyzed area is completely recorded through the PMT entrance diaphragm, while the TV camera's light optical (post) magnification makes that only a part of this spot is recorded. This may introduce a difference in analyzed area. Also the positions may not have been exactly the same because of instrumental drift. In the acquisition protocol used, first all the images were recorded at the ten positions and next the spectra were recorded at approximately the same positions. Further investigations have to be performed to determine optimal conditions to be able to compare  $I_{R_x}$  to  $S_{R_x}$ .



---

# **CHAPTER 8**

**IMAGE ANALYSIS 4  
THE USE OF MULTIVARIATE STATISTICAL  
ANALYSIS FOR QUANTIFICATION OF EELS-IMAGES**

CHAPTER 8

IMAGE ANALYSIS 4

Multivariate statistics as a tool for element analysis.

This chapter has been submitted to *Journal of Cellbiology*

*Multivariate Statistical Analysis as a tool for element quantification*

Sorber C.W.J., Bonnet N., Trebbia P., Gelsema E.S., Jongkind J.F., Beckers A.L.D. and De Bruijn W.C.

SUMMARY

In order to obtain information about the accuracy of the analysis of EELS-images, multivariate statistical analysis (MSA) is used as a tool to investigate the various effects which in combination are responsible for the image-formation. Sets of energy-loss related TEM-images, recorded with the Zeiss EM902, were analyzed with multivariate statistical and conventional methods (power-law model).

MSA is a very sensitive method which makes separation of the different sources of information in a set of images possible. Only when two or more different effects happen in exactly the same images, the effects cannot be clearly separated. Shading-correction is not necessary since this is accounted for in the average grey-value profile. Reduction of the number of images does not have a relevant influence on the siderosome area. Side-effects such as thin spots in the EPON which appeared on the first factorial axis in the analyzed set have less influence in reduced sets. Therefore, a reduction of the number of images to six is recommended, to be able to read the different sources of information from the factorial axes. This made analysis of calcium images possible while using four images in the IE-region and only two image in the PIE-region.

---

## INTRODUCTION

The aim of the analysis of EEL-spectra and images is to separate the element-specific excitation signal  $I_{K, L, M}$ , at a specific energy-loss  $E$ , from the non-specific continuum-information  $I_B$ , on which the characteristic excitation signal is superimposed (chapter 1, Fig. 1.5). Therefore, spectral data and images taken in front of the element-specific energy-loss, are analyzed in order to find a mathematical expression that gives a good description of the continuum in that region, in order to allow extrapolation beyond the edge. A power-law relation is considered to be valid in the region in front of the edge. For certain spectral regions, however, it is known that such a generalized expression will not lead to an appropriate fit [Sorber *et al.* (1991a)]. In some cases, due to the co-occurrence of edges, only short regions are available for the analysis. Especially for image-analysis this may hamper the application of a sound procedure for continuum-estimation. The limited number of images in front of the ionization edge, the influence of plasmons in that region, the steepness of the slope of the continuum and moreover the noise will make the analysis difficult both for spectra and for images [Egerton (1986), Bonnet *et al.* (1988), Trebbia & Bonnet (1990), Sorber *et al.* (1990a, 1990b)]. In this chapter we will concentrate on image-analysis. The proposed fitting and extrapolation procedures have to be applied to each of the  $512^2$  pixels, in a set of corresponding images reflecting the spectral information (see Figs. 7.2 and 7.4).

In the case of  $f(E)=A.E^{-r}$ , the parameters  $A$  and  $r$  are not the same for the entire image due to mass-thickness fluctuations. Both parameters must therefore be calculated for each pixel separately.

However, this parametrical procedure has some limitations [Hannequin & Bonnet (1988)]:

- Even though  $A$  and  $r$  are calculated for each pixel separately, this does not solve all problems related to mass-thickness fluctuations. With thick specimens e.g., multiple scattering results in a convolution of the information from the characteristic energy-loss and multiple plasmon energy-losses. Since correct deconvolution is not possible with restricted data available along the energy-loss scale, great care must be taken in interpreting the results obtained by a procedure which neglects this aspect.
- The choice of an "a priori" model (power-law) for the extrapolation to the background image under the ionization edge image may introduce a systematic bias

in the results when few images are used for the estimation of the parameters of the model.

In order to find a solution to the problem of extracting the  $I_{K, L, M}$ -image information, Hannequin and Bonnet [Hannequin & Bonnet (1988); Bonnet & Hannequin (1989)] were among the first to apply MSA to images recorded with a STEM in order to acquire the element related net-intensity image. This was further examined by Trebbia & Bonnet (1990) and Trebbia & Mory (1990). In a similar way, sets of TEM-images, recorded with the Zeiss EM902 were analyzed using MSA. The results were compared to conventional procedures, based on a power-law model.

Multivariate Statistical Analysis is a non-parametric procedure to separate the significant element-related information from the redundant information (continuum). The contribution of each of the eigenfunctions to the original images may be calculated. It is a statistical analytical procedure, looking at different effects that co-occur in a data-set. This is modelled as an eigenvalue-problem, which allows the separation of these different sources of information mixed in each image of the original data-set. These different sources of information appear in the calculations as eigenvalues. Once the different information sources are extracted from the set of composed images, each image in the original data-set may be reconstructed while discarding some of the eigenfunctions. This makes it possible to filter and interpolate (or extrapolate) the data [Hannequin & Bonnet (1988); Bonnet & Hannequin (1989); Trebbia & Bonnet (1990); Trebbia & Mory (1990), Bonnet & Trebbia (1993); Gelsema *et al.* (1982, 1992a, 1992b);]. In this chapter the identification of the factorial axis (eigenvector) which contains the element-information will be the main goal of the analysis presented here.

As compared to the conventional procedure, MSA has one fundamental limitation. The ability of the method to detect an element in the images depends on the presence of at least two different sets of pixels which react differently in the set of images, in this case pixels containing element-information and pixels containing only background information. If the element covers the whole image, all pixels will correspond in the same way both in front of and beyond the edge and MSA will not detect the element [Gelsema *et al.* (1992a, 1992b)].

Several parameters for the analysis of the data with MSA will be varied in order to test their influence on the final results. These parameters include the application of shading-correction and the number of images to be analyzed.

---

*Multivariate Statistical Analysis (MSA)*

The goal of MSA in this application is to extract the significant information contained in a dataset of  $N \times P$  greyvalues (where  $P$  is the number of pixels per image and  $N$  is the number of images). For this purpose a contingency-table of greyvalues is formed containing  $N$  rows and  $P$  columns. The formalism then calculates an "average greyvalue profile" onto which possible effects are superimposed as orthogonal modulations. Processes that affect each of the acquired images in the same way, such as the gradual decrease in continuum intensity, shading and influences of inhomogeneous specimen thickness are accounted for in this "average greyvalue profile" [Gelsema *et al.* (1992a, 1992b)]. However, image-components that are not the same in all the images such as noise, acquisition artifacts and more importantly the contribution of the chemical elements of which the features are included in the analyzed set of images, may be separated from this "average greyvalue profile".

A new  $Q$ -dimensional space ( $Q \leq N-1$ ) can be defined in which the factorial axes are representatives of the "effects" which cause each individual profile to deviate from the "average greyvalue profile". If two or more of such effects are independent, in the sense that they manifest themselves in different images and/or in different regions of the images, these effects will be represented on different factorial axes. These factorial axes are the eigenvectors of a symmetric matrix which can be composed from the original data matrix. The factorial axes are computed as the directions of maximum projected variance under the constraint of mutual orthogonality.

In principle, each original image gives a contribution to each of the factorial axes. Conversely, each original image may be exactly reconstructed as a weighted sum of the factorial contributions, superimposed on the "average greyvalue profile" of the data-set. Once the factorial axis which results from the presence of the element has been identified, its contribution to the post-edge image(s) may be calculated. This factorial contribution shows the pixels in the image-set that contributed to this factorial axis, i.e. the pixels with element content. This results in an image with a bimodal intensity histogram: one peak for the non-element pixels and one peak for the element pixels. According to this histogram the image may be segmented, thus immediately yielding the chemical element-map.

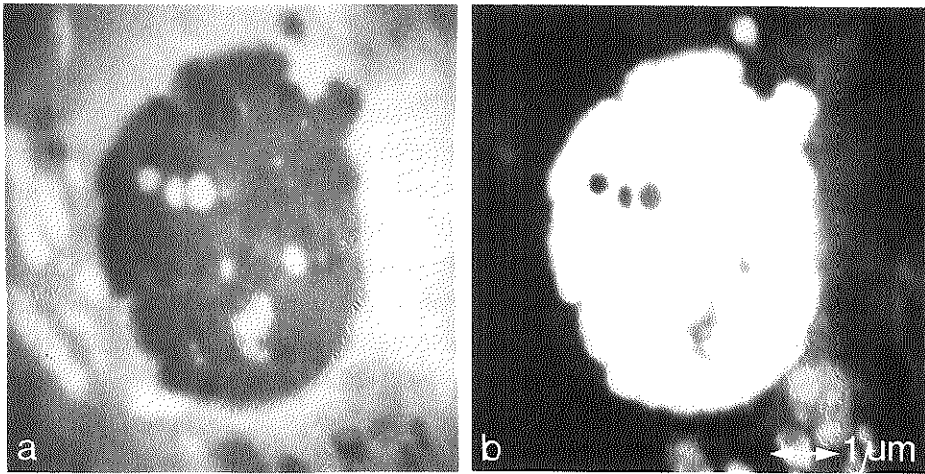


**Figure 8.1.** (a) Zero-loss image of a siderosome. The light features to the left of the siderosome are thin spots in the embedding material. (b) Contrast-sensitive darkfield-image of the same siderosome recorded just in front of the carbon-edge (250 eV).

## MATERIALS AND METHODS

### *Experiments*

Unstained ultrathin sections from aldehyde-fixed liver tissue from patients with an established haemochromatosis, were co-embedded with Fe-Bio-standards.

For the experiments sets of images were recorded and analyzed. The sets included structure-sensitive images acquired at  $\Delta E=0$  eV and  $\Delta E=250$  eV. The protocol for the recording of the images has been described in chapter 2. During recording of the images, the camera-gain, KV and black-level was locked on the intensity of the first energy-loss image. Each image was stored on disk, directly after its acquisition.

The processing of the recorded images was done on a Compaq deskpro 386/25 and a Commodore 386-SX with the programmes CARTO for conventional processing [Bonnet *et al.* (1988)] and AFC2 for multivariate statistics processing [Hannequin & Bonnet (1988); Bonnet & Hannequin (1989); Trebbia & Bonnet (1990); Trebbia & Mory (1990)]. In the latter case, the maximum number of factorial axes that can be calculated is equal to  $N-1$ , where  $N$  is the number of images being analyzed. Usually the main information is visible on the first factorial

axis, the higher factorial axes containing information from other sources.

Each of the original images may be projected onto any of the factorial axes. Projection onto the axis resulting from the presence of the element to be detected will show a clear separation of the pre-edge and the post-edge images. Such projections may therefore serve to identify the "element axis". Projection onto the other factorial axes will not show such a difference.

The following experiments were performed:

- 1 A set of 16 images of a siderosome was recorded from 605 eV to 755 eV with a slit-width of 10 eV at a magnification of 7,000x. Images 1-10 (605-695 eV) were in the pre-ionization-edge region, images 11-16 (705-755 eV) were in the ionization-edge region. In addition, for the purpose of shading-correction, at each energy-loss an out-of-focus image of the EPON was recorded.
- 2 The number of images of set •1 was reduced to test the influence of the number of images used in the analysis on the results.
- 3 Other subsets of set •1 were analyzed using only one ionization edge image (image 12). These sets were analyzed both with MSA and the power-law method.
- 4 Additionally acquired sets with a 30,000x magnification of another siderosome are used to demonstrate some acquisition artifacts that were encountered.
- 5 After analysis of the previous sets, a set of six calcium images was acquired at a magnification of 12,000x. Two images were acquired in front of the calcium ionization-edge, making sure that the carbon K-edge was not included, and four images were acquired beyond the edge.

## RESULTS

The zero-loss image of the image-set of the first three experiments is shown in Fig. 8.1a and the contrast-sensitive dark-field image (250 eV) is shown in Fig. 8.1b.

- 1 In Fig. 8.2a-f, the projections on the first three factorial axes for the original set (a, c, e) and for the shading-corrected set (b, d, f) are plotted as a function of the energy-loss at which the images were recorded. Likewise, pixel profiles may be projected onto any of the factorial axes, the projections being rearranged as so called factorial projection-images (Fig. 8.3a-f). Both without and with shading correction, the element information (iron in the siderosome) was visible on the first factorial axis (Fig. 8.2a-b, 8.3a-b).

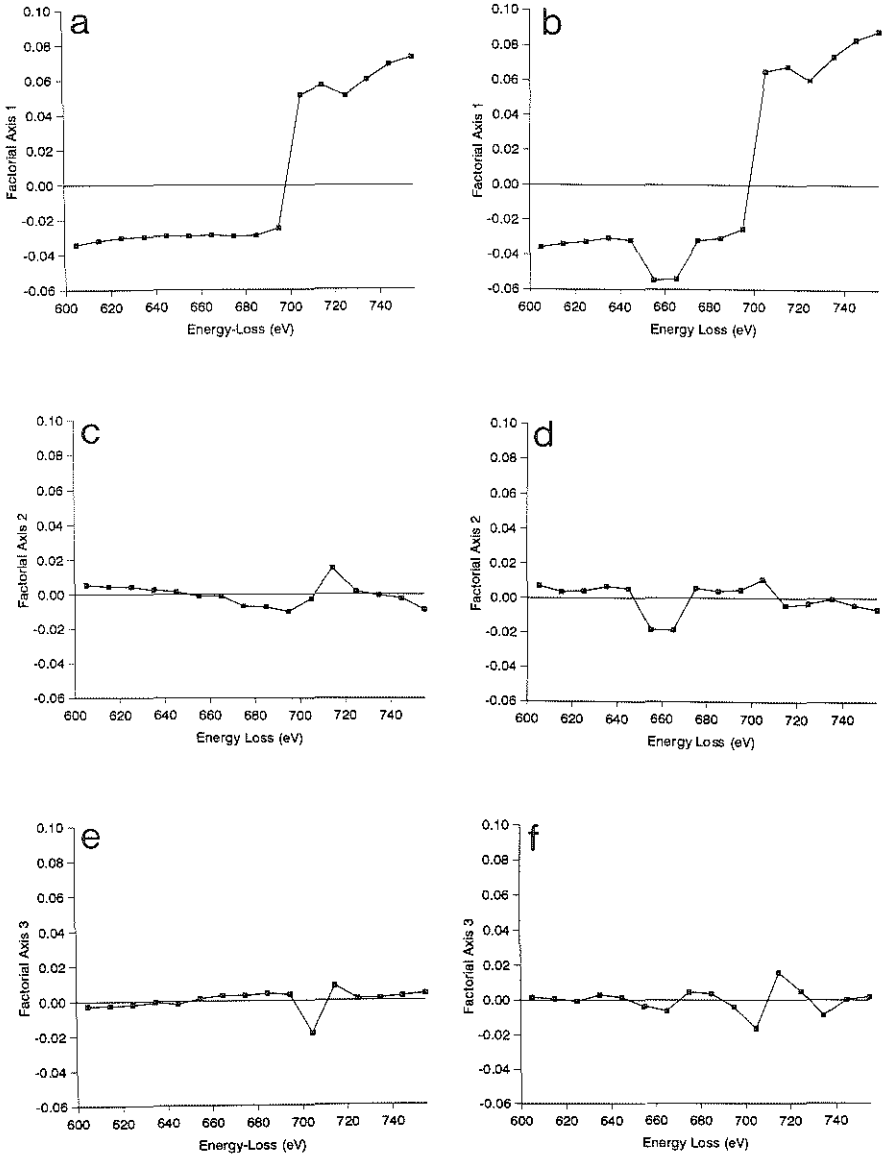


**Figure 8.2,** Projections onto the first three calculated axes of the image-set, before (a,c,e) and after (b,d,f) shading correction, plotted versus energy-loss of the images. The element-information is visible on the first axes as a steep rise in the projection between 680-710 eV.

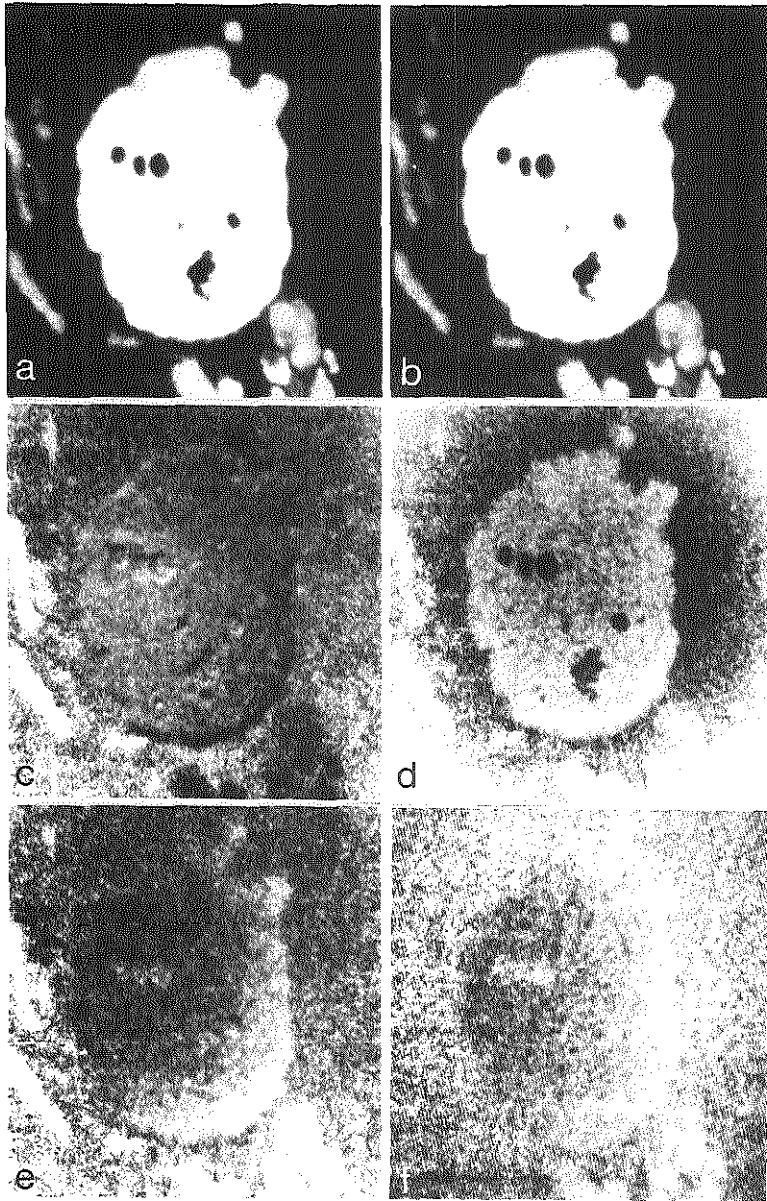


**Figure 8.3,** The first three factorial projection-images of the original set (a, c, e) and the shading-corrected set (b, d, f). The element-information is considered to be visible in the projection-image of the first factorial axes (a, b). The second factorial projection-image of the shading-corrected set shows a halo (d). In the third factorial projection-image of the shading-corrected set a frequency-pattern is observed (f).

## Chapter 8

In the cytoplasm other iron-containing features are observed. The higher factorial axes are considered to represent effects from other sources (Fig. 8.2c-f, 8.3c-f). In the second factorial projection-image of the shading-corrected set a kind of halo around the centre can be seen (Fig. 8.3d). This may be caused by the shading-correction, which may have been too strong. The third factorial projection-image of the shading-corrected set shows an interference-pattern. After closer examination of the acquisition chain the camera light controller was found to produce a line that moved over the image with a certain frequency during the acquisition of the images. The shading-correction resulted in an interference-pattern of the image of the siderosome and the out-of-focus EPON image.

After MSA-analysis, the first factorial projection-image was used as an element-distribution image, from which the area of the siderosome and the total element area were obtained.

To obtain binary images the value zero was used as a separator. In Fig. 8.4 an example is given of a greyvalue-histogram of the projection image containing the iron-information (Fig. 8.4a) and of a net-iron distribution image as obtained with the power-law method (Fig. 8.4b). The pixels left of the zero-line in Fig. 8.4a are black in the projection-image and the pixels right of the zero-line are white in the binary image (Fig. 8.3a).

Images	Figure	Shading Corr.	N	Variance (%)			Area ( $\mu\text{m}^2$ )	
				FA 1	FA 2	FA 3-15	Sid.	Total
1-16	8.2-3 a, c, e; 8.5a	No	16	87	2	11	9.50	11.02
1-16	8.2-3 b, d, f; 8.5a	Yes	16	87	2	11	9.73	10.77

**Table 8.1.** The areas and variance percentages of the experiments comparing the original set and the shading-corrected set. Images 1-10 are in the PIE-region and image 11-16 are in the IE-region. N is the number of analyzed images, FA is factorial axis, SD is the standard deviation.

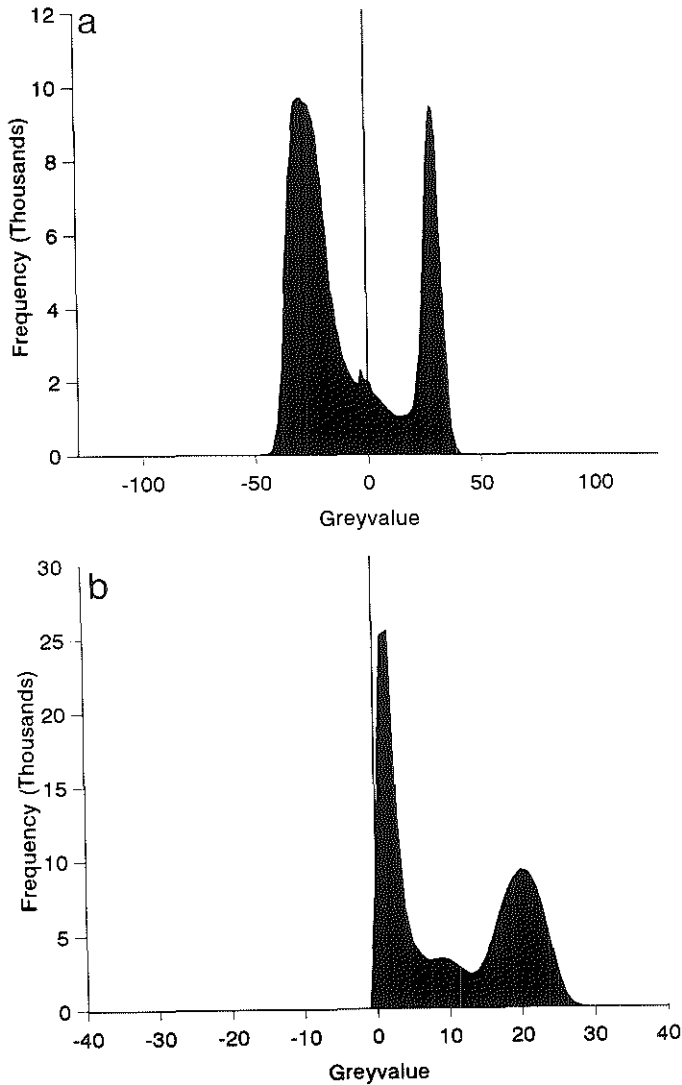


**Figure 8.4,** Greyvalue frequency histograms of a factorial projection image containing the iron information (a) and of the net iron-distribution image as obtained with the power-law method (b). In the factorial projection image, 0 is used for separation of the pixels contributing to the factorial axis and the non-contributing pixels. In the net iron-distribution image, separation of the distributions was performed as described in chapter 5.

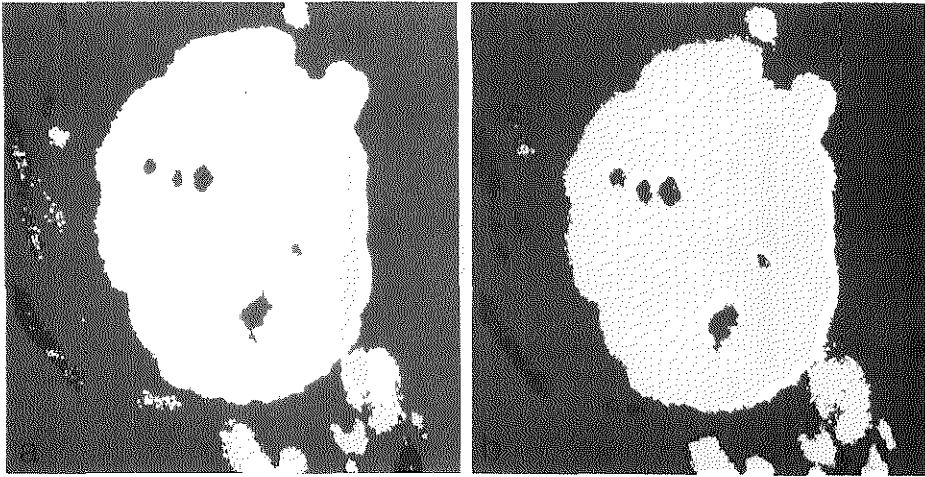


**Figure 8.5,** (a) Superposition of the projection-images onto the first factorial axis of Fig. 8.3. The original set (Fig. 8.3a) is shown as black and the shading-corrected set (Fig. 8.3b) is shown as white. The overlap after superposition is grey. (b) Superposition of the projection-image onto the first factorial axis of the image-set containing images 1-10 and 12 (shown as black) and the element net-distribution image of the power-law method (shown as black). The overlap after superposition is grey.

The influence of the shading-correction is first considered. The binary first factorial projection-images of the original set (black, Fig. 8.3a) and of the shading-corrected set (white, Fig. 8.3b) are combined in Fig. 8.5a. The overlap of the two images is displayed in darkgrey. The area of the siderosome is somewhat larger after application of shading-correction. In the areas occupied by the small features around the siderosome, small differences can be seen especially at the periphery of the image.

In our experiments, when higher instrumental magnifications are used, the shading-component of the images plays a more important role (Fig. 8.6). As a consequence, the first factorial axis may contain this shading information (Fig. 8.6a), while the element-information has moved to the second factorial axis (Fig. 8.6b).

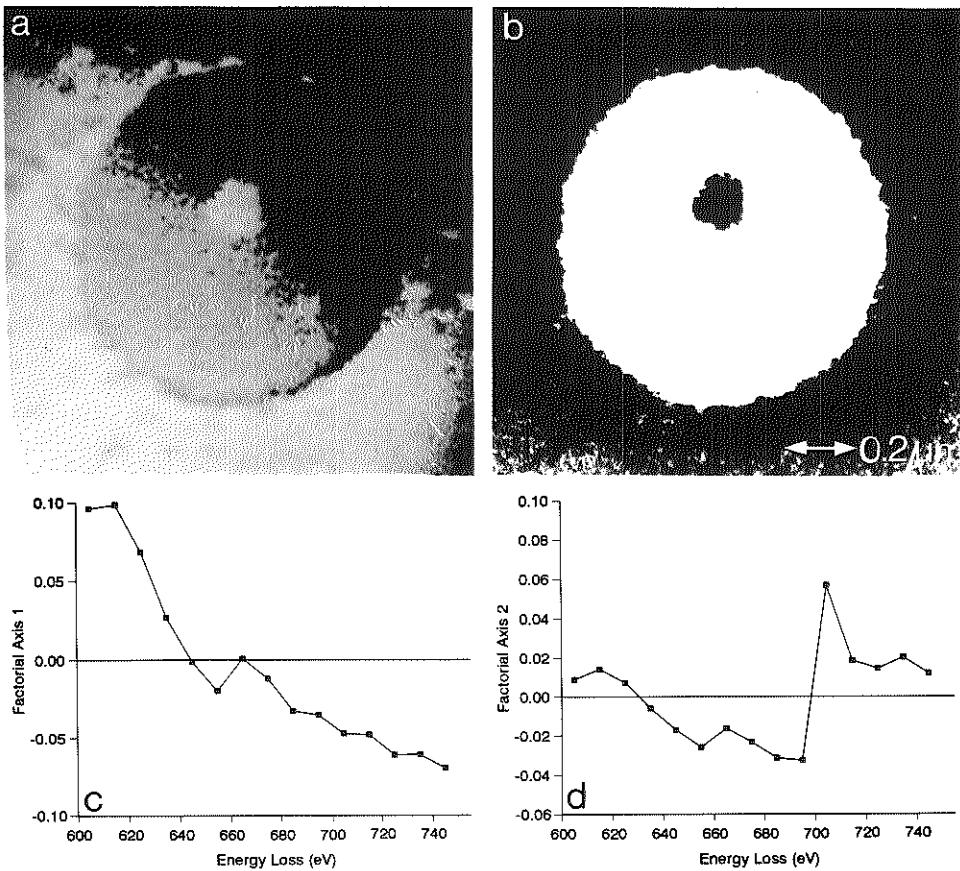


**Figure 8.6.** The influence of shading at higher magnifications (30,000x). The shading-effect is visible on the first factorial axis and the element-information on the second factorial axis.

The results of the morphometric analysis of these sets of images are shown in Table 8.1. Only the percentages of variance of the first two factorial axes are shown. The higher factorial axes of the data-set have only a very small contribution to the image-set (11% divided over 13 factorial axes). The siderosome area is slightly larger after application of a shading-correction.

In the following experiments, the original set without shading-correction will be used.

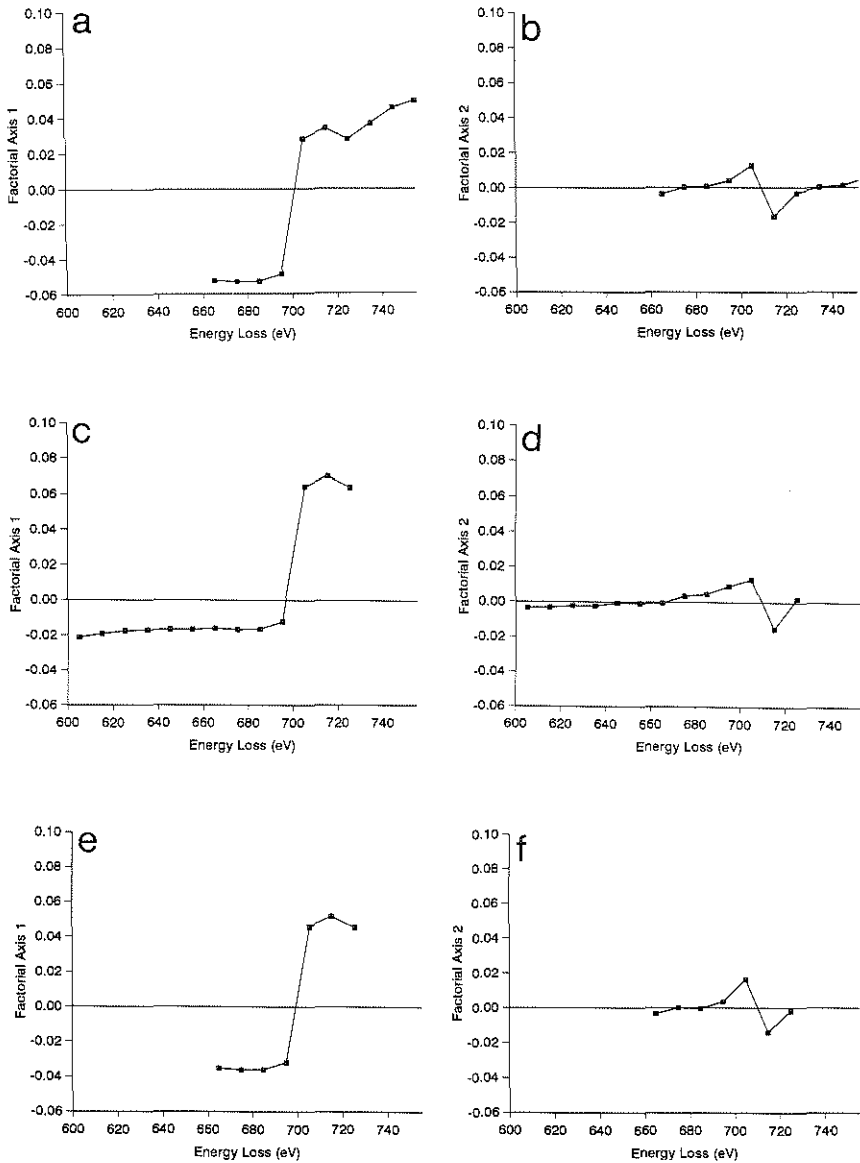


**Figure 8.7,** The influence of reduction in the number of analyzed images of Fig. 8.2. Factorial axes 1 (lefthand side) and axes 2 (righthand side) are shown; a-b, when images 7-16 are used ( $N=10$ ); c-d, when images 1-13 are used ( $N=13$ ); e-f, when images 7-13 are used ( $N=7$ ).

Images	Figure	$\Gamma/\Delta$ (eV)	N	Variance (%)			Area ( $\mu\text{m}^2$ )	
				FA 1	FA 2	FA $\geq 3$	Siderosome	Total
1-16	8.2-8.3	100/60	16	87	2	11	9.50	11.02
1-15		100/50	15	87	2	11	9.45	10.78
1-14		100/40	14	84	2	14	9.54	10.95
1-13		8.7a,b	100/30	13	83	3	14	9.56
4-16	8.7c,d	70/60	13	88	2	10	9.45	10.71
6-16		50/60	11	88	2	10	9.46	10.64
7-16		40/60	10	88	2	10	9.46	10.60
8-16		30/60	9	86	3	11	9.52	10.67
9-16		20/60	8	80	5	15	9.47	10.63
10-16		10/60	7	79	6	15	9.47	10.63
7-13		8.7e,f, 8.8b	40/30	7	88	4	8	9.46
8-13	30/30		6	82	11	7	9.54	10.93
9-12	20/20		4	78	14	8	9.51	10.69
10-11	10/10		2	100	-	-	9.55	10.84

**Table 8.2.** The areas and variance percentages of the experiments with reduction of the number of images to be analyzed. Images 1-10 are in the PIE-region and images 11-16 are in the IE-region. N is the number of analyzed images, FA is factorial axis, SD is the standard deviation.

•2 Subsets of the original set described above were analyzed by reducing the number of images to be analyzed. The results are shown in Table 8.2 and Fig. 8.7. When the number of images to be analyzed is reduced, the detected areas do not differ significantly ( $\leq 1\%$ ). The variance explained by the factorial axes of Fig. 8.7 and the measured areas of the siderosome are shown in Table 8.2. In the case of fewer images beyond the edge, the variance on the first factorial axis is quite stable. When the number of images in the pre-edge region is reduced, the variance is only decreased when fewer than three images remain. The area of the siderosome is approximately the same as for the complete set. When both in front of and beyond the edge the number of images is reduced no relevant changes are observed in the siderosome area. Evidently when only two images are used, all variance is explained by the first factorial axis and there is no way to separate different effects.

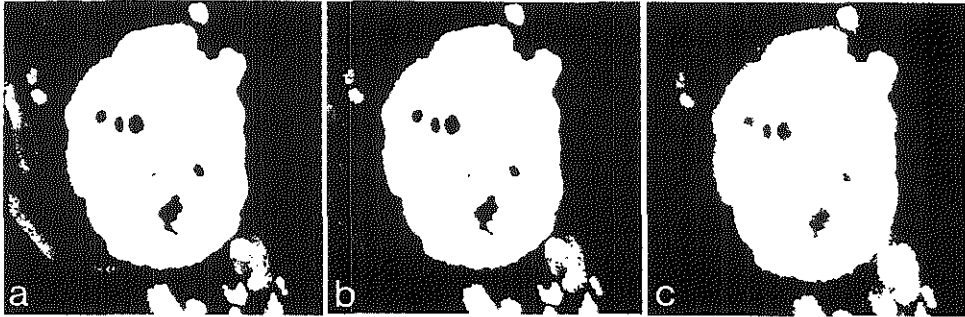


**Figure 8.8.** (a) Binary projection-image of the first factorial axis of the original set (N=16). (b) Binary projection-image of the first factorial axis of the set containing images 7-13 (N=7). (c) Binary net-intensity element-distribution image of the power-law model.

\*3 Another subset containing images 1-10 and 12 was analyzed both with MSA and conventional methods (power-law model). The number of images to be analyzed was also varied in this subset. The Fe-containing areas were calculated and compared. In Fig. 8.8c the binary resultant image of the power-law method is displayed. The grey-value histogram of the enhanced resultant images of the power-law shows three peaks (Fig. 8.4b). The last two peaks, corresponding to two different elemental concentrations, are used for the element area calculations. The first peak contains the background-pixels. The results are shown in Table 8.3.

Reduction of the number of images or analyzing the even or uneven numbered images does not change the results significantly. However when only five PIE-images are used, the siderosome area is reduced when using MSA. Furthermore the power-law analysis yields an increased siderosome area as compared to MSA and its results are more stable.

The areas of the resultant images of the set containing images 1-10 and 12 of the first projected factorial axis (black) and the power-law model (white) are compared in Fig. 8.5b. The overlap of the two images is displayed in grey. The areas of the power-law model are slightly larger than the ones of the MSA-method.

PIE- images	$\Gamma$ (eV)	N	Variance (%)			Area ( $\mu\text{m}^2$ )			
			FA 1	FA 2	FA $\geq 3$	Siderosome		Total	
						MSA	Power law	MSA	Power law
1-10	100	11	74	5	21	9.60	9.86	11.50	11.35
1-10 odd	100	6	87	5	8	9.59	9.86	11.46	11.38
1-10 even	100	6	88	4	8	9.59	9.86	11.46	11.35
4-10	70	8	76	7	16	9.61	9.87	11.40	11.37
7-10	40	5	88	4	8	9.54	9.87	11.15	11.00

**Table 8.3.** The areas and variance percentages of the sets of images analyzed with both MSA and the power-law method. Only one IE-image is used (image 12) while the number of images in the PIE-region (images 1-10) is varied. N is the number of analyzed images, FA is factorial axis, SD is the standard deviation.

•1-3 Some of the image sequences in •1, •2, •3 showed some features at the periphery of the image. Comparison with the zero-loss image and the contrast-sensitive darkfield images showed that these features were thin spots in the embedding material. These thin spots do not show up when the power-law method is used (Fig. 8.8c). Reduction of the number of images to be analyzed also reduces the effect in the thin spots (Fig. 8.8b).

The projection image of the first factorial axis of the original set shows a combination of the iron information and the effect that takes place in the thin spots. The projection image of the second factorial axis (Fig. 8.3b) shows the thin spots almost solitary. However, note that the effect on the second axis, which happens only in the thin spots, happens at almost the same energy-losses as the element-effect takes place on the first factorial axis. This may be the reason why they are not completely separated on the first axis.

•4 Some influences of the acquisition procedures which were not directly visible in the recorded sets of images, remained undetected with the conventional methods. In Fig. 8.9, a combination of the first two factorial axes is shown of an experiment in which 5 images were recorded in one run before storage to disk to reduce the acquisition time. The radiation damage during the time of storage had proceeded such that this was recorded as a deviation from the average grey-value profile.

## Chapter 8

---

Three groups of 5 points can clearly be separated in the figure. In the experiments in this chapter each image was stored on disk immediately after its acquisition to keep the influence of the radiation-damage constant. The radiation damage is then accounted for in the average grey-value profile.

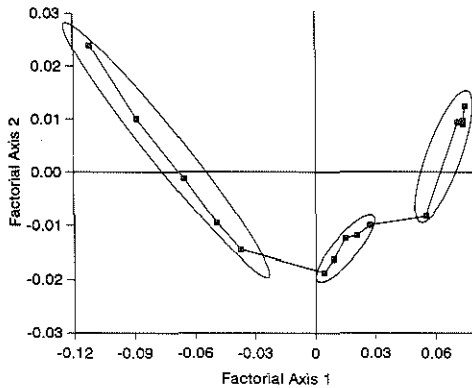


**Figure 8.9,**  
Combination of the first two factorial axes of a set of 15 images. The images were recorded in sets of 5 before storage on disk. Three groups of data-points are observed due to the influence of radiation damage during storage time.

•5 The first two factorial axes of the calcium experiment are shown in Fig. 8.10 a-b. The first factorial projection-image shows a perfect calcium-distribution (Fig. 8.10c) while the second factorial projection-image (Fig. 8.10d) shows noise. The variance percentage of the element-axis was only 60% which is less than with the iron images but the number of pixels contributing to this axis were far less than with the iron experiments. For comparison, the zero-loss image and the contrast-sensitive darkfield-image at 250 eV are shown in Fig. 8.10e and Fig. 8.10f respectively.

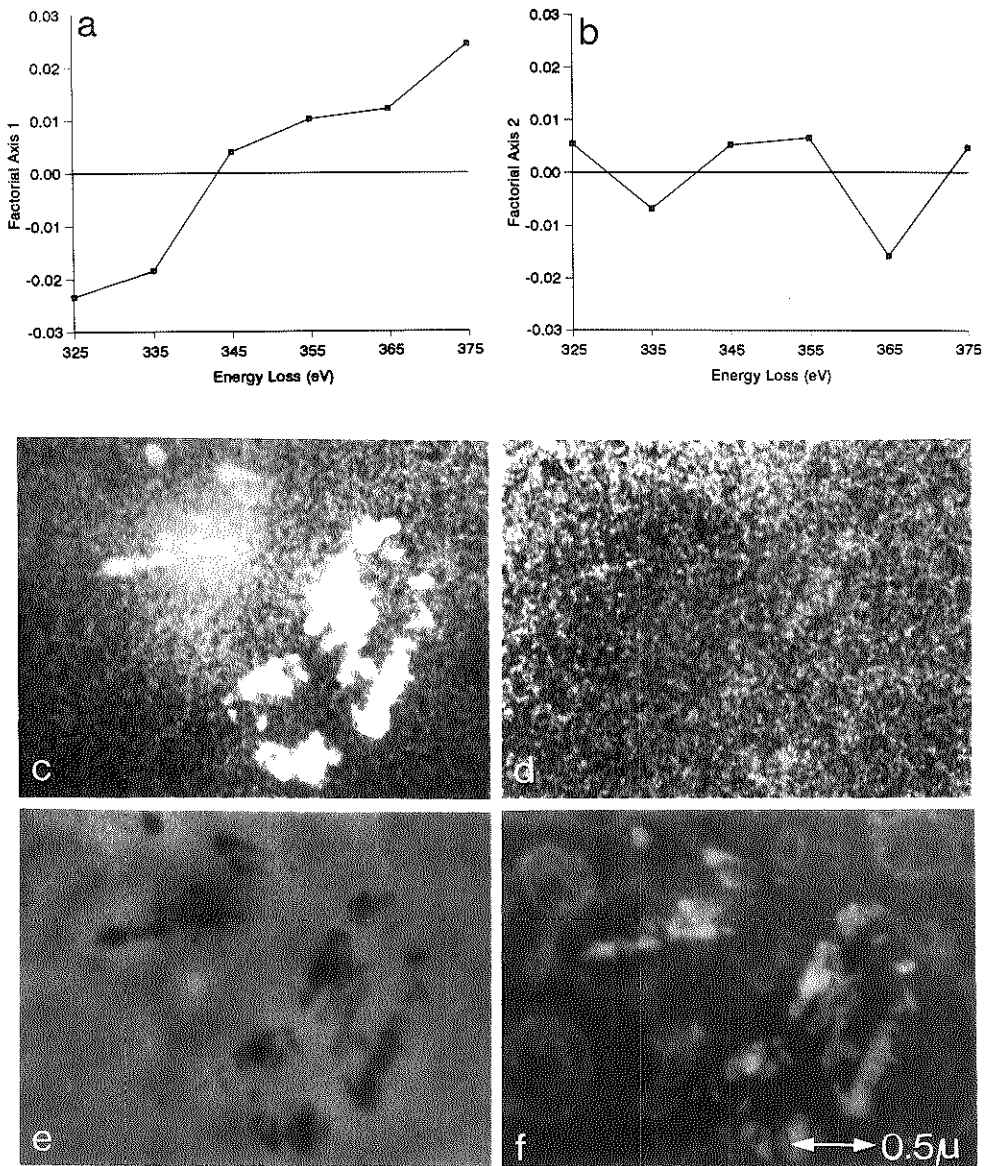


**Figure 8.10,** Projections of the image-profiles onto factorial axis 1 (a) and 2 (b) and the projections of the pixel sequences on both axes (c and d respectively) of the calcium-experiment. For comparison the zero-loss image (e) and the contrast-sensitive darkfield image (f) are also shown. Only six images were used, two in front of the calcium-edge and four beyond the edge. The calcium-distribution is clearly visible in the first factorial projection-image (a).

### DISCUSSION

From the experiments we may conclude that MSA is a very sensitive procedure which allows us to separate different sources of information in a set of images. After separation of these sources the individual information-streams have to be interpreted to allow the information of interest to be extracted.

The aim of a correct acquisition-procedure is to show the chemical element information as the main source of information. The remainder of the information-streams such as noise, visible on the higher factorial axes, can then be disregarded.

MSA was able to clearly separate all the different information-streams and reveal their influence on the images. Projection of the pixel sequences onto the factorial axis with the element information, provided the net element-distribution image.

•1 After application of shading-correction, it was observed that the calculated siderosome-area of the shading-corrected set is slightly larger than that of the original set but this increase is only small. Some features at the periphery of the image do not show up in the shading-corrected set. Because of the halo of the second projection-image we may assume that the shading-correction has been too strong. This might also lead to an increase in the detected siderosome area because the periphery of the siderosome is also visible in this second projection-image. A shading-correction should not be necessary since this is accounted for in the average greyvalue profile and it may introduce other effects on the factorial axes (Fig. 8.3d). However, there are indications that when higher instrumental magnifications are used, the shading-component of the images plays a more important role (Fig. 8.6). As a consequence, the first factorial axis may contain this shading information (Fig. 8.6a), while the element-information is recorded on the second factorial axis (Fig. 8.6b). But even then shading-correction is not necessary because the second factorial axis can now be used for quantification.

•2 Reduction of the number of images to be analyzed does not have a significant influence on the results. The calculated areas of the siderosome are quite stable both for MSA and the power-law model. This makes a reduction of the number of images possible which will make the acquisition and processing time shorter and hence reduce the influence of radiation damage.

•3 From the comparison of MSA of the original set with the conventional method we may conclude that the power-law model gives a slightly higher area-fraction, especially at the borders of the features. This may be due to the fact that the segmentation of the conventional logarithmical procedure was based on the cross-overs of the three visible contributions (Fig. 8.4b), and the calculated siderosome areas were based on the two element peaks, while during MSA analysis only part of the middle contribution, which was divided by the zero-line, was used. The duration of the analysis is approximately the same for the power-law model and MSA.

•1-3 Some effect is detected in the thin spots in the EPON which seems to occur at the same energy-loss as the edge-effect in the iron-containing parts. It has been noticed before in EELS-analysis that side-effects appear in thin spots or holes [Körtje *et al*, 1993]. These effects may be caused by some sort of scattering, the exact nature of which still has to be established. It may be caused by X-rays which cause the fluorescent screen to illuminate. The fact that the effects appear in the same images as the edge-effect seems to point to a certain relation between the two effects.

These thin spots in the EPON are less prominent when a shading-correction is performed or when the number of images is reduced. Further investigations have to be performed to explain these effects.

The original data-set can be reconstructed using only one factorial axis, e.g. factorial axis 1 (element-information). The effects of noise and other redundant information is reduced in the reconstructed set (not shown). This set can then be analyzed with the power-law method thus using MSA as a preprocessing step.

•4 More acquisition- and analysis-conditions such as the instrumental magnification, radiation-doses and slit-widths, may be examined to further improve the results.

•5 Iron was a relatively easy element to analyze, with a large available region for continuum-estimation. It was very interesting to perform the same analysis for a more complicated element such as calcium with the large carbon-edge just in front. Great care was taken to avoid the carbon-edge, so only two pre-edge images were used with four ionization-edge images. MSA detects differences in the images so,

in contrast to the power-law method, the use of only one pre-edge image is in principle sufficient. From the first factorial projection images we may conclude that MSA also performed satisfactorily with the calcium-set.

It has to be realized that by using MSA, so far only the presence/absence of the element is established. It remains to be determined whether the intensity can be used for concentration measurements. Recently Gelsema *et al.* (1992) have demonstrated that this may be the case.

In short we may conclude that MSA may be used to separate the different sources of information in a set of images. Only when two or more different effects happen in exactly the same images, the effects cannot be separated. Shading-correction is not necessary since this is accounted for in the average grey-value profile. Reduction of the number of images does not have a significant influence on the detected siderosome area. Side-effects such as thin spots in the EPON which appeared on the first factorial axis in the analyzed set have less influence in reduced sets. Therefore, a reduction of the number of images is possible. The use of six images is recommended to be able to read the different sources of information from the factorial axes.

---

# CHAPTER 9

## GENERAL DISCUSSION

## CHAPTER 9

### GENERAL DISCUSSION

The aim of the work described in this thesis was to obtain procedures that allow the localization and quantification of chemical elements in biological materials with electron energy-loss spectroscopy and electron spectroscopic imaging. Several problems had to be solved to allow elemental quantification in biological tissue.

For elemental analysis, first of all the presence of the elements had to be established. Therefore, the chemical elements were first identified by recording electron energy-loss spectra (chapter 3, 4). One of the first steps was to find the ionization-edge, for which the first derivative of the spectrum was used (chapter 2, 7). If the chemical element was present, the next step was to separate the ionization-edge from the continuum on which it is riding, for which a power-law function was fitted through the continuum preceding the ionization-edge:

$$I(E) = A * E^{-r} \quad (1.1)$$

By subtracting this continuum from the original spectrum, the edge was separated.

To optimize the continuum-fit of eq. 1.1 (the dependent variable) as a function of several experimental factors (the independent variables: A and r) the Simplex-method [Burton & Nickless (1987); Yarbo & Deming (1974); Shavers *et al.* (1979)] was proposed in this thesis. This method was compared to the two-area method [Egerton, (1986)], which is a very inaccurate method for continuum estimation, the LogLog method [Bevington (1969)] and the Steepest descent method [Colliex (1981)] and the Simplex-method and the LogLog-method proved to be superior. Comparison with the Steepest descent-method as proposed by Colliex (1981) learned that the Steepest descent-method tends to deviate from the optimal combination for A and r, while the LogLog-method as proposed by Bevington performed as adequately as the Simplex-method (chapter 3). Other methods have been tested afterwards by Van Puymbroeck (1992), leading to the conclusion that different regions (zero-loss, low-loss, high-loss) need different continuum-estimation algorithms. Special attention has to be paid to elements with core-losses

and plasmon-losses of other elements just in front of their ionization-edge, which will influence the continuum-fit (e.g. carbon L<sub>2,3</sub>-edge (284 eV) and the calcium K-edge (346 eV)).

For quantification of the element, the  $R_x^*$ -ratio as defined by Egerton (1986) may be used, which involves the measurement of all electrons that irradiate the specimen and pass the objective diaphragm:

$$R_x^* = \frac{I_{K,L,M,etc}(\beta, \Delta)}{I_t(\beta, \Delta) \cdot \sigma(\beta, \Delta)} \quad (1.2)$$

For this purpose, the first 100 eV in the energy-loss spectrum is used which approximates this value. However, due to instrumental problems (dynamic range of the electron-detectors),  $I_k$  and  $I_t$  could not be measured during the same analysis and another ratio ( $R_x$ ) was used in this thesis (chapter 3, 4):

$$R_x = \frac{I_{K,L,M,etc}(\beta, \Delta)}{I_{K,L,M,etc}(\beta, \Delta) + I_B(\beta, \Delta)} \quad (1.3)$$

Spectra allow only global measurement of the elements present in the analyzed area. Especially when only a small area is occupied by the chemical element, spectral analysis is very insensitive. In contrast to this, images give detailed information of the exact location of these elements and the analysis of chemical elements in images does not depend on the components in the rest of the image. However, image-analysis does induce other problems to be solved such as shading and the segmentation of the elemental area. At least two forms of shading were visible in the acquired images: additive- and multiplicative shading. The standard shading-correction procedure of the IBAS 2000 corrects for additive shading. An adequate shading-correction procedure should account for both the additive and the multiplicative component. However, when the extrapolated continuum-image is subtracted from the ionization-edge image, the additive shading is automatically accounted for in the resulting net-intensity image. When in the final procedure the net-intensity image is divided by the zero-loss image, the multiplicative component is also accounted for (chapter 7, 8).

Segmentation of the various contributions in an image as performed in this thesis is based on the cross-over point of the first derivative of the greyvalue

histogram as described in chapter 2. This method, which is based on the total greyvalue-distribution in the image to be analyzed, works adequately for the experiments shown in this thesis. In addition to these qualitative aspects, quantitative element distribution images are obtained with ESI. By recording several images in the pre-ionization edge region and one or more images in the post-ionization edge region, the continuum can be fitted pixel-wise and extrapolated just like in spectra.

Once the chemical elemental areas have been segmented, morphometrical analysis may be performed on semi net-intensity element-distribution images (chapter 6). Co-localization of several chemical elements was easily demonstrated with ESI. However, the results of chapter 6, as obtained with the two-window method, in which a PIE-image is subtracted from the IE-image, are highly disputable. Later experiments with more PIE-images, using the power-law method, learned that the phosphorus distribution image suffered from the influence of the Ce  $N_{4,5}$ -edge. The edges of phosphorus and cerium were lying so close together that they could not be separated. On the other hand, now it was possible to obtain sulphur distribution images. The localization of the sulphur coincided exactly with the barium distribution image.

It has been shown that calculations according to a power-law relation can be performed resulting in reliable quantitative net-intensity distribution images. The influence of the chosen fitting-procedure upon the final images is shown in chapter 7 (Fig. 7.4). However, these images still suffer from the presence of noise and other "useless" image elements. Therefore, the use of "Multivariate Statistical Analysis (MSA)" [Hannequin & Bonnet (1989), Bonnet & Hannequin (1988), Trebbia & Bonnet (1991), Trebbia & Mory (1991), Gelsema *et al.* (1992)] was investigated for the analysis of electron spectroscopic images (chapter 8). MSA is a sensitive method which allows in principle the separation of the element-information in a set of images, from the "useless" information, such as shading and radiation damage. Compared to the power-law model, the same results were obtained with MSA regarding the element-area. However, MSA was able to reduce the influence of artifacts induced during acquisition and analysis. This may influence the minimum detection limit, which has to be investigated further in future experiments. Moreover, since MSA makes reduction of the number of PIE-images possible, the calcium-signal in a set of images could clearly be separated,

which has always been a problem in biological material because of the carbon K-edge just in front of the calcium-edge. Only when different events happened in the same images, MSA was not able to separate these events completely. The source of the event that happened in the thin spots in the embedding material, which coincided with the element-effect still has to be investigated.

Sofar the images have only been used to demonstrate the presence and localization of the chemical elements, but concentration measurements still had to be performed. Like for spectra,  $R_x^*$ -images should be calculated. Instrumental problems have been solved in this case by introducing the optical calibrated attenuation filters in the image-pathway (chapter 2). The problems with  $R_x^*$ -measurements, may be solved for spectra by recording parallel spectra with the TV-camera (pEELS). However, energy-loss calibration is rather difficult in this case, especially since an aberration was observed at the edges of the tv-camera-images.

Our initial efforts to compare the quantitative spectral results to the quantitative image results were not very successful. Comparison of EEL-spectra and -images led to higher  $R_x$ -values for spectra. This may be explained by the higher resolution for the spectra because of the smaller slitwidth during acquisition ( $S_{slit}=1$  eV,  $I_{slit}=15$  eV) and the difference in analyzed area. As mentioned before, the localization of the chemical elements is more important than the overall concentration in the analyzed area. Therefore, future experiments should concentrate on image-analysis. Spectra may be used for quick identification of the elements, because of their higher resolution and their faster processing.

During acquisition of spectra and images of the elements as tested in this thesis several problems were encountered. The acquisition conditions have to be optimized in order to obtain optimal results after analysis. Several problems were investigated:

- *Radiation damage*

In the microscope, during acquisition, the section will suffer from radiation damage, which also causes some elements to evaporate. Therefore, sections should only be analyzed once and further experiments should be performed on a different section of the same specimen (chapter 5, 6). In addition, the acquisition of the spectra and images must be kept as short as possible and the time-lapse between

two successive acquisitions has to be kept constant (chapter 8).

- *Section thickness*

EELS and ESI of ultrathin sectioned material also have their instrumental limitations. The section thickness has to be below the mean free pathlength for the electrons, depending on the element (chapter 1). The section-thickness ( $t$ ) was measured by re-embedding the specimen and variations in thickness in between cross-sectioned Bio-standard beads and surrounding EPON were established. The results obtained confirmed the observations of Door *et al.* (1990) that the inelastic mean free pathlength ( $\lambda_{in}$ ) for EPON at an accelerating voltage of 80 keV is 209.1 nm. When plotting  $R_x$  against section thickness ( $t$ ), a linear relationship is observed. Only when the section thickness exceeds  $\lambda_{in}$ , is this linear relationship not longer valid (chapter 5).

- *Specimen treatment*

Most elements (Ca, Fe, Ba, Ce, P, S), that are present in the original specimen survive the classical treatment of the specimen to allow observation in the EM (fixation, embedding, sectioning), depending on the solubility and attachment to the organic matrix. Other elements (Na, K) are washed out of the specimen or are evaporated by the beam-electrons during the acquisition (Bo). Therefore, it is vital to treat the specimen carefully and to know the consequences of the treatment for the elemental composition of the specimen. Cryo-fixation may solve this problem (see also chapter 6).

The overall conclusion of this thesis is that EELS is a method which allows element-analysis on a cellular level by spectral analysis. It can easily identify chemical elements in biological materials. Element distribution-images are easily and quickly obtained. Moreover, analysis by the ESI-technique gives good quality high-resolution contrast images from unstained thin sections. To minimize the relative intensity of the background, EELS and ESI require a very thin specimen ( $\leq 200$  nm for 80 keV incident energy).

Results as obtained with MSA are comparable to the results as obtained with the power-law method. In addition, MSA was able to retrieve the calcium information from a set of calcium-images. The power-law method failed in this case, since not enough images in front of the Ca-edge are available for the continuum-fit. It is to be expected that other elements such as phosphorus which encounter similar problems with the power-law method may also adequately be analyzed with MSA.

---

# ABBREVIATIONS

---

$\beta$	Aperture of the objective-lens back-focal plane
$\Delta$	region of the spectrum used for quantification
$\Delta E_i$	Energy-loss $i$
$\Gamma$	Region of the spectrum used for background-estimation
$\lambda_x$	Minimum free pathlength of element $x$
$\rho$	Specific density
$\sigma$	Partial ionization cross-section, the probability that an incident electron causes edge-phenomena
$\bar{\sigma}$	Averaged matrix cross-sections for all EELS-background contributions
$A$	parameter for background calculation (conventional method)
$A$	Atomic mass
$B$	Best fit in simplex-procedure
CTEM	Conventional Transmission Electron Microscope
$E$	Energy-loss
$E_0$	Initial energy of the beam
EDX	Energy Dispersive X-ray microanalysis
EELS	Electron Energy Loss Spectroscopy
EFTEM	Energy Filtered Transmission Electron Microscopy
EM	Electron Microscope
EPMA	Electron Probe MicroAnalysis
EPON	LX-112 plastic embedding material
ESI	Electron Spectroscopic Imaging
$G$	Goodness function for the simplex-procedure
eV	Electron Volt
IBAS	Integriert Bild Analyse System (Integrated Image Analysis System)
IC5	Antibody directed against viral-coat proteins
IE	Ionization Edge
$I(E)$	Intensity at energy-loss $E$
$I_B$	Background integral
$I_{K, L, M}$	Core-loss integral
$I_t$	All electrons in the spectrum (usually all electrons from 0-100 eV which contains 98% of all electrons)
$M$	Molecular weight
MSA	Multivariate Statistical Analysis
$N$	Next best fit in simplex-procedure
$N_A$	Avogadro's number

NAA	Neutron activation analysis
$N_x$	Number of atoms of element x
$N_T$	Total number of matrix atoms per unit area
PIE	Pre Ionization Edge
PMT	Photomultiplier
PVP	Polyvinyl pyrolidone
QIA	Quantitative Image Analysis
QSA	Quantitative Spectral Analysis
r	parameter for background calculation (conventional method)
$R_x^*$	Relative element concentration using eq. 2
$I_{R_x}, S_{R_x}$	Relative element concentration using eq. 3 in images (I) and spectra (S)
STEM	Scanning Transmission Electron Microscope
t	Thickness of the specimen
TEM	Transmission Electron Microscope
$t_G$	preset criterion on the goodness function G in the simplex-procedure
W	Worst fit in simplex-procedure
x	Chemical element



---

# REFERENCES

- 
- Adamson-Sharpe K.M. and Ottensmeyer F.P. (1981) Spatial resolution and detection sensitivity in micro-analysis by electron energy loss selected imaging. *J. Microsc.* **122**: 309-314.
- Ahn C. and Rez P. (1985) Inner shell edge profiles in electron energy loss spectroscopy. *Ultramicroscopy* **17**: 105-116.
- Andrew J.W., Ottensmeyer F.P. and Martell E. (1978) An improved magnetic prism design for a transmission electron microscope energy filter. *Electron Microscopy/1978 9<sup>th</sup> Int. Cong.* **1**, Ed. by J.M. Sturgess, Microscopical Society of Canada, Toronto: 536-537.
- Arsenault A.L. and Ottensmeyer F.P. (1983) Quantitative spatial distributions of calcium, phosphorus and sulphur in calcifying epiphysis by high resolution spectroscopic imaging. *Proc. nat. Acad. Sci. U.S.A.* **80**: 1322-1326.
- Arsenault A.L. and Ottensmeyer F.P. (1984) Stereoscopic representation of complex overlapping elemental maps in electron spectroscopic images. *J. Microsc.* **133**: 69-72.
- Bentley J, Lehman G.L. and Sklad P.S. (1982) Improved background fitting for electron energy loss spectra. *Proc. 10<sup>th</sup> International congress on electron microscopy* **1**: 585-586.
- Berger S.D. and Pennycook S.J. (1982) Detection of nitrogen at {100} platelets in diamond. *Nature* Vol. **298**: 635-637.
- Berriman J. and Leonard K.R. (1986) Methods for specimen thickness determination in electron microscopy. *Ultramicroscopy* **19**: 349-366.
- Bevington P.R. (1969) *Data reduction and error analysis for the physical sciences*. McGraw-Hill book company, New York, San Francisco, St. Louis, Toronto, London and Sydney: p. 246-254.
- Bihl J., Rilk A. and Benner G. (1988) Angle of acceptance and energy resolution in the imaging electron energy-loss spectrometer of the EM 902. *Inst. Phys. Conf. Ser. No 93 1. Tutorials, Instrumentation and Techniques*, Ed. by P.J. Goodhew & H.G. Dickinson, Institute of Physics, Bristol and Philadelphia, Chapter 2: 159-160
- Blaineau S., Julliard A.K., Amsellem J. and Nicaise G. (1987) Quantitative X-ray microanalysis of calcium with the Camebax-TEM system in frozen, freeze-substituted and resin-embedded tissue sections. *Histochemistry* **87**: 545-555.
- Bonnet N., Colliex C., Mory C and Tencé M. (1988) Developments in processing image sequences for elemental mapping. *Scanning Microsc. Suppl.* **2**, Ed. by O. Johari, SEM Inc., AMF O'Hare, Chicago, Ill.: 351-364.

- 
- Bonnet N. and Hannequin P. (1989) Chemical mapping and multivariate statistical analysis (prospect) *Ultramicroscopy* **28**: 248-251.
- Bonnet N., Simova E. and Thomas X. (1991) Application of multivariate statistical analysis to time dependent spectroscopy. *Microsc. Microanal. Microstruct.* **2**: 129-142.
- Bonnet N. and Trebbia P. (1993) Multi-dimensional data analysis and processing in electron-induced microanalysis. In press.
- Borland L. and Van Heel M. (1990) Classification of image data in conjugate representation spaces. *J. Opt. Soc. Am. A.* **4**: 601-610.
- Burton K.W.C. and Nickless G. (1987) Optimisation via Simplex. Part I. Background, definitions and a simple application. *Chemometrics and Intelligent Laboratory Systems* **1**: 135-149.
- Carlemalm E., Acetarin J.D., Villiger W., Colliex C. and Kellenberger E. (1982) Heavy metal containing surroundings provide much more "negative" contrast by Z-imaging in STEM than with conventional modes. *J. Ultrastruct. Res.* **80**: 339-343.
- Castaing R. and Henry L. (1962) Filtrage magnetique des vitesses en microscopie électronique. *C.R. Acad. Sci. Paris* **B255**: 76-78.
- Castaing R. (1975) Energy filtering in electron microscopy and electron diffraction. *Physical Aspects of Electron Microscopy and Microbeam Analysis*, Ed. by B. Siegel, Wiley, New-York: 287-301.
- Cleton M.I., Roelofs J.M., Blok-Van Hoek C.J.G. and De Bruijn W.C. (1986) Integrated image and X-ray microanalysis of hepatic lysosomes in a patient with idiopathic hemosiderosis before and after treatment by phlebotomy. *Scanning Electron Microsc.* **1986/III**, Ed. by O. Johari, SEM Inc., A.M.F. O'Hare, Chicago, Ill.: 999-1006.
- Cleton M.I., Mostert L.J., Sorber C.W.J., de Jong A.A.W., De Jeu-Jaspers C.M.H. and De Bruijn W.C. (1989) Effect of phlebotomy on the ferritin iron content in the rat liver as determined morphometrically with the use of electron energy-loss spectroscopy. *Cell and Tissue Res.* **256**: 601-605.
- Colliex C., Jeanguillaume C., Trebbia P. (1981) Quantitative local microanalysis with EELS. *Microprobe Analysis of Biological Systems*, Ed. by T.E. Hutchinson and A.P. Somlyo, Academic Press, New York: 251-271.
- Colliex C., Jeanguillaume C. and Mory C. (1984) Unconventional modes for STEM imaging of biological structures. *J. Ultrastr. Res.* **88**: 177-206
- Colliex C. (1985) An illustrated review on various factors governing the high spatial

- 
- resolution capabilities in EELS microanalysis. *Ultramicroscopy* **18**: 131-150.
- Colliex C., Manoubi T. and Krivanek O.L. (1986) EELS in the electron microscope: a review of present trends. *J. Electron Microsc.* **35/4**: 307-313.
- Dantzig G.B. (1963) *Linear programming and extensions*. Princeton University Press, Princeton, NJ.
- De Bruijn W.C., Schellens J.P.M., Van Buitenen J.M.H. and Van der Meulen J. (1979) X-ray microanalysis of colloidal-gold labelled lysosomes in rat liver sinusoidal cells after incubation with acid phosphatase activity. *Histochemistry* **66**: 137-148.
- De Bruijn W.C. (1981) Ion exchange beads as standards for X-ray microanalysis of biological tissue. *Beitr. Elektronemikrosk. Direktabb. Oberfl.* **16**: 369-372.
- De Bruijn W.C. (1981) Ideal standards for quantitative X-ray microanalysis of biological specimens. *Scanning Electron Microscopy 1981/II*, Ed. by O. Johari, SEM Inc., A.M.F. O'Hare, Chicago, Ill: 357-367.
- De Bruijn W.C. and Zeelen J.Ph. (1983) Combined image and X-ray microanalysis of biological material. *Beitr. Elektronemikrosk. Direktabb. Oberfl.* **16**: 385-388.
- De Bruijn W.C. (1984) Standards for quantitative X-ray microanalysis of biological specimens. *Les Editions de Physique. Colloque C2, suppl. 2; Tome 45*, Les Editions de Physique, Toulouse, France: 469.
- De Bruijn W.C. (1985) Integration of X-ray microanalysis and morphometry of biological material. *Scanning Electron Microscopy 1985/II*, Ed. by O. Johari, SEM Inc., A.M.F. O'Hare, Chicago, Ill: 697-712.
- De Bruijn W.C. and Cleton-Soeteman M.I. (1985) Application of chelex standard beads in integrated morphometrical and X-ray micro-analysis. *Scanning Electron Microscopy 1985/II*, Ed. by O. Johari, SEM Inc., A.M.F. O'Hare, Chicago, Ill: 715-729.
- De Bruijn W.C., Van der Meulen J., Brederoo P. and Daems W.Th. (1986) Pt-staining of peroxidase reaction products at the ultrastructural level *Histochemistry* **84**: 492-500.
- De Bruijn W.C., Ketelaars D., Vermeij M., Cao L.C., Boevé E. and Schröder F.H. (1987) Image analysis and X-ray microanalysis in cytochemistry. *Scanning Microsc.* **1987/4**, Ed. by O. Johari, SEM Inc., A.M.F. O'Hare, Chicago, Ill: 1651-1667.
- De Bruijn W.C. and Van Miert M.P.C. (1988) Extraneous background-correction program for matrix bound multiple point X-ray microanalysis. *Scanning*

- Microsc.* 1988/2, Ed. by O. Johari, SEM Inc., A.M.F. O'Hare, Chigaco, Ill: 319-322.
- De Bruijn W.C., Sorber C.W.J., De Jong A.A.W. and Cleton-Soeteman M.I. (1989) Quantitative image analysis with EELS and EPMA in cytochemistry. *Proc. 1st Eur. Workshop. Europ. Microbeam Analysis Soc.*, p 191.
- De Bruijn W.C. and Sorber C.W.J. (1990) The application of Bio-standards for electron energy-loss analysis of biological materials. *Proc. XII<sup>th</sup> Intern. Congress for Electron Microscopy Seattle 2*, San Francisco Press Inc.: 68-69.
- Bruijn W.C., Ketelaars D., Gelsema E. and Sorber L. (1991) Comparison of the simplex method with several other methods for background-fitting for electron energy loss spectral quantification of biological materials. *Microsc. Microanal. Microstruct.* 2: 281-291.
- Door, R., Frösch D. and Martin R. (1991) Estimation of section thickness and quantification of iron standards with EELS. *J. Microsc.* 162: 15-22.
- Drechsler M. and Cantow H.-J. (1991) EELS data acquisition, processing and display for the Zeiss CEM 902 based on Lotus 1-2-3<sup>®</sup>: application examples from a biological system and inorganic transition metal compounds. *J. Microsc.* 162: 61-76.
- Egerton R.F., Philip J.G., Turner P.S. and Whelan M.J. (1975) Modification of a transmission electron microscope to give energy-loss spectra and energy-selected images and diffraction patterns. *J. Phys. E.* 8: 1033-1037.
- Egerton R.F. (1986) *Energy Loss-Spectroscopy in the electron microscope*. Plenum Press, New York and London.
- Egerton R.F. and Crozier P.A. (1987) A compact parallel-recording detector for EELS. *J. Microsc.* 148: 157-166.
- Egle W., Rilk A., Bihl J. and Menzel M. (1984) Microanalysis in the EM 902: Tests on a new TEM for ESI and EELS. *42<sup>nd</sup> Ann. Proc. Electron Microsc. Soc. A.* 1, Ed. by G.W. Bailey, San Francisco Press, San Francisco: 566-567.
- Engel A. and Reichelt R. (1984) Imaging of biological structures with the scanning transmission electron microscope. *J. Ultrastruct. Res.* 88: 105-120.
- Fiori C.E., Swyt C.R. and Gorlen K.E. (1981) Applications of the top-hat digital filter to a non-linear spectral unravelling procedure in energy-dispersive X-ray microanalysis. *Proceedings of the Microbeam Analysis Society*, Ed. by R. Geiss: 320.
- Gelsema E.S., Queiros C. and Timmers T. (1982) The formalism of correspondence analysis as a means to describe object samples. *Proc. 6<sup>th</sup> ICFR, München*.

---

564-568.

- Gelsema E.S., Beckers A.L., Sorber C.W., de Bruijn W.C. (1992) Correspondence analysis for quantification in electron energy loss spectroscopy and imaging. *Methods-Inf-Med* **31** (1): 29-35.
- Gelsema E.S., Beckers A.L.D., Sorber C.W.J. and De Bruijn W.C. (1992) Quantification procedures for electron energy-loss spectroscopy and imaging: the use of correspondence analysis for element determination. *J. Microsc.* **166** (3): 287-296.
- Goodhew P.J. and Humphreys F.J. (1988) *Electron microscopy and analysis*. Taylor and Francis, London, New-York, Philadelphia: 20-38.
- Gravekamp C, Koerten H.K., Verwoerd N.P., De Bruijn W.C. and Daems W.Th. (1982) Automatic image analysis applied to electron micrographs. *Intern. Rev.* **6**: 656-657.
- Groot C.G. (1981) Positive colloidal thorium dioxide as an electron microscopical contrasting agent for glycosaminoglycans, compared with ruthenium red and positive colloidal iron. *Histochemistry*. **71**: 617-627.
- Gundersen H.J.G. (1986) Stereology of arbitrary particles. *J. Microsc.* **143**: 3-45.
- Hannequin P. and Bonnet N. (1988) Application of multivariate statistical analysis to energetic image series. *Optik* **81**: 6-11.
- Harauz G. and Ottensmeyer F.P. (1984a) Direct three-dimensional reconstruction for macromolecular complexes from electron micrographs. *Ultramicroscopy* **12**: 309-320.
- Harauz G. and Ottensmeyer F.P. (1984b) Nucleosome reconstruction via phosphorus mapping. *Science* **226**: 936-940.
- Henkelman R.M. and Ottensmeyer F.P. (1974b) An energy filter for biological electron microscopy. *J. Microsc.* **102**: 79-94.
- Hezel U.B., Bauer R., Zellmann E. and Miller W.I. (1986) Resolution and contrast enhancement on biological specimens by means of electron spectroscopic imaging (ESI). *Proc. 44th annual meeting, EMSA*. Ed. by G.W. Baily, San Francisco Press Inc., San Francisco: 68-69.
- Hezel U.B., Bauer R. and Meißner D. (1987) New applications in electron spectroscopic imaging, electron energy-loss spectroscopy and electron spectroscopic diffraction for biomedical and material science. *Proc. Congress Electron Microscopy, Bologna*, 267-268.
- Johannsen G. and Bille J. (1982) A threshold selection method using information measures. *Proc. Int. Conf. Pattern Recognition. Inst. Electrical. Electronic*

- Engineers Inc.* 1(Computer Soc. Press. München): 140-142.
- Joy D.C. and Maher D.M. (1980) Electron energy loss spectroscopy : detectable limits for elemental analysis. *Ultramicroscopy* 5: 333-342.
- Joy D.C. and Maher M. (1981) The quantification of electron energy-loss spectra. *J. Microsc.* 124: 37-48.
- Körtje K.H., Freihöfer D. and Rahmann H. (1990) Cytochemical localization of calcium in the central nervous system of vertebrates. *Ultramicroscopy* 32: 12-17.
- Körtje K.H., Körtje D. and Rahmann H. (1990) The application of energy-filtering electron microscopy for the cytochemical localization of  $\text{Ca}^{2+}$ -ATPase activity in synaptic terminals. *J. Microsc.* 162: 105-114.
- Körtje K.H. (1993) personal communications
- Krahl D., Herrmann K.-H. and Kunath W. (1978) Electron optical experiments with a magnetic imaging filter. *Electron Microscopy/1987* 9<sup>th</sup> Int. Cong. Ed. by J.M. Sturgess, Microscopical Society of Canada, Toronto: 42-43.
- Krivanek O.L., Gubbens A.J. and Dellby N. (1991) Developments in EELS instrumentation for spectroscopy and imaging. *Microsc. Microanal. Microstruct.* 2: 315-332.
- Kruit P. and Shuman H. (1985) The influence of objective lens aberrations in energy-loss spectrometry. *Ultramicroscopy* 17: 263-268.
- Leapman, R.D., Fiori, C.E. & Swyt, C.R. (1984a) Mass thickness determination by electron energy loss for quantitative X-ray microanalysis in biology. *J. Microsc.* 133: 239-253.
- Leapman R.D., Fiori C.E., Gorlen K.E., Gibson C.C. and Swyt C.R. (1984b) Combined elemental and STEM imaging under computer control. *Ultramicroscopy* 12: 281-292.
- Leapman R.D., Gorlen K.E. and Swyt R.E. (1985) Digital processing of electron energy-loss spectra and images. *Scanning Electron Microscopy 1985/I*, Ed. by O. Johari, SEM, AMF O'Hare, Chicago. Ill.: 1-13.
- Leapman R.D. and Ornberg R.L. (1988) Quantitative electron energy loss spectroscopy in biology. *Ultramicroscopy* 24: 251-268.
- Leapman R.D. and Swyt C.R. (1988) Separation of overlapping core edges in electron energy loss spectra by multiple-least-squares fitting. *Ultramicroscopy* 26: 393-404.
- Liu D.R. and Brown L.M. (1987) Influence of some practical factors on background extrapolation in EELS quantification. *J. Microsc.* 147: 37-49.

- 
- Loretto M.H. (1984) *Electron beam analysis of materials* Chapman and Hall Ltd., London, chapter 2.
- Malis T., Cheng S.C. and Egerton R.F. (1988) EELS Log-ratio technique for specimen-thickness measurement in the TEM. *J. Electr. Microsc. Techn.* **8**: 193-200.
- Meyer F. (1981) Cytology automation with mathematical morphology. *Biol. Cell.* **41**: 1-6.
- Morgan E., Burton K. and Nickless G. (1990) Optimization using the modified Simplex method. *Chemometrics and Intelligent Laboratory Systems* **7**: 209-222.
- Mostert L.J., Cleton M.I., De Bruijn W.C., Koster J.F. and Van Eijk H.G. (1989) Studies on ferritin in rat liver and spleen during repeated phlebotomy. *Int. J. Biochem.* **21**: 39-47.
- Müller A. (1906) Bemerkungen über das Hydrosols des Thoriumoxydhydrats. *Ber. Deutsch. Chem. Ges.* **93**: 2857-2859.
- Nelder J.A. and Mead R. (1965) A Simplex method for function minimisation. *Computer Journal* **7**: 308-313.
- Newbury D.E. (1986) *Principles of analytical electron microscopy*. Ed. by D.C. Joy, A.D. Romig Jr. and J.I. Goldstein, Plenum Press, New-York: 1-27.
- Ottensmeyer P.F. (1984) Electron spectroscopic imaging: parallel energy-filtering and microanalysis in the fixed-beam electron microscope. *J. Ultrastruct. Res.* **88**: 121-134.
- Peachy L.D., Heath J.P. and Lamprecht G. (1986) The use of an energy-filtering electron microscope to reduce chromatic aberration in images of thick biological specimens. *Proc. 44th annual meeting, EMSA*. Ed. by G.W. Baily, San Francisco Press Inc., San Francisco: 88-91.
- Pejas W. and Rose H. (1978) Outline of an imaging magnetic energy filter free of second-order aberrations. *Electron Microscopy/1978 9<sup>th</sup> Int. Cong.*, Ed. by J.M. Sturgess, Microscopical Society of Canada, Toronto: 44-45.
- Probst W. (1986) Ultrastructural localization of calcium in the CNS of vertebrates. *Histochemistry* **85**: 231-239.
- Pun T., Ellis J.R. and Eden M. (1984) Optimized acquisition parameters and statistical detection limits in quantitative EELS. *J. Microsc.* **135**: 295-316.
- Pun T., Ellis J.R. and Eden M. (1985) Weighted least squares estimation of background in EELS imaging. *J. Microsc.* **137**: 93-100.
- Rademakers L.H.P.M., Koningsberger J.C., Sorber C.W.J., Baart de la Faille H.,

- Van Hattum J. and Marx J.J.M. (1993) Accumulation of iron in erythroblasts of patients with erythropoietic protoporphyria. *European Journal of Clinical Investigation* **23**: 130-138.
- Reichelt R. and Engel A. (1984) Monte carlo calculations of elastic and inelastic electron scattering in biological and plastic materials. *Ultramicroscopy* **13**: 279-294.
- Reimer L., Fromm I. and Rennekamp R. (1988) Operation modes of electron spectroscopic imaging and electron energy-loss spectroscopy on a transmission electron microscope. *Ultramicroscopy* **24**: 339-354.
- Reimer L. and Ross-Messemer M. (1990a) Contrast in the electron spectroscopic imaging mode of a TEM. II. Z-ratio, structure-sensitive and phase contrast. *J. Microsc.* **159**: 143-160.
- Reimer L. and Ross-Messemer M. (1990b) Contrast in the electron spectroscopic imaging mode of a TEM I. Influence of zero-loss filtering on a scattering contrast. *J. Microsc.* **155**: 169-182.
- Reimer L. (1991) Energy-Filtering Transmission Electron Microscopy. *Advances in electronics and electron physics* **81**: 43-126.
- Reimer L., Rennekamp R., Fromm I. and Langenfeld M. (1991) Contrast in the electron spectroscopic imaging mode of a TEM. IV. Thick specimens imaged by the most-probable energy loss. *J. Microsc.* **162**: 3-14.
- Ringeling P.L., Cleton M.I., Kroos M.J., Sorber C.W.J., De Bruijn W.C., Harrison P.M. and Van Eijk H.H. (1989) Lysosomal and cytosolic ferritins. A biochemical and electron-spectroscopic study. *Biol. Metals* **2**: 114-121.
- Ringeling P.L., Cleton M.I., Huijskes-Heins M.I.E., Seip M.J.E., De Bruijn W.C. and Van Eijk H.G. (1990) Analysis of iron-containing compounds in different compartments of the rat-liver after iron loading. *Biol. Metals* **3**: 176-182.
- Roomans G.M. and Shelburne J.D. (1980) Basic methods in biological X-ray microanalysis in. *Scanning Electron Microsc.* **II**, Ed. by O. Johari, SEM Inc. A.M.F. O'Hare, Chigaco, Ill.: 309-321.
- Roos N. and Barnard T. (1984) Aminoplastic standards for quantitative X-ray microanalysis of thin sections of plastic-embedded biological material. *Ultramicroscopy* **15**: 277-286.
- Rose H. and Plies E. (1974) Entwurf eines fehlerarmen magnetischen Energie-Analysators. *Optik* **40**: 336-341.
- Russ J.C. and Russ J.C. (1984) Image processing in a general purpose computer. *J. Microsc.* **135**: 89-102.

- 
- Russ J.C. and Russ J.C. (1987) Automatic discrimination of features in grey-scale images. *J. Microsc.* **148**: 263-277.
- Shavers C.L., Parsons M.L. and Deming S.N. (1979) Simplex optimization of chemical systems. *J. Chem. Ed.* **56**: 307-309.
- Shuman H. and Somlyo A.P. (1982) Energy-filtered transmission electron microscopy of ferritin. *Proc. Nat. Acad. Sci. USA* **79**: 106-107.
- Shuman H., Chang C.F., and Somlyo A.P. (1986) Elemental imaging and resolution in energy-filtered conventional electron microscopy. *Ultramicroscopy* **19**: 121-133.
- Shuman H. and Somlyo A.P. (1987) Electron energy loss analysis of near-trace-element concentrations of calcium. *Ultramicroscopy* **21**: 23-32.
- Somlyo A.P. and Shuman H. (1982) Electron probe and electron energy loss analysis in biology. *Ultramicroscopy* **8**: 219-233.
- Somlyo A.P. (1984) Compositional mapping in biology: X-rays and electrons. *J. Ultrastruct. Res.* **88**: 135-142.
- Sorber C.W.J., De Jong A.A.W., Den Breejen N.J. and De Bruijn W.C. (1990a) Quantitative energy-filtered image analysis in cytochemistry I. Morphometric analysis of contrast related images. *Ultramicroscopy* **32**: 55-68.
- Sorber C.W.J., Van Dort J.B. Ringeling P.C., Cleton-Soeteman M.I. and De Bruijn W.C. (1990b) Quantitative energy-filtered image analysis in cytochemistry II. Morphometric analysis of element-distribution images. *Ultramicroscopy* **32**: 69-79.
- Sorber C.W.J., Ketelaars G.A.M., Gelsema E.S., Jongkind J.F. and De Bruijn W.C. (1991a) Quantitative analysis of electron energy-loss spectra from ultrathin-sectioned biological material. I. Optimization of the background-fit with the use of Bio-standards. *J. Microsc.* **162**: 23-42.
- Sorber C.W.J., Ketelaars G.A.M., Gelsema E.S., Jongkind J.F. and De Bruijn W.C. (1991b) Quantitative analysis of electron energy-loss spectra from ultrathin-sectioned biological material. I. The application of Bio-standards for quantitative analysis. *J. Microsc.* **162**: 43-54.
- Spendley W., Hext G.R. and Himsforth F.R. (1962) Sequential application of Simplex designs in optimisation and evolutionary operations. *Technometrics* **4**: 441-461
- Steele J.D., Titchmarsh J.M., Chapman J.N. and Paterson J.H. (1985) A single-stage process for quantifying electron energy loss spectra. *Ultramicroscopy* **17**: 273-276.

- Stobbs W.M. and Boothroyd C.B. (1991) Approaches for energy loss and energy filtered imaging in TEM in relation to the materials problems to be solved. *Microsc. Microanal. Microstruct.* **2**: 333-350.
- Titchmarsh J.M. and Malis T.F. (1989) On the effect of objective lens chromatic aberration on quantitative electron-energy-loss spectroscopy (EELS). *Ultramicroscopy* **28**: 277-282.
- Trebbia P. (1988) Unbiased method for signal estimation in electron energy loss spectroscopy, concentration measurements and detection limits in quantitative microanalysis: methods and programs. *Ultramicroscopy* **24**: 399-408.
- Trebbia P. (1989) *Proc. 1st Europ. Workshop. Europ. Microbeam Analysis Soc.*: 107.
- Trebbia P. and Bonnet N. (1990). EELS elemental mapping with unconventional methods. I Theoretical bases: image analysis with multivariate statistics and entropy concepts. *Ultramicroscopy* **34**: 165-178.
- Trebbia P. and Mory C. (1990) EELS elemental mapping with unconventional methods II. Applications to biological specimens. *Ultramicroscopy* **34**: 179-203.
- Trebbia P. (1990) EELS elemental mapping with unconventional methods I. Theoretical basis: image analysis with multivariate statistics and entropy concepts. *Ultramicroscopy* **36**: 165-178.
- Trinick J. and Berriman J. (1987) Zero-loss electron microscopy with the Zeiss EM902. *Ultramicroscopy* **21**: 393-398.
- Van der Meijden W., Koerten H.K., Van Mourik W. and De Bruijn W.C. (1988) Descriptive light and electron microscopy of normal and clue cell-positive discharge. *Gynecol. obstet. Invest.* **25**: 47-57.
- Van Dort J.B., Zeelen J.Ph. and de Bruijn W.C. (1987) An improved procedure for the X-ray microanalysis of acid phosphatase activity in lysosomes. *Histochemistry* **87**: 71-77.
- Van Dort J.B., Ketelaars G.A.M., De Jong A.A.W. and De Bruijn W.C. (1988) Electron energy-loss spectroscopy in ultrastructural cytochemistry. *Inst. Phys. Conf. Ser.* **93**, York: 577-578.
- Van Dort J.B., Ketelaars G.A.M., Daems W. Th. and De Bruijn W.C. (1989) Ultrastructural electron probe X-ray microanalytical reaction product identification of three different enzymes in the same mouse resident peritoneal macrophage. *Histochemistry* **92**: 243-253.
- Van Puymbroeck J. (1992) *Electron energy-loss spectroscopy: Development of*

---

*methodology and software for the acquisition and processing of spectra.*  
Thesis.

- Verbeek P.W., Vrooman H.A., Van Vliet L.J. (1988) Low-level image processing by Max-Min filters. *Signal Processing* **15**, 249-258.
- Verbucken A.H., van Grieken E., Poulas G.J. and De Bruijn W.C. (1984) Embedded ion exchange beads as standards, for laser microprobe mass analysis of biological specimens. *Analytical Chemistry* **56**: 1362-1370.
- Yarbo L.A. and Deming S.N. (1974) Selection and preprocessing of factors for simplex optimization. *Anal. Chim. Acta* **73**: 391-398.
- Young, I.T. (1988) Sampling density and quantitative microscopy. *Anal. quant. Cytol. histol.* **10/4**: 269-275.
- Zaluzec N.J. (1985) Digital filters for application to data analysis in electron energy-loss spectroscopy. *Ultramicroscopy* **18**: 185-190.
- Zanchi G., Perez J.-P. and Sevely J. (1975) Adaptation of a magnetic filtering device on a one megavolt electron microscope. *Optik* **43**: 495-501.
- Zanchi G., Sevely J. and Jouffrey B. (1977a) An energy filter for high voltage electron microscopy. *J. Microsc. Spectrosc. Electron.* **2**: 95-104.
- Zanchi G., Sevely J. and Jouffrey B. (1977b) Second-order image aberration of a one megavolt magnetic filter. *Optik* **48**: 173-192.
- Zanchi G. Kihn Y. and Sevely J. (1982) On aberration effects in the chromatic plane of the OMEGA filter. *Optik* **60**: 427-436.
- Zondervan P.E., de Jong A., Sorber C.W.J., Kok L.P., De Bruijn W.C. and Van der Kwast Th.H. (1988) Microwave-stimulated incubation in immunoelectron microscopy: a quantitative study. *Histochemical J.* **20**: 359-364.

---

**LIST  
OF  
PUBLICATIONS**

---

**LIST OF PUBLICATIONS**

- Sorber C.W.J., De Jong A.A.W., Den Breejen N.J. and De Bruijn W.C. (1990) Quantitative energy-filtered image analysis in cytochemistry I. Morphometric analysis of contrast related images. *Ultramicroscopy* **32**, p. 55-68.
- Sorber C.W.J., Van Dort J.B. Ringeling P.C., Cleton-Soeteman M.I. and De Bruijn W.C. (1990) Quantitative energy-filtered image analysis in cytochemistry II. Morphometric analysis of element-distribution images. *Ultramicroscopy* **32**, p. 69-79.
- Sorber C.W.J., Ketelaars G.A.M., Gelsema E.S., Jongkind J.F. and De Bruijn W.C. (1991) Quantitative analysis of electron energy-loss spectra from ultrathin-sectioned biological material. I. Optimization of the background-fit with the use of Bio-standards. *J. Microsc.* **162**, p. 23-42.
- Sorber C.W.J., Ketelaars G.A.M., Gelsema E.S., Jongkind J.F. and De Bruijn W.C. (1991) Quantitative analysis of electron energy-loss spectra from ultrathin-sectioned biological material. I. The application of Bio-standards for quantitative analysis. *J. Microsc.* **162**, p. 43-54.
- Sorber C.W.J., Ketelaars G.A.M., Beckers A.L.D. and De Bruijn W.C. (1991) *Proc. 2<sup>nd</sup> Europ. Workshop European Microbeam Analysis Soc.*, p. 76.
- Sorber C.W.J., Bonnet N, Trebbia P., Gelsema E.S., Jongkind J.F., Beckers A.L.D. and De Bruijn W.C. (1993) Multivariate Statistical Analysis as a tool for EELS-analysis: submitted to *J. Microsc.*

---

**OTHER PUBLICATIONS**

- Cleton M.I., Mostert L.J., Sorber C.W.J., de Jong A.A.W., De Jeu-Jaspers C.M.H. and De Bruijn W.C. (1989) Effect of phlebotomy on the ferritin iron content in the rat liver as determined morphometrically with the use of electron energy-loss spectroscopy. *Cell and Tissue Res.* **256**: 601-605.
- De Bruijn W.C., Sorber C.W.J., De Jong A.A.W. and Cleton-Soeteman M.I. (1989) Quantitative image analysis with EELS and EPMA in cytochemistry. *Proc.. 1st Eur. Workshop. Europ. Microbeam Analysis Soc.*: 191.
- De Bruijn W.C. and Sorber C.W.J. (1990) The application of Bio-standards for electron energy-loss analysis of biological materials. *Proc. XII<sup>th</sup> Intern. Congress for Electron Microscopy Seattle 2*, San Francisco Press Inc.: 68-69.
- De Bruijn W.C., Ketelaars D., Gelsema E. and Sorber L. (1991) Comparison of the simplex method with several other methods for background-fitting for electron energy loss spectral quantification of biological materials. *Microsc. Microanal. Microstruct.* **2**: 281-291.
- De Bruijn W.C., Ketelaars G.A.M., Jongkind J.F. and Sorber C.W.J. (1991) *Proc. 2<sup>nd</sup> Europ. Workshop European Microbeam Analysis Soc.*: 40.
- De Bruijn W.C., Sorber C.W.J., Trommelen-Ketelaars G.A.M., Jongkind J.F., Beckers A.L.D. and Gelsema E.S. (1993) Electron energy-loss spectroscopy and electron probe X-ray microanalysis of biological material: a comparative quantitative analysis of electron microscopical images. In: *X-ray Microanalysis in biology: Experimental techniques and applications*. Edited by Sigee D.C, Morgan A.J., Summer A.T and Warley A.: p. 81-98.
- De Bruijn W.C., Sorber C.W.J., Gelsema E.S., Beckers A.L.D., Jongkind J.F. (1993) Energy-filtered transmission electron microscopy of biological specimens *Scanning Microscopy*: in press.

- 
- Gelsema E.S., Beckers A.L., Sorber C.W. and de Bruijn W.C. (1992) Correspondence analysis for quantification in electron energy loss spectroscopy and imaging. *Methods-Inf-Med* 31 (1): 29-35
- Gelsema E.S., Beckers A.L.D., Sorber C.W.J. and De Bruijn W.C. (1992) Quantification procedures for electron energy-loss spectroscopy and imaging: the use of correspondence analysis for element determination. *J. Microsc.* 166 (3): 287-296.
- Rademakers L.H.P.M., Koningsberger J.C., Sorber C.W.J., Baart de la Faille H., Van Hattum J. and Marx J.J.M. (1993) Accumulation of iron in erythroblasts of patients with erythropoietic protoporphyria. *European Journal of Clinical Investigation* 23: 130-138.
- Ringeling P.L., Cleton M.I., Kroos M.J. Sorber C.W.J., De Bruijn W.C., Harrison P.M. and Van Eijk H.H. (1989) Lysosomal and cytosolic ferritins. A biochemical and electron-spectroscopic study. *Biol. Metals* 2: 114-121.
- Willemsen R., Brünken R., Sorber C.W.J., Hoogeveen A.T., Wisselaar H.A., Van Dongen J.M. and Reuser A.J.J. (1991) A quantitative immunoelectron microscopic study on soluble, membrane-associated and membrane-bound lysosomal enzymes in human intestinal epithelial cells. *Histochemical Journal* 23: 467-473.
- Zondervan P.E., de Jong A., Sorber C.W.J., Kok L.P., De Bruijn W.C. and Van der Kwast Th.H. (1988) Microwave-stimulated incubation in immunoelectron microscopy: a quantitative study. *Histochemical J.* 20: 359-364.

---

**SUMMARY**

**SAMENVATTING**

---

## SUMMARY

Several methods are proposed for the elemental analysis of biological material with the use of electron energy-loss spectroscopy (EELS) and electron spectroscopic imaging (ESI) in a Zeiss EM902.

For spectra, the Simplex-method was tested and compared to Egerton's 2-area method, the Steepest descent method and the Loglog method. The Simplex method and the Loglog method performed best. The Simplex method was then used for the analysis of biological specimens containing calcium and iron. The results of the analysis of a test-spectrum, an iron-spectrum and a calcium-spectrum taken with various widths of the  $\Gamma$ -region were compared. It was observed that calcium is a hard element for EELS-analysis because of the carbon K-edge just in front of its ionization-edge. Ca- and Fe-Bio-standards, which were co-embedded with the specimens, were used to obtain elemental concentrations in the specimen.

In combination with the Kontron IBAS 2000, morphometrical image analysis was performed on cells and their reaction products. The influence of several acquisition factors was analyzed (objective-lens diaphragm diameter, image mode, number of integrations during image acquisition). Segmentation is applied using the cross-overs of the first derivative of the greyvalue distribution histogram of the image. Co-localization of several chemical elements could be demonstrated by comparing the net-intensity distribution images of the respective elements.

In images, several methods were tested for the separation of the element-information from the continuum. The power-law method gives the best results. The influence of the width of the integration-region on the obtained relative concentration was tested.

Since the power-law method did not overcome all problems encountered with image-analysis (Calcium), Multivariate statistical analysis (MSA) was examined as an alternative. The latter method performed very well and was able to analyze calcium images. MSA also reduces the influence of other sources of information in the images such as shading and radiation damage.

## SAMENVATTING

Verschillende methoden worden onderzocht voor de element analyse van biologisch materiaal met behulp van "electronen energie-verlies spectroscopie" (EELS) en "electronen spectroscopische afbeelding" (ESI) in een Zeiss EM902.

Voor spectra werd de Simplex-methode getest en vergeleken met Egerton's 2-oppervlakken methode, de steilste pad methode en de Loglog methode. De Simplex methode en de Loglog methode gaven de beste resultaten. De Simplex-methode werd vervolgens gebruikt voor de analyse van biologische preparaten die calcium en ijzer bevatten. De resultaten van de analyse van een test-spectrum, een ijzer-spectrum en een calcium-spectrum, verkregen met verschillende groottes voor het  $\Gamma$ -gebied, werden vergeleken. Hieruit blijkt onder andere dat calcium een erg moeilijk element is door de koolstof-piek net voor zijn ionisatie-kant. Calcium en ijzer Bio-standaarden, die bij de coupe waren ingebed, werden gebruikt om element concentraties te bepalen.

In combinatie met de Kontron IBAS 2000, werden cellen en hun reactie-producten morfologische geanalyseerd. De invloed van verschillende factoren werd bepaald (diametergrootte van het object-lens diafragma, afbeeld mode, aantal integraties bij beeldopname). Voor de segmentatie van de beeld-objecten werd gebruik gemaakt van de 1<sup>e</sup> afgeleide van het grijswaarde frequentie-histogram van het beeld. Co-localisatie van verscheidene chemische elementen kon worden aangetoond door de netto-intensiteits verdelings beelden van de respectievelijke elementen te vergelijken.

In beelden werden verschillende methodes getest om de element-informatie te scheiden van het continuüm. De "Power-law" methode gaf de beste resultaten. De invloed van de breedte van de  $\Delta$ -zone op de verkregen relatieve concentratie werd getest.

Aangezien de "Power-law" methode niet alle problemen kon oplossen die in beeld-analyse werden ondervonden (calcium) werd het gebruik van "Multivariate Statistische Analyse" (MSA) als alternatief onderzocht. MSA gaf zeer goede resultaten en maakte het ook mogelijk om calcium beelden te analyseren. MSA reduceerde ook de invloed van andere informatie-bronnen uit de beelden zoals "shading" en stralingsschade.



Toen ik vijf jaar geleden op de afdeling pathologie stage liep had ik nooit kunnen dromen dat ik in 1993 een promotie-onderzoek zou afronden. Dit is vooral mogelijk gemaakt door het vertrouwen en de steun van mijn co-promotor, **Dr. Wim de Bruijn** en mijn promotor, **Prof. Dr. Hans Jongkind**, waarvoor ik ze zeer dankbaar ben. Samen met **Prof. Dr. Edzard Gelsema** zorgden ze door hun heel verschillende invalshoeken voor een unieke combinatie om problemen te benaderen. Alle drie heel hartelijk bedankt hiervoor en voor het kritisch lezen van het manuscript. De overige leden van de leescommissie wil ik ook nog bedanken: **Prof. Dr. Fré Bosman** voor de gastvrijheid op de afdeling pathologie en voor het "automatiseren" van de afdeling waardoor ik veel extra ervaring maar ook veel extra werk kreeg, en **Prof. Dr. Noël Bonnet** voor zijn gastvrijheid tijdens mijn verblijf in Reims (Noël, thank you for your hospitality during my stay in Reims).

De afdeling electronen-microscopie ben ik zeer dankbaar voor de oergezellige tijd tijdens de afgelopen vijf jaar. **Piet van der Heul, Ton de Jong, Peter van Run, Annemiek van den Broek, Theo van der Schaft, Pieter Derkx** en **Alex Nigg**, ik zal jullie missen! Vooral de discussies tijdens de "werkbesprekingen". Drie collega's hadden al eerder afscheid genomen van de afdeling pathologie maar **Paula Delfos, Diane Trommelen** en **Elly Visser** ook jullie zal ik heel erg missen, vooral de uitjes tussen de middag naar de stad.

**Ton de Jong**, dank voor alle electronen microscopische lessen die je me met veel geduld en een uitgestreken gezicht hebt bijgebracht (labjassen, veiligheidsbrillen, mondkapjes en handschoenen om een filament te vervangen ???).

**Frank van der Panne** en **Paula Delfos** bedankt voor de fotografie. Ik weet dat ik soms erg lastig was maar de foto's / grafieken zijn prachtig.

**Piet van der Heul** (mijn paranymphomaan, je was als een vader voor de EM-afdeling) en **Diane Trommelen** bedankt voor het paranymphen.

De feestcommissie, sorry, het personeels-fonds, bedankt voor de gezellige planningen, vergaderingen, feesten en labdagen. **Monica Seijbel, Josiane Godschalk, Huib de Bruin, Hein Sleddens** en **Frank van der Panne** het was altijd heel gezellig.

De stagiaires van de afgelopen vijf jaar wil ik ook nog bedanken: **Jolanda Krijnen, Nettie de Breejen, Loek Timmermans, Mariëlla Ansems, Coert-Jan van Mook, Robert Brünken, Ellen Raaymakers, Kees de Crom** en **Bart Willemse**.

En natuurlijk ben ik mijn ouders zeer dankbaar voor hun constante steun tijdens de laatste 28 jaar.

Verder hebben nog vele mensen bijgedragen aan dit proefschrift en aangezien ik niet iedereen bij naam kan noemen wil ik hierbij iedereen bedanken die op enigerlei wijze heeft bijgedragen aan dit proefschrift of aan de gezellige sfeer tijdens de afgelopen 5 jaar.

---

## CURRICULUM VITAE

Lianne Sorber werd geboren op 27 december 1964 te Dordrecht. Na het eindexamen VWO in juli 1983 aan het Thomas More College te Oudenbosch heeft zij één jaar Biologie gestudeerd aan de Katholieke Universiteit te Nijmegen. Aangezien deze studie niet voldeed aan haar verwachtingen heeft zij deze studie afgebroken en vervolgens heeft zij van augustus 1984 tot juli 1988 de opleiding Hogere Laboratorium Informatica en Automatisering gevolgd aan het toenmalige Dr Struycken Instituut te Etten-Leur. Na haar stage op de afdeling Pathologische Anatomie van de Erasmus Universiteit Rotterdam in het 4<sup>e</sup> jaar van deze opleiding heeft zij van oktober 1988 tot december 1992 haar promotie onderzoek verricht als AIO (assistent in opleiding) op de afdeling Electronen Microscopie van de Pathologische Anatomie met als resultaat dit proefschrift. Hiervan werden drie maanden doorgebracht aan de INSERM-unit van de Universiteit te Reims (Frankrijk). Vanaf 1 juni 1993 zal zij werkzaam zijn bij Unilever in Sharnbrook, Engeland.